Studies on the eigenmodes of self-defocusing nonlinear optical systems with PT-symmetric super-Gaussian and k-wavenumber Scarf II potentials

Thesis submitted to

University of Calicut

for the award of the degree of

Doctor of Philosophy in Physics

under the Faculty of Science

by

THASNEEM A. R.

under the guidance of

Prof. P. A. SUBHA

Department of Physics

Farook College (Autonomous)

Farook College, Kozhikode

Kerala - 673632

India

February 2024

CERTIFICATE

Certified that the work presented in this thesis titled 'Studies on the eigenmodes of self-defocusing nonlinear optical systems with PT-symmetric super-Gaussian and k-wavenumber Scarf II potentials' is a bonafide work done by Ms. A. R. Thasneem under my guidance in the Department of Physics, Farook College (Autonomous), University of Calicut and that this work has not been included in any other thesis submitted previously for the award of any degree.

Farook College

February 2024

Prof. P. A. SUBHA
Research Supervisor
Department of Physics
Farook College
Kozhikode - 673 632.

DECLARATION

I hereby declare that the work presented in the thesis entitled 'Studies on the eigenmodes of self-defocusing nonlinear optical systems with PT-symmetric super-Gaussian and k-wavenumber Scarf II potentials' is based on the original work done by me under the guidance of Dr. P. A. Subha, Department of Physics, Farook College, University of Calicut, and has not been included in any other thesis submitted previously for the award of any degree. The contents of the thesis are undergone plagiarism check using 'iThenticate' software at C.H.M.K. Library, University of Calicut, and the similarity index found within the permissible limit. I also declare that the thesis is free from AI generated contents.

Thasneem A. R.

Farook College

February 2024

Prof. P. A. SUBHA
Research Supervisor
Department of Physics
Farook College
Kozhikode - 673 632.

CERTIFICATE

This is to certify that the corrections/suggestions recommended by the adjudicators have been incorporated in the thesis of A. R. Thasneem, research scholar under my supervision and that the contents in the thesis and the soft copy are one and the same.

31.05.2024

Farook College

Subha

Prof. P. A. SUBHA
Research Supervisor
Department of Physics
Farook College
Kozhikode - 673 632.

Acknowledgements

I would like to express my deepest gratitude to all those who supported me throughout this journey, enabling me to complete my Ph.D. thesis successfully. First and foremost, I would like to thank my Ph.D. supervisor Prof. P. A. Subha, former Head of the Department, Department of Physics, Farook College for the enduring support, invaluable guidance and encouragement throughout the entire journey. I am honoured to have the opportunity to work with her, whose expertise in the topic was extremely helpful. Her dedication, sincerity and dynamism have deeply inspired me. I am profoundly thankful for her immeasurable contribution to my academic achievements.

I would like to acknowledge Dr. K. A. Aysha Swapna, Principal of Farook College and Dr. K. M. Naseer, former Principal of Farook College for their great support in completing my research. I am grateful to Mr. Midhun Shah, Head of the Department of Physics, Farook College for providing resources and ample opportunities. I am also thankful to Dr. Sulfikkar Ali N. K., Research Coordinator, Department of Physics, Farook College and Prof. T. Mohamed Nishad, Convenor, Research Promotion Council, Farook College for their guidance and support. Also, I thank Prof. M. M. Musthafa, Department of Physics, University of Calicut and Prof. Mohamed Shahin Thayyil, Department of Physics, University of Calicut for their assistance and support. I would like to acknowledge RUSA for providing financial support via Farook College and DST, India for the research facilities through FIST.

I am so grateful to Dr K. A. Muhsina, with whom we collaborated on some of our work, for her contributions that have greatly enriched the quality of my research. I express my sincere gratitude to Prof. K Indulekha, Former Director, School of Pure and Applied Physics, MG University, Kottayam for her motivation and recognition, and Dr. K. K. Abdulla, former HOD, Department of Physics, Farook College for his support and encouragement. I am so thankful to all the faculties of the Department of Physics, Farook College for their kind cooperation. I thank all the teaching and non teaching staffs of Farook College. Special thanks to Ms. Hyfa for her timely help in the office. Also, I thank Informatics Centre, Farook College for the technical support.

I thank my dear sister and fellow researcher Ms. Amal Abdulrahman for her wholehearted and constant support from start to finish. I am so thankful to Dr. T. Remi for her boundless support and technical assistance. I am also grateful to Dr. N. M. Musammil and Dr. T. P. Suneera for their sincere support. I also thank my fellow researchers Mr. Muhammed Jubeer and Ms. T. Sreeshna. I extend my wholehearted thanks to Ms. T. Aminabi and Dr. Ismail Maritheri for reigniting the thirst for research.

My intense desire for physics research sparked when I was in tenth standard. My uppa T. Abdul Rahman and my umma Asia O gave strong wings to conquer my dreams. All my prayers dear uppa and umma. I am so thankful to father-in-law T. P. Kassim and mother-in-law Nafeesa for their unrestricted cooperation. Thank you very much brother Abdul Gafoor, sisters Najmah, Dr. Nisreen and Amal for your emotional support from childhood. My heartfelt thanks to sisters-in-law Thayyiba, Shaheera, Noura, and brothers-in-law Dr. Naseer, Dr. Ali Muhammed, Javed Islam and Dr. Shakir. My sincere thanks to all my nephews. Your inquiry about my Ph.D status from time to time was a motivation for me. I am forever indebted to my grand parents, uncles and aunties. I will always be grateful to everyone in Varian Kandy family, Othayoth family, TP family and Thalakkayil family. I would like to thank housemaids for taking care of my kids. I thank all my teachers, friends and all other relatives for the support and motivation.

This voyage would not have been possible without the emotional and physical support of my beloved, Dr. Shahid T. P. Endless love for tolerating me during my stresses and struggles. My children did their works beautifully so I was able to make mine beautiful. Dear Fathima Kenza, Maryam Thahiyya and Muhammed Rayyan, my hugs to you with lots of love and affection. Thank you everyone who have been a part of this journey. Above all, I thank Almighty, the Most Gracious and Merciful, for His blessings in completing the thesis successfully. Accept these efforts taken to acquire knowledge as virtues in your path.

Thasneem A. R.

Abstract

The interaction of the high-intense beam with parity-time (PT) symmetric single and coupled nonlinear optical media, modelled by modified nonlinear Schrodinger equation, generates families of localised waves called optical bright and dark solitons, which find applications in high-speed signal communication, all-optical switching, unidirectional and non-reciprocal light transmission etc. Even though the stationary states and propagation dynamics of optical bright solitons are intensively studied, the existence and dynamics of dark solitons are less explored.

In the thesis, we analysed the existence of dark soliton-like solutions, stability, beam propagation and switching dynamics in the PT-symmetric optical systems with self-defocusing nonlinearity. The symmetric real and antisymmetric imaginary components of the PT-symmetric super-Gaussian and k-wavenumber Scarf II well and barrier potentials take the role of refractive index distribution and gain/loss effects. The real part of these potentials consists of different profiles of refractive index from smooth to step-index distributions. The delicate balancing between the effects of defocusing nonlinearity and PT-symmetric potentials leads to dark soliton form of solution, which is discussed in a single system. The threshold condition of PT phase transition depends on the strength of the nonlinearity and coefficients of real and imaginary potential. The stability of the solution is verified using the linear stability analysis and the propagation in the PT regime has also been analysed. The study has been extended to coupled system with equal gain and loss. The power variations of the low and high-frequency modes have been analysed using variational analysis. The switching dynamics of the coupled systems with PT-symmetric potentials are analysed for PT and broken PT phases using finite difference beam propagation method. The power switching between the channels in the PT regime and power confinement in one of the channels in the broken PT regime are observed.

The existence of the dark soliton-like solution has relevance in long-distance energy-efficient communication technology due to its high stability against losses. The switching dynamics in a PT-symmetric coupled system can contribute to the construction of switching devices and optical nanostructures. The power confinement in the broken PT regime has relevance in non-reciprocal and unidirectional signal transmission.

സാരം

പാരിറ്റി-ടൈം സമമിതിയുള്ള സിംഗിൾ, കപ്പിൾഡ് നോൺ ലീനിയർ ഒപ്റ്റിക്കൽ സിസ്റ്റവുമായുള്ള അതിതീവ്ര പ്രകാശബീമിന്റെ പ്രതിപ്രവർത്തനം ഒപ്റ്റിക്കൽ ബ്രൈറ്റ് സോളിറ്റോണുകൾ, ഡാർക്ക് സോളിറ്റോണുകൾ എന്നീ സ്ഥിരതയുള്ള തരംഗങ്ങളെ സൃഷ്ടിക്കുന്നു. ഇത് അതിവേഗ സിഗ്നൽ കമ്മ്യൂണിക്കേഷൻ, ഓൾ-ഒപ്റ്റിക്കൽ സ്വിച്ചിംഗ്, യൂണിഡയറക്ഷണൽ ലൈറ്റ് ട്രാൻസ്മിഷൻ മുതലായവ സാധ്യമാക്കുന്നു. ബ്രൈറ്റ് സോളിറ്റോണുകളുടെ നിശ്ചല അവസ്ഥകളും പ്രസരണവും ശാസ്ത്ര ലോകം ഏറെ പഠനവിധേയമാക്കിയെങ്കിലും ഡാർക്ക് സോളിറ്റോണുകളുടെ അസ്തിത്വത്തെയും ചലനാത്മകതയെയും കുറിച്ചുള്ള പഠനങ്ങൾ വളരെ കുറവാണ്.

ഈ പ്രബന്ധത്തിൽ, സെൽഫ്-ഡീഫോക്കസിംഗ് നോൺലീനിയർ സ്വഭാവവും പാരിറ്റി-ടൈം സമമിതിയും കാണിക്കുന്ന ഒപ്റ്റിക്കൽ മാധ്യമത്തിൽ രൂപപ്പെടുന്ന സോളിറ്റോൺ പോലുള്ള തരംഗങ്ങളുടെ അസ്തിത്വം, സ്ഥിരത, പ്രസരണം, സ്വിച്ചിംഗ് എന്നിവ അവലോകനം ചെയ്യുന്നു. പാരിറ്റി-ടൈം സമമിതിയുള്ള സൂപ്പർ-ഗോസിയൻ, കെ-വെയ്റ് നമ്പർ സ്കാർഫ് II പൊട്ടൻഷ്യലുകളുടെ റിയൽ ഭാഗവും ഇമാജിനറി ഭാഗവും യഥാക്രമം മാധ്യമത്തിന്റെ അപവർത്തന സൂചികയുടെ വിതരണത്തെയും സിസ്റ്റത്തിലുണ്ടാവുന്ന നേട്ടം/നഷ്ടത്തിന്റെ പങ്കിനെയും പ്രതിഫലിപ്പിക്കുന്നു. സിംഗിൽ സിസ്റ്റത്തിൽ നോൺ ലീനിയാരിറ്റിയുടെയും പാരിറ്റി- ടൈം സമമിതി പൊട്ടൻഷ്യലുകളുടെയും സന്തുലനം കാരണം രൂപപ്പെടുന്ന ഡാർക്ക് സോളിറ്റോണുകളെക്കുറിച്ച് പഠനം നടത്തി. പാരിറ്റി-ടൈം സമമിതിയുള്ള ഘട്ടത്തിൽ നിന്ന് ഈ സമമിതി നഷ്ടപ്പെടുന്ന ഘട്ടത്തിലേക്കുള്ള പരിവർത്തനം മനസ്സിലാക്കുകയും അത് ഏതൊക്കെ ഘടകങ്ങളെ ആശ്രയിച്ചിരിക്കുന്നു എന്നതിനെറ വിശകലനവും നടത്തി. ലീനിയർ സ്റ്റബിലിറ്റി അനാലിസിസ് ഉപയോഗിച്ച് സോളിറ്റോണിന്റെ സ്ഥിരത പരിശോധിക്കുകയും അതിന്റെ നഷ്ട രഹിത പ്രക്ഷേപണം മനസ്സിലാക്കുകയും ചെയ്തു. ഈ പഠനം ലാഭവും നഷ്ടവും തുല്യമായ കപ്പിൾഡ് സിസ്റ്റത്തിലേക്ക് വിപുലീകരിക്കുകയും വേരിയേഷനൽ അനാലിസിസ് വഴി രണ്ട് മാധ്യമങ്ങളിൽ ഉണ്ടാവുന്ന പവർ വിതരണവും അപഗ്രഥിച്ചു. പാരിറ്റി-ടൈം സമമിതി പൊട്ടൻഷ്യൽ ഉള്ള കപ്പിൾഡ് സിസ്റ്റങ്ങളുടെ സ്വിച്ചിംഗ് ഡൈനാമിക്സ്, പരിവർത്തന ഘട്ടത്തിന് മുമ്പും ശേഷവും പരിശോധിച്ചു. പാരിറ്റി-ടൈം സമമിതി നിലനിൽക്കുന്ന ഘട്ടത്തിൽ മാധ്യമങ്ങൾക്കിടയിലെ പവർ സ്വിച്ചിംഗും അത് നഷ്ടപ്പെടുന്ന ഘട്ടത്തിൽ ഒരു മാധ്യമത്തിലേക്ക് പവർ കേന്ദ്രീകരിക്കുന്നതും കാണാം.

ഡാർക്ക് സോളിറ്റൺ പോലുള്ള തരംഗങ്ങളുടെ ഉയർന്ന സ്ഥിരത കാരണം കമ്മ്യൂണിക്കേഷൻ ടെക്നോളജിയിൽ ഇതിന് വളരെ പ്രാധാന്യമുണ്ട്. പാരിറ്റി-ടൈം സമമിതി പ്രകടമാക്കുന്ന കപ്പിൾഡ് സിസ്റ്റത്തിലെ സ്വിച്ചിംഗ് ഡൈനാമിക്സിന് സ്വിച്ചിംഗ് ഉപകരണങ്ങളുടെയും ഒപ്റ്റിക്കൽ നാനോസ്കെച്ചുകളുടെയും നിർമ്മാണത്തിൽ സംഭാവന ചെയ്യാൻ കഴിയും. പാരിറ്റി-ടൈം നഷ്ടപ്പെട്ട ഘട്ടത്തിൽ പവറിന്റെ ഒരു മാധ്യമത്തിലെ കേന്ദ്രീകരണ സ്വഭാവത്തിന് ഏകദിശയിലുള്ള സിഗ്നൽ ട്രാൻസ്മിഷനിൽ കാര്യമായ പ്രസക്തിയുണ്ട്.

Contents

List of Figures

List of Tables

Preface

In the thesis, the eigenmodes of ground and excited states of self-defocusing nonlinear optical systems with parity-time (PT) symmetric super-Gaussian and k-wavenumber Scarf II potentials are studied. In optical systems, the refractive index and gain/loss distribution take the role of real and imaginary parts of the PT-symmetric potentials. The super-Gaussian and k-wavenumber Scarf II potentials comprise different profiles of refractive index from smooth to step-index distributions. Thesis consists of eight chapters in which the first chapter introduces basic terminologies and methods of analysis.

Chapter 2 presents the existence of dark soliton-like solutions in self-defocusing nonlinear medium with super-Gaussian potential. The stability and propagation of the stationary states are also discussed. **Chapter 3** deals with the stationary solutions and propagation dynamics of the single system under PT-symmetric k-wavenumber Scarf II potential. The symmetry and stability of the solutions with central dips are analysed in the linear and nonlinear regimes. The influence of the strength of real and imaginary potentials and the width of the potential on the threshold condition of phase transition are also analysed. The study has been extended to the eigenmodes of coupled systems with different types of PT-symmetric potentials. The eigenmode and power oscillation between the channels are studied for constant gain and loss profiles using variational analysis, in **Chapter 4**. Two-coupled nonlinear partial differential equation has been converted into four-coupled equation using variational analysis and the two-channel power distribution has been discussed. We also discuss the effect of the defocusing nonlinearity on the formation of eigenstates with central dips in the PT regime. **Chapter 5** focuses on the switching dynamics of coupled system with k-wavenumber Scarf II well potential. The high and low-frequency modes of ground and excited states and the switching dynamics between the channels are analysed. The effects of gain/loss coefficient and potential width on the power oscillation are discussed. **Chapter 6** analyses the interplay between the k-wavenumber Scarf II barrier potential and defocusing nonlinearity in the formation of stable eigenmodes in single and coupled systems. The switching dynamics of the system has been studied with low and high input

power in the PT and broken PT regimes. The power oscillation and the region of power confinement are also analysed for low and high inputs. In **Chapter 7**, coupled system with super-Gaussian barrier potential is analysed. The dark soliton-like solutions, stability and switching dynamics are studied. The power distribution in the two channels, and the role of super-Gaussian potential on the power oscillation and power confinement are also discussed. **Chapter 8** concludes the thesis with summarising the results and proposing the recommendations for future studies.

The formation of stable dark soliton-like solution has been realised by the effective steering of PT-symmetric potential and defocusing nonlinearity. The dark solitons have wide spread applications in long-distance energy-efficient communication technology as it exhibit stability against losses than bright soliton. The switching dynamics and power oscillation in defocusing nonlinear medium find applications in developing optical nanostructures and switching devices. Coupled system with high gain/loss effects, supporting power confinement in a single channel, has relevance in unidirectional light transport.

List of Papers

Published/Communicated

1. **A. R. Thasneem**, P. A. Subha, K. Aysha Muhsina, 'Stationary states of parity-time symmetric dark solitons in super-Gaussian potential'. Optik - International Journal for Light and Electron Optics 265 (2022) 169518.

2. **A. R. Thasneem**, P. A. Subha, 'One-dimensional PT-symmetric eigenmodes in k-wave number Scarf II potential with defocusing nonlinearity'. Phys. Scr. 98 (2023) 035208.

3. **A. R. Thasneem**, P. A. Subha, 'Self-defocusing nonlinear coupled system with PT-symmetric super-Gaussian potential'. Chaos 33 (2023) 093119.

4. **A. R. Thasneem**, P. A. Subha, 'Stationary states and switching dynamics of the self-defocusing nonlinear coupled system with PT-symmetric k-wavenumber Scarf II potential'. Chaos, Solitons & Fractals 177 (2023) 114245.

5. **A. R. Thasneem**, P. A. Subha, 'The switching dynamics of self-defocusing nonlinear coupled system with PT-symmetric Scarf II barrier potential'. Eur. Phys. J. Plus (2024) 139.

6. **A. R. Thasneem**, P. A. Subha, 'The effect of self-defocusing nonlinearity on the eigenmodes of PT-symmetric single system with k-wavenumber Scarf II barrier potential'. (Accepted for publication)

7. **A. R. Thasneem**, P. A. Subha, 'The eigenstates of PT-symmetric coupled system with self-defocusing Kerr-nonlinearity'. (Under review)

List of International Conference Presentations

1. **A. R. Thasneem**, P. A. Subha, Two-dimensional dark soliton in inhomogenous media, International Conference on Theoretical and Experimental Physics (ICTEP 2020), Farook College, February 2020.

2. **A. R. Thasneem**, P. A. Subha, Dark soliton in PT-symmetric Gaussian potential, Conference on Nonlinear Systems and Dynamics (CNSD 2021), Centre for Nonlinear Science & Engineering, SEEE, SASTRA, deemed University, Thanjavur, December 2021.

3. **A. R. Thasneem**, P. A. Subha, The eigenmodes of parity-time symmetric systems with defocusing nonlinearity, Conference on Nonlinear Systems and Dynamics (CNSD 2022), IISER Pune, December 2022.

List of Abbreviations

PT	Parity-Time
GVD	Group Velocity Dispersion
SPM	Self-Phase Modulation
NLSE	Nonlinear Schrodinger Equation
BEC	Bose-Einstein Condensates
ODE	Ordinary Differential Equation
PDE	Partial Differential Equation
NLPDE	Nonlinear Partial Differential Equation
FDM	Finite Difference Method
FDBPM	Finite Difference Beam Propagation Method
LSA	Linear Stability Analysis
BDG	Bogoliubov-de Genes
OI	Oscillatory Instability

Chapter 1

Fundamental concepts and thesis outline

1.1 Introduction

Nonlinear optics deals with various optical effects due to the interactions of intense optical radiation with matter and it is one of the fastest-growing research fields after the invention of the laser. Low-intensity optical signals are not sufficient to modify the optical properties of the material systems. The interaction of high-intense laser light with the material system gives rise to nonlinear effects like second-harmonic generation, nonlinear refraction and third-harmonic generation etc. Media with inversion symmetry prevent the second-order nonlinear response and the presence of third-order nonlinear response contributes to effects like soliton generation and four-wave mixing [1].

The phenomenon of soliton was first noticed by John Scott Russell in 1834, at a canal in Scotland. Soliton is a self-reinforcing localised wave packet which can propagate over a long distance without any distortion. Soliton, formed by the delicate balance between linear and nonlinear effects in a medium, has been a subject of intense research in different areas of nonlinear physics including Bose-Einstien condensates (BEC), electronics, fluid dynamics, optics and so on. Optics is definitely a fertile field for the physical realisation of the soliton and the enhanced

control over many undesirable optical effects have important roles in high-speed signal transmission in advanced communication technology.

Optical soliton for communication was first suggested in 1973. Different kinds of optical solitons, including bright and dark solitons, described by the famous nonlinear Schrodinger equation, have been identified. The spatial bright and dark optical solitons are observed when the effect of beam diffraction compensates with the self-focusing and self-defocusing nonlinear effects, respectively. The nonlinear systems with different kinds of parity-time (PT) symmetric potentials can host localised solutions and have applications in the construction of optical fibre networks, solid-state waveguides, switching devices and unidirectional couplers. In nonlinear optical systems, PT-symmetry can be achieved by tailoring the refractive index and gain/loss distributions of the medium. The PT-symmetric super-Gaussian and k-wavenumber Scarf II potentials include a wide range of refractive index distributions in an optical medium. PT-symmetric single and coupled systems with self-focusing nonlinearity are studied widely, whereas systems with self-defocusing nonlinearity are less explored. The studies on defocusing nonlinear PT systems have relevance because the dark solitons are more stable than the bright solitons.

1.2 Optical solitons

The origin of nonlinear effect in optical fibre is caused by the nonlinear response of polarization to a strong optical field. In nonlinear optics, the induced polarization $\boldsymbol{P}$ in an isotropic medium can be expressed as

$$\boldsymbol{P} = \epsilon_0 \ (\chi^{(1)}.E + \chi^{(2)}.E^2 + \chi^{(3)}.E^3 + ...), \tag{1.1}$$

where E implies the amplitude of the electric field and ϵ_0 refers to the permittivity of free space. $\chi^{(1)}$ represents the linear susceptibility and $\chi^{(2)}, \chi^{(3)}, ...$ refer to the higher order nonlinear susceptibilities. Because of the inversion symmetry displayed by the amorphous and crystalline solids, the second-order susceptibility $\chi^{(2)}$ vanishes [2]. But the third-order susceptibility, $\chi^{(3)}$, is present both in centrosymmetric and noncentrosymmetric media.

1.2.1 Linear effects

Group velocity dispersion

Group velocity dispersion (GVD) is an optical effect in which group velocity varies with the frequency of light waves. It will depend on the properties of the material of the fibre. Different frequency components of the light wave travel at different speeds in the direction of propagation. The relative time delay (Δt_D) between the signals of different frequencies, ω_1 and ω_2, at the propagation distance z is given by [3]

$$\Delta t_D = k^{''}(\omega_1 - \omega_2)\ z. \tag{1.2}$$

If $k^{''} < 0$, the dispersion is anomalous for which the information with higher frequency arrives earlier. Whereas, if $k^{''} > 0$, the dispersion is normal for which the information with lower frequency arrives earlier. This time delay leads to the loss of information.

1.2.2 Nonlinear effects

In nonlinear optics, third-order susceptibility leads to the optical Kerr effect. This is due to the deformation of the electron orbits of the molecules in the presence of an applied electric field. The index of refraction of a dielectric material is proportional to the square of the electric field and it modifies the refractive index as

$$n = n_0 + n_2|E|^2, \tag{1.3}$$

where n_0 is the linear index of refraction and n_2 represents the Kerr nonlinearity.

Self-phase modulation

When the input is a pulsed laser beam, the refractive index change, $\Delta n(t) = n_2 I(t)$, is a function of time. It induces a phase shift, $\Delta\phi_N$, given by

$$\Delta\phi_N = n_2 \frac{\omega}{c} I z. \tag{1.4}$$

This effect in a nonlinear system is termed as self-phase modulation (SPM).

Self-focusing and self-defocusing nonlinearity

In a third-order nonlinear medium, a laser beam may be self-focused or self-defocused depending on the properties of the medium. It induces intensity-dependent refractive index change, $\Delta n(r) = n_2 I(r)$, where r is the radius of the beam in the transverse direction. Depending on the sign of the nonlinearity coefficient, the nonlinear medium acts like a focusing ($n_2 > 0$) or defocusing ($n_2 < 0$) lens. For nonlinear media with $n_2 < 0$, the optical beam spreads faster than diffraction and is self-defocused.

1.2.3 Nonlinear Schrodinger Equation (NLSE)

The optical field evolution in a nonlinear medium is governed by the nonlinear Schrodinger equation. In the nonlinear medium, the wave equation is given by Maxwell's relation as

$$\nabla^2 \mathbf{E} - \frac{1}{c^2}\frac{\partial^2 \mathbf{E}}{\partial t^2} = \frac{1}{\epsilon_0 c^2}\frac{\partial^2 \mathbf{P}}{\partial t^2} \tag{1.5}$$

Due to the first and third-order susceptibilities, induced polarization consists of linear and nonlinear components,

$$\mathbf{P}(\mathbf{r}, t) = \mathbf{P}_L(\mathbf{r}, t) + \mathbf{P}_{NL}(\mathbf{r}, t)$$

and are given by

$$\mathbf{P}_L(\mathbf{r}, t) = \epsilon_0 \int_{-\infty}^{\infty} \chi^{(1)}(t - t')\mathbf{E}(\mathbf{r}, t')\, dt' \tag{1.6}$$

$$\mathbf{P}_{NL}(\mathbf{r}, t) = \epsilon_0 \iiint_{-\infty}^{\infty} \chi^{(3)}(t - t_1)(t - t_2)(t - t_3)\mathbf{E}(\mathbf{r}, t_1)\mathbf{E}(\mathbf{r}, t_2)\mathbf{E}(\mathbf{r}, t_3)\, dt_1 dt_2 dt_3. \tag{1.7}$$

Assuming that the nonlinear response is instantaneous, Equation (1.7) can be simplified to

$$\mathbf{P}_{NL}(\mathbf{r}, t) = \epsilon_0 \chi^{(3)}\mathbf{E}(\mathbf{r}, t)\mathbf{E}(\mathbf{r}, t)\mathbf{E}(\mathbf{r}, t). \tag{1.8}$$

The corresponding nonlinear part of the dielectric constant causes the intensity-dependent refractive index as given in Equation (1.3). It considerably affects the

optical pulse/beam propagation in the nonlinear Kerr medium.

In the temporal domain, for optical pulse propagating in an optical fibre, the time-dependent pulse envelope is given by

$$E(\mathbf{r},t) = A(Z,t)F(X,Y)\ \exp(i\beta_0 Z), \tag{1.9}$$

where $F(X,Y)$ represents the field distribution in transverse direction, $\beta_0 = k_0 n_0$ is the propagation constant and Z is the axis of propagation. The pulse amplitude $A(Z,t)$ is time-dependent because of GVD. In the absence of the nonlinear effect, the optical pulses are broadened. Taking the Fourier transform of $A(Z,t)$, $A(Z,\omega)$ can be written as

$$\frac{\partial \tilde{A}}{\partial Z} = i[\beta(\omega) + \Delta\beta + \beta_0]\tilde{A}. \tag{1.10}$$

where $\beta(\omega) = k_0 n(\omega)$ and $\Delta\beta$ is the nonlinear part which is defined as

$$\Delta\beta = k_0 n_2 |A|^2 \frac{\iint_{-\infty}^{\infty} |F(X,Y)|^4 dX dY}{\iint_{-\infty}^{\infty} |F(X,Y)|^2 dX dY} \equiv \gamma |A|^2, \tag{1.11}$$

i.e., frequency and intensity-dependent phase shift is observed with the propagation. Expanding $\beta(\omega)$ using Taylor series expansion,

$$\beta(\omega) = \beta_0 + (\omega - \omega_0)\beta_1 + \frac{1}{2}(\omega - \omega_0)^2\beta_2 + \frac{1}{6}(\omega - \omega_0)^3\beta_3 + ..., \tag{1.12}$$

where

$$\beta_m = (\frac{d^m}{d\omega^m})_{\omega=\omega_0},\ (m = 1, 2, 3, ...).$$

Substituting Equation (1.12) in Equation (1.10) and taking the inverse Fourier transform we get an equation for $A(Z,t)$ as

$$\frac{\partial A}{\partial Z} + \beta_1 \frac{\partial A}{\partial t} + i\frac{\beta_2}{2}\frac{\partial^2 A}{\partial t^2} = i\gamma |A|^2 A. \tag{1.13}$$

Physically, the parameter β_2 represents the group-velocity dispersion. In Equation (1.13), the transformations given below are applied.

$$\tau = (t - \beta_1 Z)/T_0,\ z = Z/L_D,\ \psi = \sqrt{|\gamma| L_D A},$$

where T_0 is usually taken as the input pulse width and the dispersion length is given by $L_D = T_0^2/|\beta_2|$. The modified form of (1+1)- dimensional NLSE is

$$i\frac{\partial\psi}{\partial z} - \frac{s}{2}\frac{\partial^2\psi}{\partial\tau^2} \pm |\psi|^2\psi = 0, \tag{1.14}$$

where $s = sgn(\beta_2) = \pm 1$ gives the sign of GVD. The nonlinear term may be negative or positive based on the properties of the optical medium.

In the spatial domain, the solution of Equation (1.5) can be written as

$$E(\mathbf{r}, t) = A(\mathbf{r})\ \exp(i\beta_0 Z). \tag{1.15}$$

The beam diffraction happens along the transverse co-ordinates X and Y. Here, X, Y and Z are the spatial co-ordinates related to $\mathbf{r}$, and $A(X, Y)$ describes the evolution of the field. In the presence of Kerr nonlinearity and diffraction, the beam envelope satisfies the nonlinear parabolic equation given as

$$2i\beta_0\frac{\partial A}{\partial Z} + (\frac{\partial^2 A}{\partial X^2} + \frac{\partial^2 A}{\partial Y^2}) + 2\beta_0 k_0 n_2 I A = 0, \tag{1.16}$$

n_2 is the coefficient of Kerr nonlinearity. If the nonlinear medium is a slab waveguide, for example, the optical beam is confined in one of the transverse directions and Equation (1.16) is modified as

$$2i\beta_0\frac{\partial A}{\partial Z} + \frac{\partial^2 A}{\partial X^2} + 2\beta_0 k_0 n_2 I A = 0. \tag{1.17}$$

We define the transverse scaling parameter, w_0, related to the input field width and $L_d = \beta_0 w_0$ as the diffraction length, scaled dimensionless variables $x = X/w_0$, $z = Z/L_d$ and $\psi = \sqrt{k_0 n_2 L_d}\ A$ are introduced. Using these variables, Equation (1.17) forms (1+1)-dimensional NLSE

$$\frac{\partial\psi}{\partial z} + \frac{1}{2}\frac{\partial^2\psi}{\partial x^2} \pm |\psi|^2\psi = 0. \tag{1.18}$$

Here $+|\psi|^2\psi$ represents self-focusing nonlinearity and $-|\psi|^2\psi$ implies self-defocusing nonlinearity.

1.3 The temporal and spatial solitons

In optics, the interplay between the pulse dispersion/beam diffraction and nonlinear effects results in optical solitons. Different types of optical solitons are extensively studied and have found applications in the field of fibre-optic communication. Temporal solitons are formed due to the compensation of the pulse dispersion and the refractive nonlinearity in waveguides. When the input is an optical pulse, the evolution equation in 1-D is given by

$$i\frac{\partial\psi}{\partial z} - \frac{d}{2}\frac{\partial^2\psi}{\partial\tau^2} + \beta|\psi|^2\psi = 0, \tag{1.19}$$

where τ is the time in the group-velocity frame. The second term is related to the GVD and d represents the coefficient of pulse dispersion. The third term emerges from the Kerr effect and β is the nonlinearity coefficient. Equation (1.19) gives rise to families of localised temporal solitons.

The effects of beam diffraction along the transverse direction compensate for the effects of the intensity-dependent refractive index of the medium to form a spatial soliton. The beam evolution in a nonlinear Kerr medium is represented by the general form of (1+1)-dimensional NLSE in terms of dimensionless variables as

$$i\frac{\partial\psi}{\partial z} - \frac{d}{2}\frac{\partial^2\psi}{\partial x^2} + \beta|\psi|^2\psi = 0. \tag{1.20}$$

The nonlinear Schrodinger equation given by Equation (1.20) leads to families of localised solutions called spatial solitons.

1.3.1 Bright and dark solitons

Temporal bright solitons are evolved for anomalous GVD ($d < 0$) and temporal dark solitons are formed for normal GVD ($d > 0$), in Equation (1.19) for positive SPM. Depending on the sign of the Kerr nonlinearity coefficient β in Equation (1.20), two types of spatial solitons are formed for negative beam diffraction ($d < 0$). For an optical medium with self-focusing nonlinearity, $\beta > 0$, there exists spatial bright soliton. On the other hand, for self-defocusing nonlinear medium with $\beta < 0$,

spatial dark soliton is formed. Optical dark solitons are light pulses that appear as an inverted bell-shaped local depression on a non-zero background [4–6]. Although the existence of dark soliton in optical fibres was predicted in the early 1970s the experimental verification was reported only very recently. The fundamental dark solitons are mainly two kinds, black and grey solitons. The dark soliton having zero intensity at its center is called a black soliton and that with a nonzero dip is called a grey soliton. Greater stability is exhibited by the dark soliton against losses and it is less affected by the interaction forces than the bright soliton. Though optical solitons are basically classified into bright and dark solitons, other kinds of solitons like spatio-temporal soliton, gap soliton, vortex soliton, etc., have been discovered depending on the dispersive and nonlinear properties of the optical medium.

1.4 PT-symmetry

Carl Bender and his collaborators proposed that non-Hermitian Hamiltonian may possess real spectra if it meets the conditions of parity-time (PT)-symmetry [7]. Performing the parity reflection operator ($\hat{P}$) and time-reversal operator ($\hat{T}$) on the position and momentum coordinates, the changes are defined by

$$\hat{P} \text{ as } x \to -x,\ p \to -p$$
$$\hat{T} \text{ as } x \to x,\ p \to -p,\ i \to -i.$$

The potential $V(x) = V_r(x) + iV_i(x)$ is known as PT-symmetric if it obeys $V(x) = V^*(-x)$, i.e., when the real and imaginary parts satisfy $V_r(x) = V_r(-x)$ and $V_i(x) = -V_i(-x)$. It means that PT-symmetry requires the condition that the real part of the potential must be an even function of the transverse coordinate, whereas the imaginary part must be an odd function. Theoretical analysis and experimental realisation of PT-symmetric non-Hermitian systems have attracted researchers in quantum mechanics [8, 9], optics and photonics [10], Bose-Einstein condensates [11], plasmonic waveguides and metamaterials [12], superconductivity etc. The optical system is an ideal playland for the physical realisation of the parity-time symmetric system, making use of the refractive index profile and gain/loss in the system in place of complex potential [13, 14]. A PT-symmetric system shows the behaviour of

a conservative system and transforms into a dissipative system after PT-symmetry breaking. The parity-time symmetric physical system with real eigenvalue spectrum and its abrupt phase transition at the breaking point of PT-symmetry has become an area of intense research.

1.4.1 PT-symmetry in optical system

The intensity evolution through a nonlinear Kerr medium with PT-symmetric distribution of the index of refraction is governed by the normalised NLSE of the form

$$i\frac{\partial\psi}{\partial z} + \frac{d}{2}\frac{\partial^2\psi}{\partial x^2} + \beta|\psi|^2\psi + [V_r(x) + i\ V_i(x)]\psi = 0, \tag{1.21}$$

V_r and V_i are real and imaginary components of the complex potential. The PT-symmetric potential represents the complex refractive index distribution of the medium as $n(x) = n_r(x) + in_i(x)$. The real part has a smooth symmetric profile, i.e., $n_r(x) = n_r(-x)$. Whereas, the imaginary part has an anti-symmetric distribution $n_i(x) = -n_i(-x)$. The refractive index must obey the condition of PT-symmetry, $n(x) = n^*(-x)$.

1.4.2 PT-symmetric potentials

The realisation of different profiles of complex PT-symmetric potentials like Gaussian, super-Gaussian, Rosen-Morse, Scarf II, k-wavenumber and multiwell Scarf II, sextic anharmonic double well etc., are attained by amalgamating an antisymmetric gain/loss profile on an even refractive index distribution. Out of which we focused on super-Gaussian and k-wavenumber Scarf II potentials. The transverse distribution of the barrier and well profiles of these potentials have been discussed in respective chapters in detail.

1.5 Methods of analysis

The theoretical studies on PT-symmetric single and coupled systems with self-defocusing nonlinearity are focused in this work. The stationary solution, prop-

agation and switching dynamics are analysed. The model equations are nonlinear partial differential equations (NLPDE) and we have studied the system using variational and numerical methods.

1.5.1 Variational method

It is a semi-analytical method based on the Lagrangian formalism of classical mechanics. We construct Lagrangian density which generates the model equations. The variation of the parameters with respect to the Lagrangian is evaluated by choosing a trial function of unknown variables. If the system is dissipative, the total Lagrangian density will be the sum of conservative part and non-conservative part, i.e., $L = L_C + L_{NC}$. The dynamics of the dissipative system is described by Euler-Lagrange equations given by

$$\frac{\partial}{\partial z}\frac{\partial L_C}{\partial \psi_z} + \frac{\partial}{\partial x}\frac{\partial L_C}{\partial \psi_x} - \frac{\partial L_C}{\partial \psi} = Q_i. \tag{1.22}$$

The function Q_i includes all dissipative processes which are involved in the non-conservative Lagrangian density. The reduced Lagrangian is given by

$$< L_c >= \int_{-\infty}^{\infty} L_c dx. \tag{1.23}$$

The trial functions are chosen judiciously and the standard variational approach for the dissipative system is given by

$$\frac{d}{dz}\frac{\partial < L_c >}{\partial(\eta_{iz})} + \frac{d}{dx}\frac{\partial < L_c >}{\partial(\eta_{ix})} - \frac{\partial < L_c >}{\partial \eta_i} = 2Re\int_{-\infty}^{\infty} Q_i \frac{\partial \psi^*}{\partial \eta_i} dx, \tag{1.24}$$

where η corresponds to parameters that are varied in the variational Ansatz. Using Equations (1.22), (1.23) and (1.24), the power variations in the two channels of a coupled system are obtained.

1.5.2 Numerical Methods

Single and coupled NLPDEs are studied numerically to find the localised eigenmodes of ground and excited states. Eigenvalue equations are obtained from NLPDEs and are solved using the finite difference method (FDM). The discretisation of the differential operators are done and converted the eigenvalue equation into matrix form. The matrix is solved to get the eigenvalues and corresponding eigenfunctions. The finite difference beam propagation method (FDBPM) is used to analyse the propagation dynamics and the stability has been studied using Bogoliubov-de Genes (BDG) equations.

FDBPM

The propagation and switching dynamics have been analysed by solving NLPDE using the finite difference beam propagation method. In this method, the continuous domain is discretized by splitting the $x-z$ plane into rectangular grids with grid spacing $\Delta x = h$ and $\Delta z = k$ such that $x = ih$ and $z = jk$, where i and j are integers. Taking the Taylor series expansion of a function, $f(x)$, in the neighborhood of x, we get

$$\begin{aligned} f(x+h) &= f(x) + h\frac{\mathrm{d}f(x)}{\mathrm{d}x} + \frac{h^2}{2}\frac{\mathrm{d}^2 f(x)}{\mathrm{d}x^2} + \frac{h^3}{6}\frac{\mathrm{d}^3 f(x)}{\mathrm{d}x^3} + ..., \\ f(x-h) &= f(x) - h\frac{\mathrm{d}f(x)}{\mathrm{d}x} + \frac{h^2}{2}\frac{\mathrm{d}^2 f(x)}{\mathrm{d}x^2} - \frac{h^3}{6}\frac{\mathrm{d}^3 f(x)}{\mathrm{d}x^3} + ... \end{aligned} \tag{1.25}$$

Hence the first and second differential terms of the equation are approximated to

$$\begin{aligned} \frac{\mathrm{d}^2 f(x)}{\mathrm{d}x^2} &= \frac{f_{i+1}^j - 2f_i^j + f_{i-1}^j}{h^2}, \\ \frac{\mathrm{d}f(z)}{\mathrm{d}z} &= \frac{f_i^{j+1} - f_i^j}{k}. \end{aligned} \tag{1.26}$$

The NLPDE is solved using the Crank-Nicolson scheme.

The Crank-Nicolson method is an implicit method for solving partial differential equations. In this method, z and x derivatives are replaced by central difference approximation at the halfway between the grid points (i, j) and $(i, j+1)$. Thus

diffusion equation can be written as

$$\frac{f_i^{j+1} - f_i^j}{\Delta z} = \frac{\alpha}{2}[\frac{f_{i+1}^j - 2f_i^j + f_{i-1}^j}{(\Delta x)^2} + \frac{f_{i+1}^{j+1} - 2f_i^{j+1} + f_{i-1}^{j+1}}{(\Delta x)^2}]. \tag{1.27}$$

Assuming f is known at j^{th} level and taking $i = 1, 2, ..., N-1$ with boundary values f_0 and f_N, the above equation yields a set of simultaneous equations in terms of f_i^{j+1}. Taking $r = \alpha\Delta z/(\Delta x)^2$, Equation (1.27) forms a tridiagonal matrix equation given by

$$\begin{bmatrix} 1+r & -r/2 & . & ... \\ -r/2 & 1+r & -r/2 & ... \\ . & . & . & ... \\ . & . & . & ... \\ ... & . & -r/2 & 1+r \end{bmatrix} \begin{bmatrix} f_1^{j+1} \\ f_2^{j+1} \\ . \\ . \\ f_{N-1}^{j+1} \end{bmatrix} = \begin{bmatrix} d_1^j \\ d_2^j \\ . \\ . \\ d_N^j. \end{bmatrix} \tag{1.28}$$

where d_i^j are known variables. This matrix is in the form $A\psi = D$ and hence output field is obtained as $\psi = A^{-1}D$.

1.5.3 BDG equations

The stability of the stationary state solutions in the PT-symmetric single system has been analysed taking into consideration of the effect of small perturbations of the form [15, 16], $\psi(x,z) = [\phi(x) + a(x,z)]\exp(-i\mu z)$ on the solutions. Here,

$$a(x,z) = p(x)\exp(i\lambda z) + q(x)\exp(-i\lambda^* z).$$

p and q denote the perturbation eigenfunctions and λ represents perturbation growth rate. The stability has been analysed using linearised BDG equations

$$\lambda \begin{bmatrix} p \\ q^* \end{bmatrix} = \begin{bmatrix} L_1 + iV_i & \beta\phi^2 \\ -\beta(\phi^*)^2 & -(L_1 + iV_i) \end{bmatrix} \begin{bmatrix} p \\ q^* \end{bmatrix}, \tag{1.29}$$

where $L_1 = \mu + \frac{d}{2}\frac{\partial^2}{\partial x^2} + 2\beta|\phi|^2 + V_r(x)$. Equation (1.29) is analysed to study the stability of the solutions. $Im(\lambda) = 0$ implies linearly stable solutions. The solutions exhibit oscillatory instability (OI) if the eigenvalues are complex. The eigenvalues with $Im(\lambda) < 0$ refer to exponentially growing modes and $Im(\lambda) > 0$ correspond to exponentially decaying modes. The solution is completely unstable, when any one of the eigenvalues is purely imaginary, due to the exponentially amplifying noise.

1.6 Outline of the thesis

The thesis presents the studies on the eigenmodes of ground and excited states of self-defocusing nonlinear single and coupled systems with PT-symmetric super-Gaussian and k-wavenumber Scarf II potentials. The existence of dark soliton-like solutions, stability, beam propagation and switching dynamics in the symmetry-preserving and symmetry-broken phases are analysed. The thesis consists of eight chapters. The fundamental concepts and basic terminologies are introduced in this chapter.

In Chapter 2, the eigenmodes in linear and self-defocusing nonlinear single systems with super-Gaussian potential have been studied as it addresses different types of confining distributions of the index of refraction ranging from step-index to smooth profiles. The role of the imaginary potential on the phase transition of the dark soliton solution has been analysed. Also, the effect of nonlinearity and the coefficient of real potential are studied. The stability of the stationary states using LSA and the propagation of the solution in the PT regime have also been discussed in this chapter.

In Chapter 3, the stationary states and dynamical evolution of eigenmodes under PT-symmetric k-wavenumber Scarf II potentials are analysed in the defocusing nonlinear medium. In the optical system, a set of symmetric refractive index and antisymmetric gain/loss distributions can be achieved by tuning the width of the potential. The effect of the imaginary potential on the eigenspectra are studied for the ground and first excited state, in linear and nonlinear media. The symmetry and stability of the eigenmode and its propagation are also analysed. The role of

nonlinearity, the width of the complex potential and the depth of the well potential on the PT phase transition of the system have been analysed.

In Chapter 4, the study has been extended to coupled systems with constant gain and loss. The power variation of the low and high-frequency modes in the gain and lossy channels when the gain channel is excited has been analysed using variational analysis. The stationary state, its stability and propagation dynamics of high and low-frequency modes are also analysed. The effect of nonlinearity on the formation of solutions with central dips and the variation of the threshold eigenvalues with coupling constant are discussed. The studies on the simplest case of PT-symmetric coupled systems with balanced gain and loss give rise to interesting physical phenomena and have applications in various fields like all-optical signal manipulation.

In Chapter 5, we focused on the switching dynamics of coupled systems by introducing k-wavenumber Scarf II well potential. The effect of defocusing nonlinearity and real potential on the dip formation for both the high and low modes of fundamental and even excited states are studied. Using the finite difference beam propagation method, the power-switching dynamics between the gain and lossy channels is analysed. The power-dependent switching and the effects of gain/loss terms and potential width on the power transfer are studied.

In Chapter 6, we studied the interplay between the k-wavenumber Scarf II barrier potential and weak and strong defocusing nonlinearity in the formation of localised stable eigenmodes in single and coupled systems. The switching dynamics of the coupled system is studied by exciting the gain (lossy) channel with low and high input power in the unbroken and broken PT regimes. Also, the power oscillation between the channels, the region of power confinement and the power variation during propagation in these two regimes are analysed.

In Chapter 7, the switching dynamics in super-Gaussian barrier potential in coupled system has been analysed. The effect of nonlinearity, coupling constant on the phase transition and stability of the stationary states are discussed. The power distribution with the propagation in the two channels of the system is analysed, in the PT and broken PT regimes, by exciting the gain channel with the stationary

solutions. The role of Gaussian and super-Gaussian distributions on the power oscillation and power confinement are also discussed.

Chapter 8 concludes the results of the thesis with recommendations for future studies.

Chapter 2

PT-symmetric dark solitons in super-Gaussian potential

2.1 Introduction

The propagation of optical solitons over relatively long distance without any change of its shape has relevance in modern signal transmission technology. When the effects of nonlinearity and pulse dispersion (for temporal solitons) or beam diffraction (for spatial solitons) balance each other, the pulse or beam can propagate without any change in its shape. Its evolution is governed by nonlinear Schrodinger equation with two distinct types of localised solutions, bright or dark soliton, determined by the type of nonlinearity, self-focusing or self-defocusing. In this chapter, the stationary states and propagation of solutions, in spatial domain, in a medium with self-defocusing nonlinearity and PT-symmetric super-Gaussian potential are studied.

Eventhough the PT-symmetric quantum systems were discovered in 1998, it is a purely speculative concept because the experimental realisation of such systems are difficult. For this reason the study is currently concentrated in optics in which of PT-symmetry can be easily constructed. During last decade, great attention has been attained by the studies in one-dimensional and multi-dimensional bright solitons in different PT-symmetric systems with periodic, generalised Scarf II, super-Gaussian potentials etc., in single [10, 17–21] and coupled structures [22–24]. Stable soliton

solutions with higher-order dispersion [25], competing cubic-quintic nonlinearity and derivative nonlinearity [26] in PT systems have been investigated. Eventhough many researchers focused their works in the field of bright solitons, studies on the dark solitons are very limited.

Analytical and numerical studies on the dark solitary waves can also be done for different kinds of models with good accuracy [27]. Dark solitons and vortices in nonlinear PT systems [28], in dual-core waveguides [29], interactions of black and grey solitons [30], vector dark soliton dynamics [31], dynamics of Manakov vector soliton [32], periodic oscillations by the dark soliton [33] etc., are proposed in this area, recently. The propagation dynamics and interactions of one and higher-dimensional dark solitons [34] and nonlinear tunnelling effects in various PT potentials need further investigations. Though the propagation dynamics of two or three-dimensional optical dark solitons are subjected to transverse instabilities, one-dimensional dark solitons in temporal and spatial domains with Kerr nonlinearity are not prone to transverse instabilities [35]. The phenomenon called Busch-Anglin effect has been noticed during the propagation of optical dark soliton in the presence of an external potential in defocusing nonlocal nonlinear medium and the role of nonlocality in triggering the effect has been discussed [36]. The effect of the coefficient of imaginary potential on the stationary states of 1-D optical dark soliton are studied in the self-defocusing nonlinear Kerr medium with PT-symmetric potential.

The fundamental and higher eigenstates of 1-D dark soliton in linear and nonlinear media with Gaussian and super-Gaussian potentials and the stability of the eigenmodes have been analysed in this chapter. The chapter is organised as follows: In Section 2.2, the theoretical model of the system is explained. In Section 2.3, the effect of gain/loss on the eigenstates in linear and nonlinear cases has been analysed. Section 2.4 discusses the stability of the dark soliton solution and the concluding section of the chapter, Section 2.5, summerises the results.

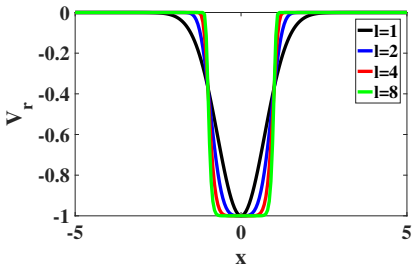

(a) Real

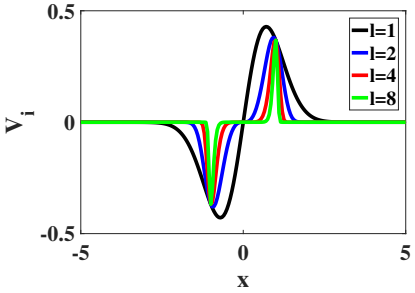

(b) Imaginary, Type A

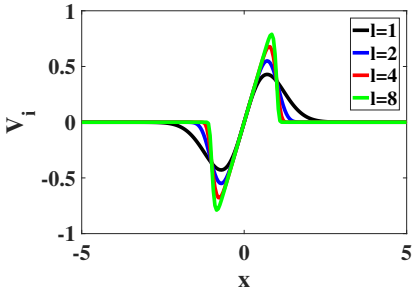

(c) Imaginary, Type B

Figure 2.1: The real and imaginary parts of the super-Gaussian potential at $k = 1$ and $\epsilon = 1$, for $l = 1, 2, 4, 8$. (a) The real component of the potential, (b) The imaginary component of Type A and (c) the imaginary component of Type B.

2.2 Nonlinear model

The light beam propagating in a nonlinear Kerr medium is governed by normalised NLSE

$$i\frac{\partial\psi}{\partial z} + \frac{d}{2}\frac{\partial^2\psi}{\partial x^2} + \beta|\psi|^2\psi + V(x)\psi = 0, \tag{2.1}$$

where ψ is the dark soliton solution propagating along z-direction and x is the transverse direction, respectively. d and β refer to diffraction and nonlinearity coefficients, respectively. $\beta > 0$ for self-focusing nonlinear medium and $\beta < 0$ for self-defocusing nonlinear medium. $V(x)$ is the PT potential and $V(x) = V_r(x) + i\ V_i(x)$. The system in self-defocusing nonlinear medium has been studied in this chapter. In optics, the refractive index distribution and gain/loss term takes the role of PT-symmetric potential.

We have considered PT-symmetric potential with the symmetric real part

$$V_r(x) = -k\exp(-x^{2l}), \tag{2.2}$$

where k refer to the coefficient of real potential and l has chosen as $l = 1, 2, 4, 8$. $l = 1$ refers to Gaussian and $l = 2, 4, 8$ represent super-Gaussian profiles. As l increases, the the central depression of V_r becomes wider and flattens with constant depth k. For large l values, $V_r(x)$ form a rectangular well profile which is shown in Fig. 2.1(a). The two profiles taken for the antisymmetric imaginary components are

Type A: The potential with

$$V_i^A(x) = \epsilon\ x^{2l-1} \exp(-x^{2l}), \tag{2.3}$$

where the gain/loss coefficient is represented by ϵ. For $l > 1$, the two peaks of $V_i^A(x)$ are narrowed and are shifted to the edges with the increase in l, which is shown in Fig. 2.1(b).

Type B: The potential with

$$V_i^B(x) = \epsilon\ x \exp(-x^{2l}). \tag{2.4}$$

For this type, the changes in V_i with l is negligible. At $l = 1$, both types have the same profile. It is clear from Fig. 2.1(c) that the peaks are wider for $V_i^B(x)$ than $V_i^A(x)$ and are located at the confined area of the real potential. Thus Type B is a better choice to admit the dependence of the potential in the tranverse direction on the field evolution, for the super-Gaussian distribution.

2.3 Stationary solutions

The solutions of stationary states of the dark soliton have been studied in linear and nonlinear cases. Using Ansatz

$$\psi(x, z) = \phi(x) \exp(-i\mu z), \tag{2.5}$$

the stationary solutions are studied. Here the eigenmode ϕ is a function of x only and μ is the propagation constant. Nonlinear eigenvalue equation satisfied by ϕ is

$$-\frac{d}{2}\frac{d^2\phi}{dx^2} - \beta|\phi|^2\phi - V(x)\phi = \mu\phi. \tag{2.6}$$

Equation (2.6) has been numerically solved by taking squared hyperbolic function as the initial form and the eigenvalues and eigenmodes are discussed. Because of the presence of gain/loss effects, as in Equation (2.6), μ will be a complex value, $\mu = \mu_r + i\ \mu_i$. The effect of the imaginary potential on the eigenvalue spectra of the ground and excited states are analysed.

	Type A				Type B			
l	1	2	4	8	1	2	4	8
$\epsilon_{th}^{(1)}$	0.6	1.1	2.1	4	0.6	0.85	0.9	0.9
$\epsilon_{th}^{(2)}$	1.35	2.15	4	7.8	1.35	1.4	1.35	1.3

Table 2.1: The first and second threshold values for Type A and Type B potentials in the linear regime.

2.4 The effect of imaginary potential

2.4.1 Linear system

For linear system, i.e., in the absence of the nonlinear Kerr effect, solutions have been studied by solving

$$-\frac{d}{2}\frac{d^2\phi}{dx^2} - [V_r(x) + iV_i(x)]\phi = \mu\phi. \tag{2.7}$$

The real and imaginary eigenvalues, μ_r and μ_i, and corresponding eigenmodes with the gain/loss coefficient have been studied in Gaussian and super-Gaussian potentials. The eigenvalues and eigenfunctions of fundamental and higher modes with Gaussian profile have been plotted in Fig. 2.2.

The blue dots shown in Figs. 2.2(a) and (b) represent the variation of the real and imaginary eigenvalues of the fundamental state with ϵ. For low values of ϵ,

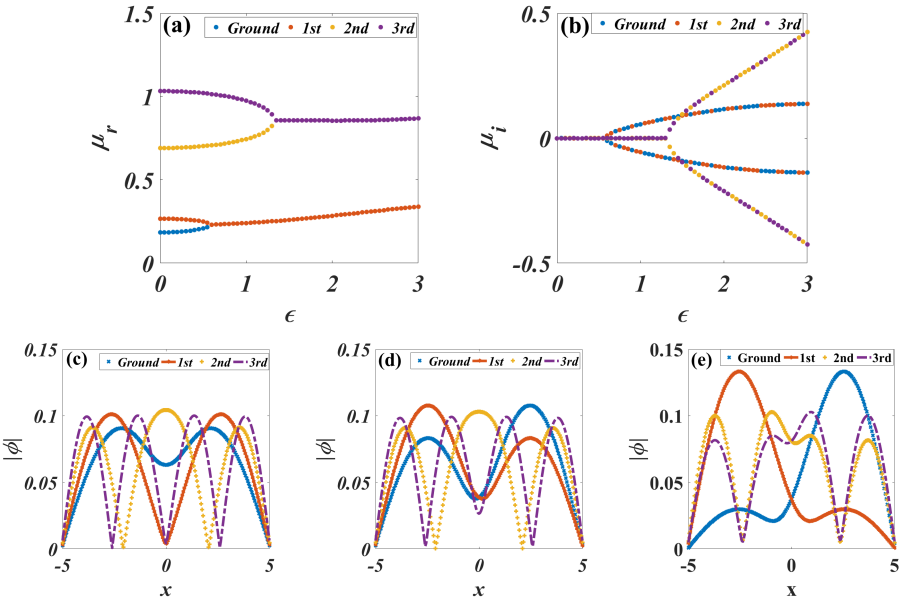

Figure 2.2: The eigenmodes of the ground, 1st, 2nd and 3rd excited states in PT Gaussian potential for linear case. First row: (a) real part of the eigenvalues and (b) imaginary part of the eigenvalues. Second row: eigenfunctions at (c) $\epsilon = 0.1$,(d) $\epsilon_{th}^{(1)} = 0.6$ and (e) $\epsilon_{th}^{(2)} = 1.35$.

only real eigenvalues are present. As ϵ increases, $|\mu_i|$ starts to grow keeping the μ_r almost constant. The critical threshold of ϵ at which the imaginary eigenvalue evolves is called the threshold value of the gain/loss coefficient (ϵ_{th}) or PT breaking point. The region where $\epsilon < \epsilon_{th}$ is called as PT-symmetric regime and if $\epsilon > \epsilon_{th}$, it is termed as broken PT-symmetric regime. The fundamental mode before and after the threshold value are shown as blue dotted curves in Figs. 2.2(c)-(e). The eigenmodes are symmetric along the x-axis below the threshold condition. When the gain/loss coefficient is greater than the threshold value, the symmetry gets broken.

The red dots in Figs. 2.2(a) and (b) represent real and imaginary components of the eigenvalues of 1st excited state. For low values of ϵ, the eigenvalues of the first excited state are real. Both the fundamental and first excited states have the equal threshold value called the first threshold value, $\epsilon_{th}^{(1)}$, above which the eigenvalues become complex conjugates. In Fig. 2.2(a) and (b), the yellow dots and purple dots represent eigenvalues of second and third excited states, respectively. For these states, eigenvalues are real below a threshold value, called the second threshold value, $\epsilon_{th}^{(2)}$. Above $\epsilon_{th}^{(2)}$, the imaginary eigenvalues are complex conjugates with equal

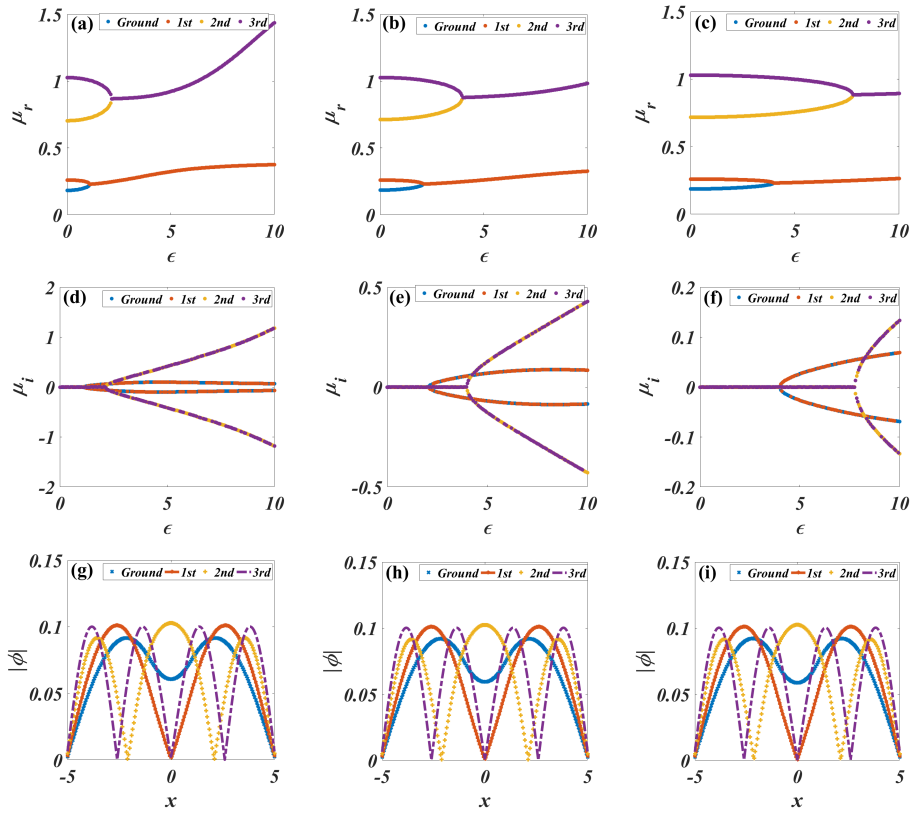

Figure 2.3: The eigenmodes of the fundamental and higher states in super-Gaussian Type A potential in the linear regime. Top panel: μ_r vs ϵ for (a) $l = 2$, (b) $l = 4$ and (c) $l = 8$. Middle panel: μ_i vs ϵ for (d) $l = 2$, (e) $l = 4$ and (f) $l = 8$. Bottom panel: eigenfunctions in $\mathcal{PT}$-symmetric regime ($\epsilon = 0.1$) for (g) $l = 2$,(h) $l = 4$ and (i) $l = 8$. Blue, red, yellow and purple colours indicate ground, 1st, 2nd and 3rd excited states, respectively.

real part. The threshold values are tabulated in Table 2.1. From the table it is clear that $\epsilon_{th}^{(2)} > \epsilon_{th}^{(1)}$.

The red dotted, yellow dotted and purple dashed curves, shown in Figs. 2.2(c)-(e), are the first, second and third eigenstates, respectively. All the eigenstates are symmetric in x direction when ϵ is less than the first and second threshold values as shown in Fig. 2.2(c). When $\epsilon_{th}^{(1)} < \epsilon < \epsilon_{th}^{(2)}$, the fundamental and first eigenstates are asymmetric, but 2nd and 3rd eigenstates are symmetric in x as shown in Fig. 2.2(d). Fig. 2.2(e) clearly shows that all the eigenstates break their symmetry at $\epsilon > \epsilon_{th}^{(2)}$.

Type A potential:

The stationary solutions of the model given in Equation (2.7) for super-Gaussian potential with V_i given in Equation (2.3), i.e. of the form Type A, have been studied. The eigenvalue spectra and eigenfunctions of fundamental and higher eigenmodes have been illustrated in Fig. 2.3. In Figs. 2.3(a)-(i), the blue, red, yellow and purple coloured plots imply the ground, first, second and third excited states, respectively. The real eigenvalue spectra for $l = 2, 4, 8$ are depicted in Figs. 2.3(a)-(c), respectively, and the first and second threshold values, $\epsilon_{th}^{(1)}$ and $\epsilon_{th}^{(2)}$ are given in Table 2.1. μ_i values for $l = 2, 4, 8$ are shown in Figs. 2.3(d)-(f), respectively. For small values of gain/loss coefficient, $\mu_i = 0$ and above $\epsilon_{th}^{(1)}$ and $\epsilon_{th}^{(2)}$, $|\mu_i|$ starts to grow with ϵ. The phase transition point increases as l increases for Type A potential. Also, $\epsilon_{th}^{(1)} < \epsilon_{th}^{(2)}$ for a given l value. The eigenstates below the PT breaking points are plotted in Figs. 2.3(g)-(i) for $l = 2, 4, 8$ respectively. All the states are symmetric in x.

Type B potential:

Fig. 2.4 depicts eigenvalues and eigenmodes of eigenstates for Type B super-Gaussian potential given in Equation (2.4). Figs. 2.4(a)-(c) show the real eigenspectra and Figs. 2.4(d)-(f) depict the imaginary eigenspectra at $l = 2, 4, 8$. $\epsilon_{th}^{(1)}$ and $\epsilon_{th}^{(2)}$ have been given in Table 2.1. As l increases, $\epsilon_{th}^{(1)}$ and $\epsilon_{th}^{(2)}$ remain almost constant for Type B potential. Plots in Figs. 2.4(g)-(i), show the eigenstates before the PT breaking. In PT regime all the eigenstates are found to be symmetric in x direction.

In linear systems with PT-symmetric Gaussian and super-Gaussian potentials, the eigenstates have real eigenvalues for small values of the coefficient of imaginary potentials. Also, corresponding eigenmodes are symmetric in x coordinate. At the threshold values, the eigenvalues are complex and eigenfunctions are asymmetric. In this regime, eigenmodes are symmetric with a single dip at $x = 0$ but 2nd and 3rd excited states have multi dip solutions in PT-symmetric region.

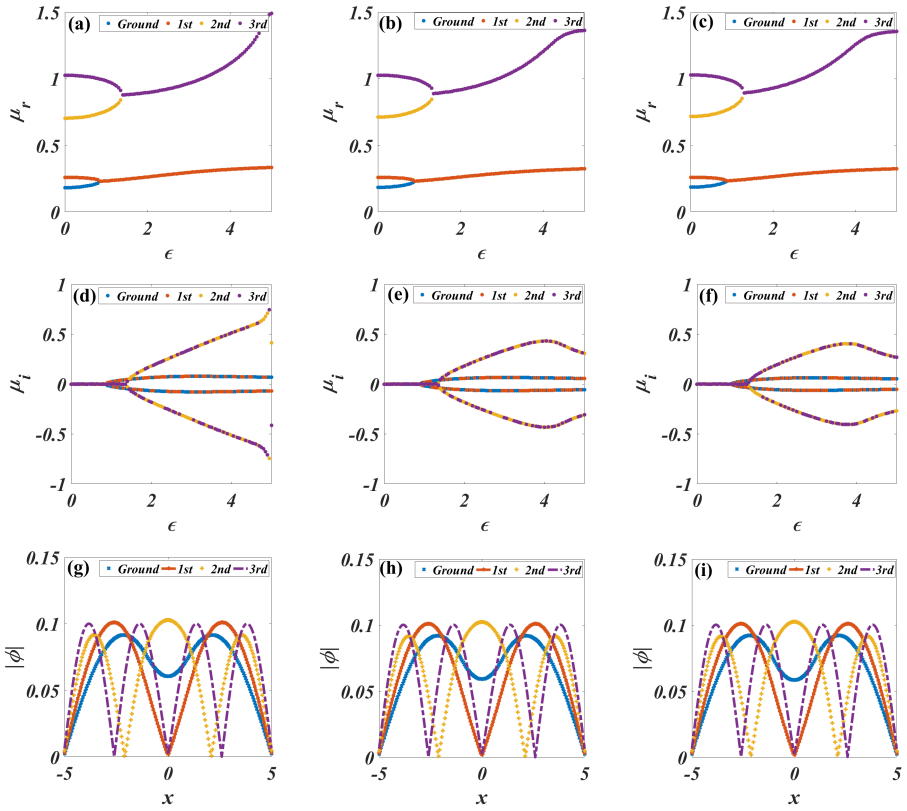

Figure 2.4: The eigenvalues and eigenmodes in super-Gaussian Type B potential in the linear regime. Top panel: The real eigenvalues for (a) $l = 2$ (b) $l = 4$ and (c) $l = 8$. Middle panel: The imaginary eigenvalues (d) $l = 2$, (e) $l = 4$ and (f) $l = 8$. Bottom panel: The eigenfunctions in the $\mathcal{PT}$-symmetric regime ($\epsilon = 0.1$) for (g) $l = 2$,(h) $l = 4$ and (i) $l = 8$.

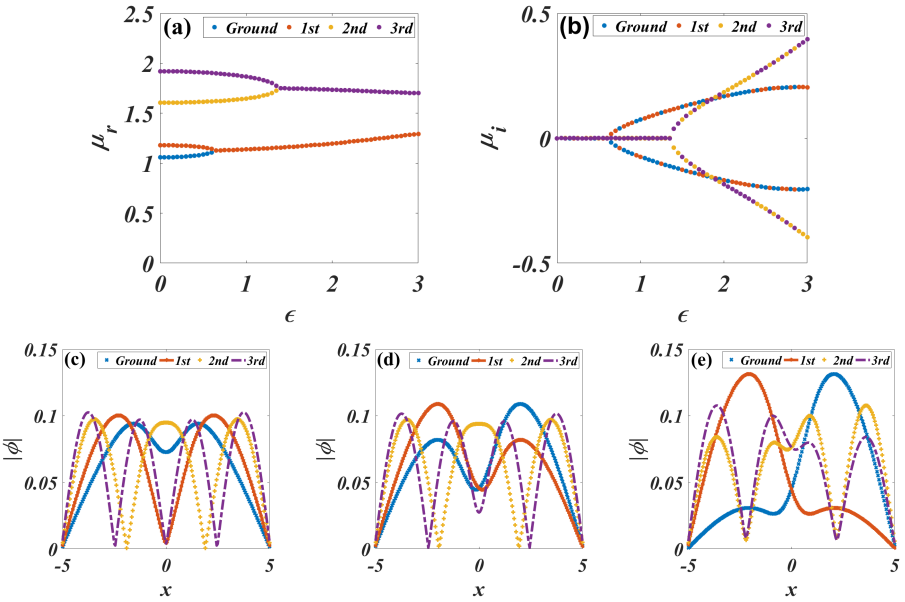

Figure 2.5: The eigenvalue spectrum of ground, 1st, 2nd and 3rd excited states in PT-symmetric Gaussian potential in nonlinear regime. First row: (a) real part of the eigenvalues and (b) imaginary part of the eigenvalues. Second row: the eigenfunctions (c) at $\epsilon = 0.1$, (d) at $\epsilon_{th}^{(1)} = 0.65$ and (e) at $\epsilon_{th}^{(2)} = 1.4$.

2.4.2 Nonlinear regime

The system with Kerr nonlinearity has been studied by solving the eigenvalue problem given as

$$-\frac{d}{2}\frac{d^2\phi}{dx^2} - \beta|\phi|^2\phi - [V_r(x) + iV_i(x)]\phi = \mu\phi. \tag{2.8}$$

The eigenvalue spectra and eigenfunctions of the ground and excited states with gain/loss coefficient in Gaussian and super-Gaussian potentials have been studied in the nonlinear regime.

The changes in real and imaginary components of eigenvalues and eigenmodes with ϵ for ground (blue), 1st excited (red), 2nd excited (yellow) and 3rd excited (purple) states in Gaussian potential are depicted in Fig. 2.5. When ϵ is small, the eigenvalues of all the states are real until it reaches a threshold value, above which the eigenvalues become complex as shown in Figs. 2.5(a) and (b). The threshold value for fundamental and 1st excited states are equal and is called as the first threshold value in the nonlinear regime, $\epsilon_{th}^{(1)}$. For second and third excited states, the threshold value is equal and is termed as the second threshold value in the nonlinear regime,

$\epsilon_{th}^{(2)}$. The threshold values are given in Table 2.2. The regions below and above the threshold values are called the PT-symmetric regime and broken PT-symmetric regime, respectively. Analogous to linear case, all the eigenmodes are symmetric below $\epsilon_{th}^{(1)}$ and $\epsilon_{th}^{(2)}$ as shown in Fig. 2.5(c). At $\epsilon_{th} = \epsilon_{th}^{(1)}$, the ground and 1st excited eigenmodes are asymmetric but 2nd and 3rd excited eigenmodes are symmetric in x-coordinate which is plotted in Fig. 2.5(d). From Fig. 2.5(e), it is observed that at $\epsilon_{th} = \epsilon_{th}^{(2)}$, all the eigenmodes are asymmetric in x.

	Type A				Type B			
l	1	2	4	8	1	2	4	8
$\epsilon_{th}^{(1)}$	0.65	1.05	1.85	3.5	0.65	0.8	0.85	0.8
$\epsilon_{th}^{(2)}$	1.4	2	3.55	6.8	1.4	1.35	1.3	1.25

Table 2.2: The first and second threshold values in Type A and Type B super-Gaussian potential in the nonlinear regime.

Type A potential:

The nonlinear eigenvalue problem given in Equation (2.8) has been solved for $l = 2, 4, 8$ for the potential of the form Type A and its eigenvalues and eigenfunctions are plotted in Fig. 2.6. The real eigenvalues with ϵ for $l = 2, 4, 8$ are shown in Figs. 2.6(a)-(c), respectively. Figs. 2.6(d)-(f) show the imaginary part of the eigenvalues with ϵ for $l = 2, 4, 8$. For small imaginary potential, the eigenvalues of fundamental (blue dots) and 1st eigenmode (red dots) are real. Beyond $\epsilon_{th}^{(1)}$, the values of μ_i begin to grow and are complex conjugates for these two states. Also, second (yellow) and third (purple) states have real eigenvalues for weak imaginary potential and have the same threshold values, $\epsilon_{th}^{(2)}$, for each l. Above the threshold value, the eigenvalues are complex conjugates. The first and second threshold values for $l = 2, 4, 8$ are given in Table 2.2. The eigenfunctions of each mode are symmetric in PT-symmetric region for $l = 2, 4, 8$ as illustrated in Figs. 2.6(g)-(i). Whereas the eigenfunctions are asymmetric in the broken PT-symmetric region as shown in Figs. 2.6(j) and (k). When the parameter l increases the threshold value also increases.

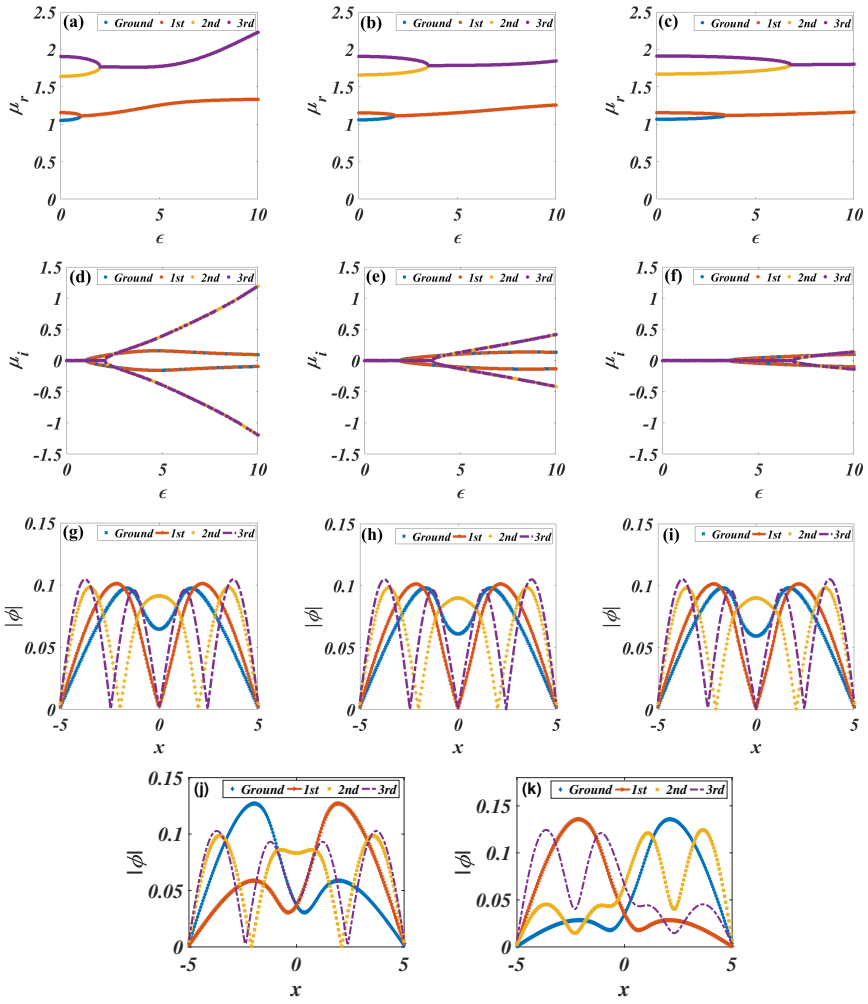

Figure 2.6: The eigenvalue spectrum and eigenmodes in super-Gaussian Type A potential in the nonlinear regime. First row: μ_r with ϵ for (a) $l = 2$, (b) $l = 4$ and (c) $l = 8$. Second row: μ_i with ϵ for (d) $l = 2$, (e) $l = 4$ and (f) $l = 8$. Third row: the eigenstates in PT-symmetric region ($\epsilon = 0.1$) for (g) $l = 2$, (h) $l = 4$ and (i) $l = 8$. Fourth row: the eigenstates in the broken PT-symmetric region for $l = 2$ at (j) $\epsilon_{th}^{(1)} = 1.05$ and (k) $\epsilon_{th}^{(2)} = 2$

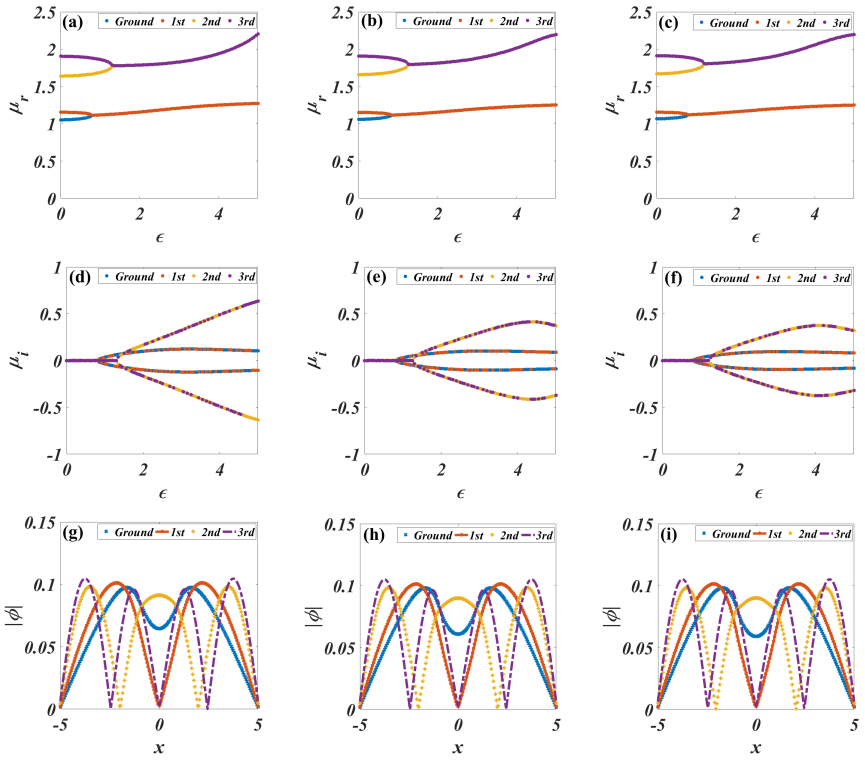

Figure 2.7: The eigenvalues and eigenmodes in super-Gaussian Type B potential in the nonlinear regime. Top panel: μ_r vs ϵ for (a) $l = 2$, (b) $l = 4$ and (c) $l = 8$. Middle panel: μ_i vs ϵ for (d) $l = 2$, (e) $l = 4$ and (f) $l = 8$. Bottom panel: the eigenfunctions in PT-symmetric regime ($\epsilon = 0.1$) for (g) $l = 2$,(h) $l = 4$ and (i) $l = 8$.

Type B potential:

The eigenspectra of the system in super-Gaussian potentials with imaginary part of the form Type B are studied and demonstrated in Fig. 2.7. For $l = 2, 4, 8$ the real eigenvalues with ϵ are plotted in Figs. 2.7(a)-(c) and the imaginary eigenvalues are plotted in Figs. 2.7(d)-(f). For the fundamental and first excited states, the phase transition from PT to broken PT-symmetry occurs at $\epsilon_{th}^{(1)}$, above which imaginary eigenvalues are complex conjugates. Also, the second and third excited states have no imaginary part until $\epsilon_{th}^{(2)}$, beyond which eigenvalues are complex conjugates. Table 2.2 shows the threshold values, $\epsilon_{th}^{(1)}$ and $\epsilon_{th}^{(2)}$, for Type B potentials in the nonlinear regime. Figs. 2.7(g)-(i) show that in PT-symmetric region, all the eigenmodes are symmetric in x. The threshold values remain almost constant with l in this potential. For $\epsilon > \epsilon_{th}$, asymmetric eigenstates are observed in broken PT region for PT-symmetric Type A and Type B potentials.

In super-Gaussian Type A and Type B potentials, the nonlinear modes have real eigenvalues for a low value of gain/loss coefficient and complex conjugate eigenvalues are emerged at the threshold values. Also, eigenmodes are symmetric in PT regime for both the potentials. A dissipative nonlinear system with low loss, admits dark soliton solution by the effective balancing of the gain/loss term with the nonlinearity. In the nonlinear regime, the ground and 1st excited states have single dark soliton solutions and higher eigenmodes have multi dark soliton solutions.

The variation of the threshold values with the parameter l for potentials of the form, Type A and Type B, have been plotted in Fig. 2.8(a) in linear regime and in Fig. 2.8(b) in nonlinear regime. In both the regimes, the threshold value increases linearly with l for Type A potential, but it becomes almost constant in Type B potential. Also, it is found that $\epsilon_{th}^{(2)} > \epsilon_{th}^{(1)}$ in Type A and Type B potentials for given l.

The variation of the threshold value with the coefficient of real potential, k, for Gaussian and super-Gaussian potentials in linear and nonlinear regimes has been illustrated in Fig. 2.9. Blue and red lines, respectively, give $\epsilon_{th}^{(1)}$ and $\epsilon_{th}^{(2)}$ in the linear regime. Yellow and purple colours implies $\epsilon_{th}^{(1)}$ and $\epsilon_{th}^{(2)}$, respectively, in the nonlinear regime. Fig. 2.9(a) shows that for Gaussian potential as k increases the

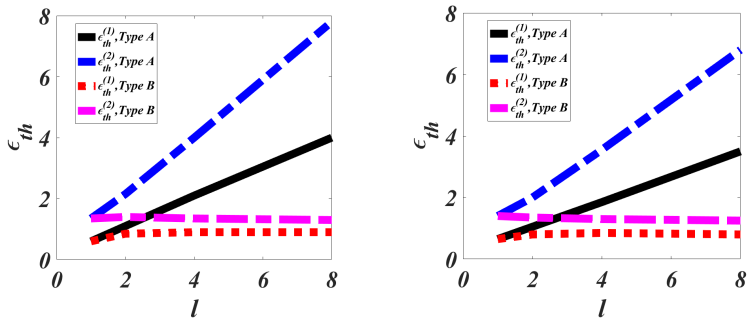

(a) Linear (b) Nonlinear

Figure 2.8: ϵ_{th} vs l for Type A and Type B potentials in (a) linear regime and (b) nonlinear regime. Solid black line for $\epsilon_{th}^{(1)}$ and dashed blue line for $\epsilon_{th}^{(2)}$, in Type A . Dotted red line for $\epsilon_{th}^{(1)}$ and dashed magenta line for $\epsilon_{th}^{(2)}$, respectively, in Type B.

first and second threshold values decrease in both the regimes. For $l = 2, 4, 8$, the variation of $\epsilon_{th}^{(1)}$ and $\epsilon_{th}^{(2)}$ with k value in Type A potential has been illustrated in Figs. 2.9(b)-(d) and that for Type B in Figs. 2.9(e)-(g). In both the cases, the results are analogous to Gaussian potential, i.e. the threshold value decreases with k. For nonlinear modes the threshold value is higher than that in the linear regime and the second threshold is greater than the first threshold if the other parameters are fixed.

2.5 Linear stability analysis

The stability of the fundamental dark soliton solution in Gaussian potential has been analysed for solutions with small perturbations [15, 16]. The stability of the stationary state has been studied by considering the perturbation of the form:

$$\psi(x, z) = [\phi(x) + a(x, z)] \exp(-i\mu z) \tag{2.9}$$

where $a(x, z) = p(x) \exp(i\lambda z) + q(x) \exp(-i\lambda^* z)$. Here, $p(x)$ and $q(x)$ are the perturbation eigenfunctions and λ is the growth rate of the perturbation. The stability

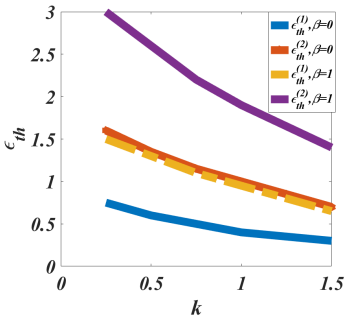

(a) Gaussian

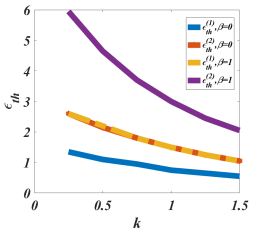

(b) Type A, $l = 2$

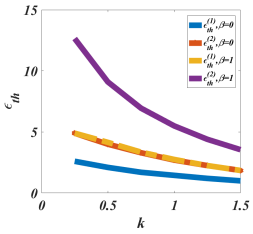

(c) Type A, $l = 4$

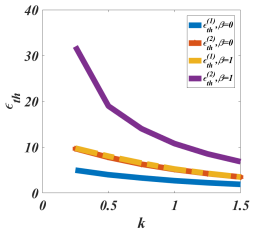

(d) Type A, $l = 8$

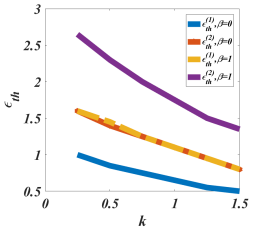

(e) Type B, $l = 2$

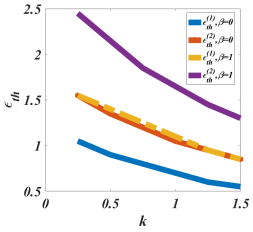

(f) Type B, $l = 4$

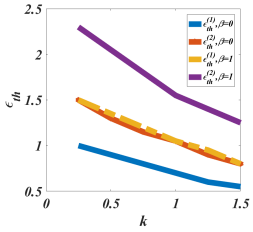

(g) Type B, $l = 8$

Figure 2.9: The variation of threshold values with k for Gaussian, Type A and Type B super-Gaussian potentials in linear and nonlinear regimes. First row: (a) for Gaussian potential, second row: for Type A with (b) $l = 2$ (c) $l = 4$ (d) $l = 8$ and third row: for Type B with (e) $l = 2$ (f) $l = 4$ (g) $l = 8$. Blue and red lines for $\epsilon_{th}^{(1)}$ and $\epsilon_{th}^{(2)}$, respectively, in linear regime and yellow dotted and purple solid lines for $\epsilon_{th}^{(1)}$ and $\epsilon_{th}^{(2)}$, respectively, in nonlinear regime.

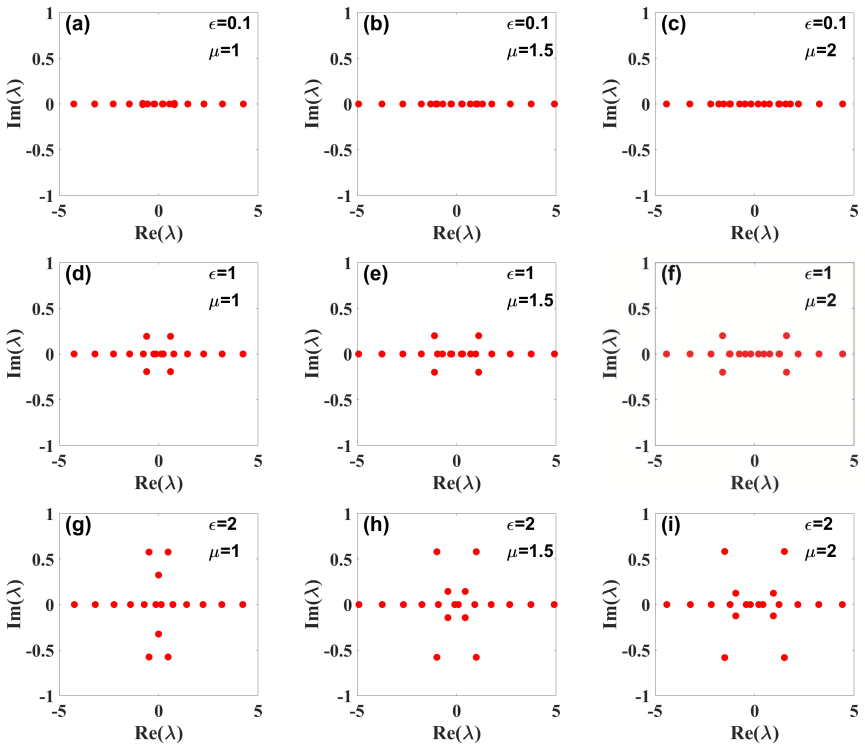

Figure 2.10: The stability eigenvalue spectrum in the nonlinear regime for Gaussian potential for (a) $\epsilon = 0.1, \mu = 1$ (b) $\epsilon = 0.1, \mu = 1.5$ (c) $\epsilon = 0.1, \mu = 2$ (d) $\epsilon = 1, \mu = 1$ (e) $\epsilon = 1, \mu = 1.5$ (f) $\epsilon = 1, \mu = 2$ (g) $\epsilon = 2, \mu = 1$ (h) $\epsilon = 2, \mu = 1.5$ (i) $\epsilon = 2, \mu = 2$.

has been analysed using linearised Bogoliubov-de Genes(BDG) equations,

$$\lambda \begin{bmatrix} p \\ q^* \end{bmatrix} = \begin{bmatrix} L_1 + iV_i & \beta\phi^2 \\ -\beta(\phi^*)^2 & -(L_1 + iV_i) \end{bmatrix} \begin{bmatrix} p \\ q^* \end{bmatrix}, \tag{2.10}$$

where $L_1 = \mu + \frac{d}{2}\frac{\partial^2}{\partial x^2} + 2\beta|\phi|^2 + V_r(x)$. Equation (2.10) has been studied numerically to analyse the stability of the solutions. If $Im(\lambda) = 0$, the fundamental soliton is linearly stable. For complex eigenvalues, an oscillatory instability (OI) exists. The eigenvalues with $Im(\lambda) > 0$ and $Im(\lambda) < 0$ correspond to exponentially decaying and growing modes, respectively. If there is any purely imaginary eigenvalue, the solution is completely unstable due to the exponential amplification of the noise. Fig. 2.10 shows the eigenvalues of fundamental eigenmode by varying the coefficient of imaginary potential and the propagation constant. For low values of ϵ, i.e. in the region of PT-symmetry, all the eigenvalues are real and the solutions are linearly stable as shown in Figs. 2.10(a)-(c). When the coefficient of imaginary potential is greater than a threshold value, i.e. in the broken PT-symmetric region, the eigenvalues are complex and the eigenmodes show OI. The eigenvalues appear in quartet with values λ, λ^*, $-\lambda$ and $-\lambda^*$ as depicted in Figs. 2.10(d)-(f). When ϵ increases again, more quartets with higher imaginary parts are formed and the solutions show OI as plotted in Figs. 2.10(h) and (i), but Fig. 2.10(g) shows the presence of pure imaginary eigenvalues leading to completely unstable solutions. The second and third rows of Fig. 2.10 show that as μ increases $|Re(\lambda)|$ of the quartet also increases.

The stability of the perturbation eigenfunctions for real and complex eigenvalues has been illustrated in Fig. 2.11. The amplitudes of eigenfunctions, $|p|$ and $|q|$, have been discussed for low values of the gain/loss coefficient in Figs. 2.11(a) and (b) and for high values of ϵ in Figs. 2.11(c) and (d), respectively. The profiles are symmetric for low value of imaginary potential ($\epsilon = 0.1$) and in the region of instability ($\epsilon = 1$) eigenfunctions become asymmetric, in x direction. The value of $|q|$ is negligible compared to the value of $|p|$. The stability of soliton holds valid independent of the values of μ, l and of potentials of Type A or Type B.

We analysed the stability of dynamical states by adding Gaussian noise of magni-

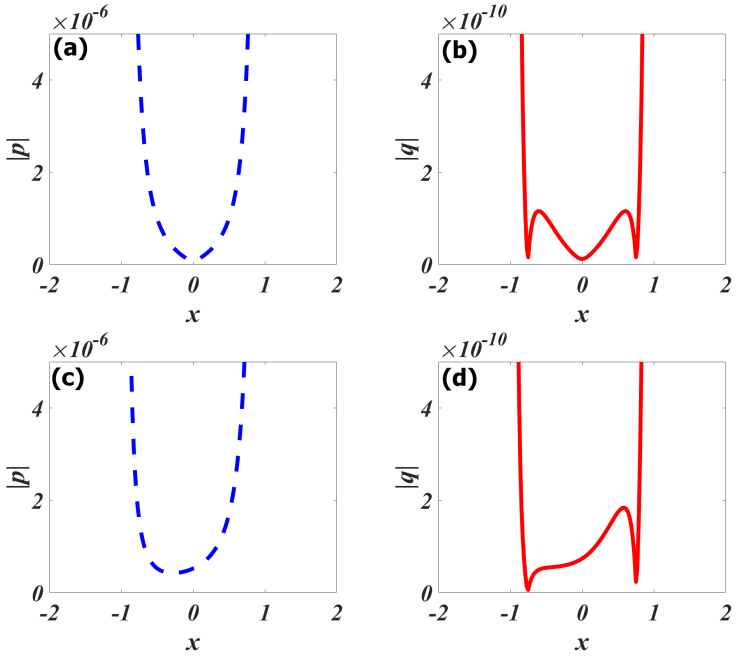

Figure 2.11: Profiles of the perturbation eigenfunctions in x coordinate for Gaussian potential in the nonlinear regime. Top panel: (a) $|p|$ vs x for $\epsilon = 0.1$ and (b) $|q|$ vs x for $\epsilon = 0.1$, bottom panel: (c) $|p|$ Vs x for $\epsilon = 1$ and (d) $|q|$ Vs x for $\epsilon = 1$.

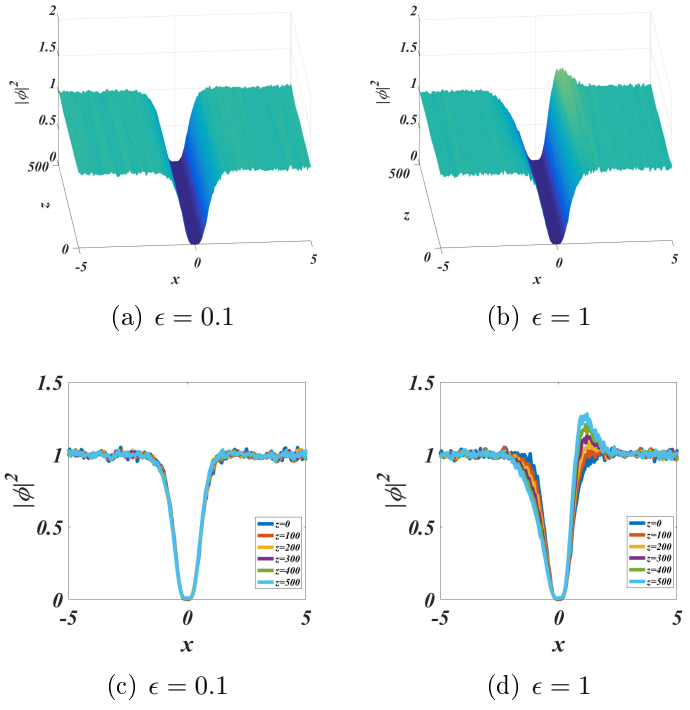

(a) $\epsilon = 0.1$ (b) $\epsilon = 1$

(c) $\epsilon = 0.1$ (d) $\epsilon = 1$

Figure 2.12: The stability of dynamical states in the presence of noise in PT-symmetric Gaussian potential. Top panel: the propagation dynamics at (a) $\epsilon = 0.1$ and (b) $\epsilon = 1$. Bottom panel: the transverse profiles of the solution at (c) $\epsilon = 0.1$ and (d) $\epsilon = 1$.

tude 1% of the soliton amplitude. The representative results in Gaussian potentials with low and high values of ϵ have been shown in Fig. 2.12. For low value, the dark soliton is stable as shown in Figs. 2.12(a) and (c). For high value, the soliton loses its spatial symmetry as depicted in Figs. 2.12(b) and (d). The studies show that at low values of the imaginary potential, soliton preserves its shape and amplitude during propagation but the stability gets broken at high values of the gain/loss.

2.6 Conclusion

In this chapter, we have investigated the existence of 1-D dark soliton with PT-symmetric potential in linear and nonlinear regimes. We studied the system by choosing the PT system with a super-Gaussian real part and the imaginary part in two different profiles. The phase transition from PT to broken PT-symmetry occurs at a threshold value of the coefficient of imaginary potential. In linear regime, the eigenvalues of the fundamental and excited states are real below the respective threshold values, above which eigenvalues are complex. The eigenmodes are symmetric in the transverse direction in PT-symmetric region and their symmetry gets broken at the threshold values. The threshold values are the same for ground and first excited states and have solutions with a single dip. Whereas, for second and third excited states the threshold values are the same and have solutions with multi dips. The study has been extended to the system with defocusing Kerr nonlinearity, where the threshold values are higher than that in the linear regime. The coefficient of nonlinearity enhances the PT-symmetry in the system. The phase transition from PT-symmetry to broken PT-symmetry occurs at the same threshold value for fundamental and first eigenstates and have single dark soliton solutions. Whereas, for 2nd and 3rd eigenstates, the phase transition occurs at a threshold value higher than that of ground and first excited states and have multi dark soliton solutions. In both linear and nonlinear cases, the threshold value increases with the power of the exponential term when the imaginary part is the derivative of the real part of the potential, which is the Type A form. But, in both the regimes, the threshold value is almost constant for the imaginary profile of the other form, Type B. Also,

when the coefficient of the real part of the potential increases the threshold value decreases in both the regimes. The linear stability analysis shows that the stationary solutions are stable for the PT-symmetric modes. The dark soliton dynamics in the presence of noise have been studied and the results show that the soliton is stable during propagation in PT-symmetric region.

Chapter 3

The eigenmodes of self-defocusing nonlinear system with k-wavenumber Scarf II potential

3.1 Introduction

Latest fibre communication technology has made significant progress in building optical nanostructures and artificial device engineering, which has achieved control over many effects in photonics. Experimental realisation of optical fibre networks and solid-state waveguides with adjustable refractive indices is an active area of present research. In linear PT-symmetric models, the presence of real eigenvalues in the PT-symmetric region and complex conjugate pairs of eigenvalues in the broken PT-symmetric region are predicted analytically [37, 38]. The formation of stable bright solitons in PT-symmetric potentials such as Gaussian [39], super-Gaussian, hyperbolic Scarf II [40] and Rosen-Morse [41, 42] potentials in nonlinear optical systems were investigated. Gross-Pitaevskii equations with Wadati class of potentials are of interest when studying the PT-symmetric systems [43, 44]. PT-symmetric soliton models with Kerr nonlinearity in single [45–47] and coupled systems [48, 49] have been studied extensively. Apart from Kerr nonlinear system, different kinds of nonlinear models such as nonlocal [50], variable coefficient [51], parabolic law [52],

cubic-quintic [53], cubic-quartic [54], quintic-septimal [55, 56] and cubic-quintic-septimal [57] nonlinear Schrodinger equations leading to different types of soliton solutions have been studied. Fractional soliton [58, 59], symmetric and antisymmetric solitons [60] have been discussed in fractional NLS [61–63] with PT-symmetric potential.

Analytical and numerical solutions of the bright solitons with PT-symmetric Scarf II potential are studied widely, as the losses in the medium have been effectively compensated. Non-Hermitian Scarf II potential and PT breaking mechanism in one-dimensional linear Schrodinger equation have been discussed [64]. Studies on the soliton propagation along waveguides whose index of refraction perturbed by PT Scarf II potential is reported [65]. A unified theory is proposed for bright soliton solutions in focusing and defocusing nonlinear media with PT-symmetric k-wavenumber Scarf II and multi-well Scarf II potentials [66]. The nonlinear system with a class of PT-symmetric potentials that generalises the classical Scarf II potential in 1D and 2D settings has been studied [67]. Nonlinear modes and dynamical stability of higher-dimensional soliton with PT-symmetric generalised Scarf II potential have been addressed recently [68]. The presence of stable soliton families in non-PT-symmetric complex potential has also been proposed [69, 70].

The dark soliton is more promising and more robust transmission carrier than a bright soliton as it shows slow broadening and less proneness to disturbances during the transmission [71]. The noise affects the intensity of the pulse center of the bright soliton whereas the noise disturbs only the wave background of the dark soliton. Due to these unique properties, the dark soliton has versatile applications in photonics. Dark soliton dynamics, stability, interactions, phase dynamics, ultrashort dark soliton, vector dark solitons, their tunnelling effects etc. in nonlinear lossless and lossy media are theoretically explored [72–75]. Relevant studies on the dark-bright vector soliton in fibre ring lasers [76], robust dark topological valley Hall edge soliton [77], dark soliton families in quintic nonlinear lattices [78] and dark gap solitons in nonlinear media with fourth-order dispersion [79] are reported recently. The dark gap solitons in Bose-Einstein codensates trapped by optical lattices are predicted both in defocusing cubic [80] and quintic [81] nonlinearities. Current non-

linear researches have revealed flat floor bubbles, flat waist dark soliton and flat waist vortices [82]. Even though the properties of dark soliton in the nonlinear medium have been studied, PT-symmetric dark soliton and applications are not much explored. Dark solitons and vortices in PT-symmetric nonlinear media and phase transition are discussed earlier. Recently, the stable modes of dark solitons are observed in nonlinear Kerr medium with PT-symmetric super-Gaussian potential [83]. The studies on the eigenmodes with k-wavenumber Scarf II potential in defocusing nonlinear Kerr medium have significant applications in all-optical gates and other switching circuits.

In this chapter, we study the stationary solutions, propagation and stability of the eigenstates under localised PT-symmetric k-wavenumber Scarf II potential in linear and self-defocusing nonlinear media. The chapter focuses on the effect of the imaginary potential on the symmetry of the ground and first excited states in the PT-symmetric regime. The threshold value of the phase transition from PT-symmetry to broken PT-symmetry has been discussed. The chapter is organised as follows: Section 3.2 describes the theoretical model of 1-D NLSE in k-wavenumber Scarf II potential with defocusing Kerr nonlinearity. The stationary states in linear and nonlinear regimes are analysed in Section 3.3. The stability of the stationary solution has been studied using linear stability analysis in Section 3.4. The features of the dynamical evolution of the solutions in the PT-symmetric regime are reported in Section 3.5. The chapter is concluded in Section 3.6.

3.2 Theoretical model

1D optical beam evolution through a Kerr nonlinear medium with PT-symmetric refractive index distribution is governed by a normalised NLSE,

$$i\frac{\partial\psi}{\partial z} + \frac{d}{2}\frac{\partial^2\psi}{\partial x^2} + \beta|\psi|^2\psi + [V_r(x) + i\ V_i(x)]\psi = 0 \tag{3.1}$$

where ψ is the amplitude of the beam. $\beta < 0$ represents self-defocusing nonlinearity. The real and imaginary components of the PT-symmetric complex potential satisfy

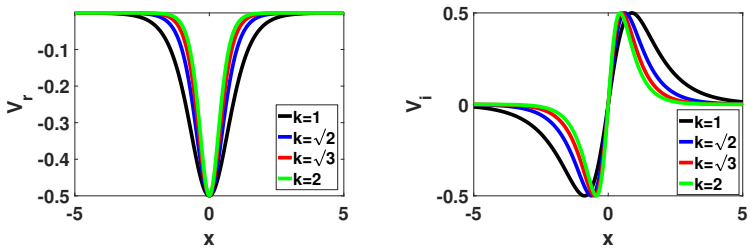

(a) Real (b) Imaginary

Figure 3.1: k-wavenumber Scarf II potential for different k values at $v = -0.5$ and $\epsilon = 1$.

the condition for PT-symmetry. Physically, $V_r(x)$ is associated with refractive index variation while $V_i(x)$ represents the gain/loss distribution in the optical medium. In this work, we study stationary nonlinear modes and propagation in k-wavenumber Scarf II potential.

PT-symmetric k-wavenumber Scarf II potential has real and imaginary parts of the form

$$V_r(x) = v\ \mathrm{sech}^2(kx) \tag{3.2}$$

$$V_i(x) = \epsilon\ \mathrm{sech}(kx)\tanh(kx), \tag{3.3}$$

where $k > 0$ denotes the wavenumber which modulates the width of the potential. The coefficient of the real part, v, refers to the amplitude of the real potential and the coefficient of the imaginary part, ϵ, gives the strength of gain/loss distribution. $v < 0$ means the real part is a potential well and if $v > 0$ it is a potential barrier. From Fig. 3.1 it is evident that as k increases the width of the potential reduces. At $k = 1$, the complex potential becomes the usual PT-symmetric Scarf II form. The real potential has symmetric and the imaginary component has antisymmetric profiles.

3.3 The eigenmodes

The stationary states of the system have been studied in linear and nonlinear cases. We look for the propagation-invariant solution, ϕ, of Equation (3.1) using Ansatz,

$$\psi(x, z) = \phi(x)\mathrm{e}^{-i\mu z}. \tag{3.4}$$

Where μ is the propagation constant. Equations (3.1) and (3.4) lead to the nonlinear eigenvalue equation,

$$\mu\phi = -\frac{d}{2}\frac{d^2\phi}{dx^2} - \beta|\phi|^2\phi - [V_r(x) + i\ V_i(x)]\phi. \tag{3.5}$$

The complex term in Equation (3.5) gives rise to complex eigenvalues. The eigenvalues of the ground and first excited states using Equation (3.5) have been studied. The influence of the coefficient of the imaginary part of the PT-symmetric potential (gain/loss coefficient ϵ) on the eigenmodes and eigenvalues has been analysed. Also, the effects of the width of the potential (k) and the depth of the real potential well (v) on the PT-symmetric phase transition have been studied.

3.3.1 Linear regime

The eigenvalue equation in the absence of Kerr nonlinearity has the form

$$\mu\phi = -\frac{d}{2}\frac{d^2\phi}{dx^2} - [V_r(x) + i\ V_i(x)]\phi. \tag{3.6}$$

Equation (3.6) has been analysed to find the effect of the coefficient of the imaginary potential on the eigenvalue spectra and eigenmodes of the ground and 1st excited states. The solutions of the linear eigenvalue equation have been analysed at different potential widths by taking $k = 1, \sqrt{2}, \sqrt{3}, 2$ and an optimised parameter range for the depth of the real potential well, v.

The intensity profiles of the eigenmodes of the fundamental (blue) and 1st (red) eigenstate by varying the transverse coordinate (x = -5 to 5) in the linear medium have been plotted as shown in Fig. 3.2. When the imaginary potential is small ($\epsilon = 0.2$), both the eigenmodes are symmetric in x-direction for $k = 1, \sqrt{2}, \sqrt{3}, 2$ as shown in Figs. 3.2(a)-(d). At $\epsilon = \epsilon_{th}$, the symmetry of the eigenfunction in the x-axis gets broken as illustrated in Figs. 3.2(e) and (f). In the unbroken PT regime, the ground and first excited states have symmetric eigenmodes with single dip.

The μ_r and μ_i values are plotted against ϵ, in PT potential as shown in Figs. 3.3(a)-(d). Blue and red coloured dots indicate the eigenvalues of the fundamental and first excited states, respectively. For PT-symmetric k-wavenumber Scarf II

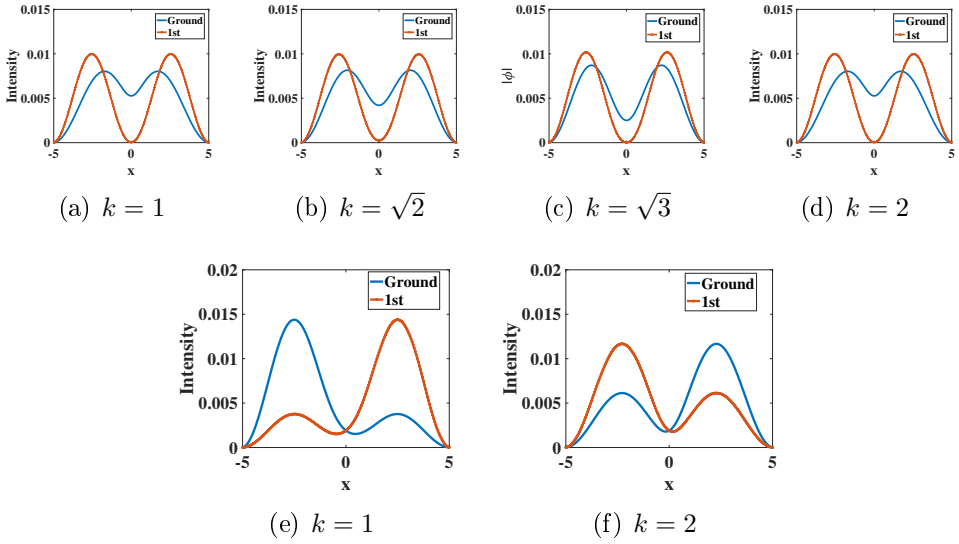

(a) $k = 1$ (b) $k = \sqrt{2}$ (c) $k = \sqrt{3}$ (d) $k = 2$

(e) $k = 1$ (f) $k = 2$

Figure 3.2: The eigenfunctions of ground and first excited states in the unbroken and broken PT-regimes for the linear case at $d = 0.05$ and $v = -0.5$. Top panel: for $\epsilon = 0.2$ (unbroken) and bottom panel: for $\epsilon = \epsilon_{th}$ (broken).

potential, it has been found that for low values of ϵ, the ground and first excited states have distinct real eigenvalues until ϵ_{th}, at which the imaginary eigenvalues become nonzero. For $\epsilon \geq \epsilon_{th}$, the eigenvalues of ground and first excited states become complex conjugate pairs and the PT-symmetry is spontaneously broken. The region below the threshold value is called the unbroken PT-symmetric regime and the region above it is called the broken PT-symmetric regime. Fig. 3.3 shows that as the parameter k increases the threshold value also increases, i.e. narrowing the potential enhances the PT-symmetry.

3.3.2 Nonlinear regime

The eigenvalue equation in the defocusing nonlinear Kerr medium has the form:

$$-\frac{d}{2}\frac{d^2\phi}{dx^2} - \beta|\phi|^2\phi - [V_r(x) + iV_i(x)]\phi = \mu\phi, \tag{3.7}$$

where β is the coefficient of Kerr nonlinearity. The effect of the gain/loss coefficient on the eigenvalue spectra and eigenfunctions of the stationary states of ground and first excited modes in defocusing nonlinear optical Kerr medium with k-wavenumber Scarf II potential has been analysed. We have studied Equation (3.7), numerically,

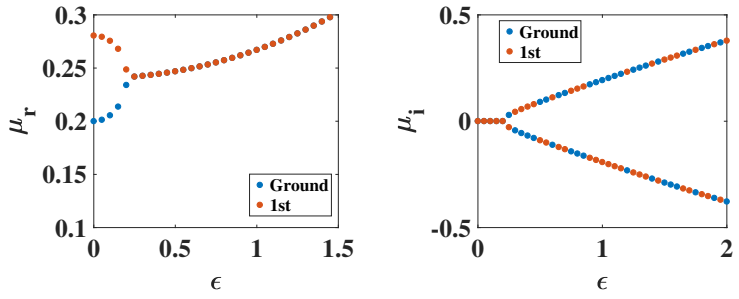

(a) $k = 1$

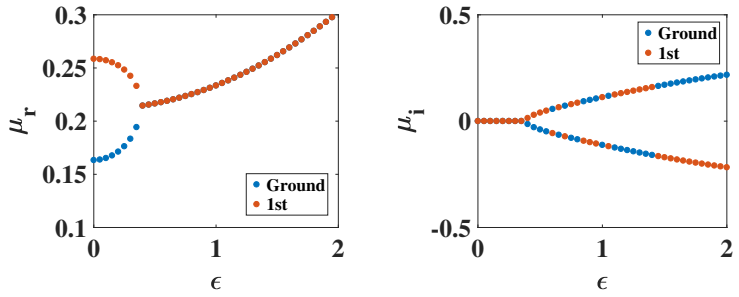

(b) $k = \sqrt{2}$

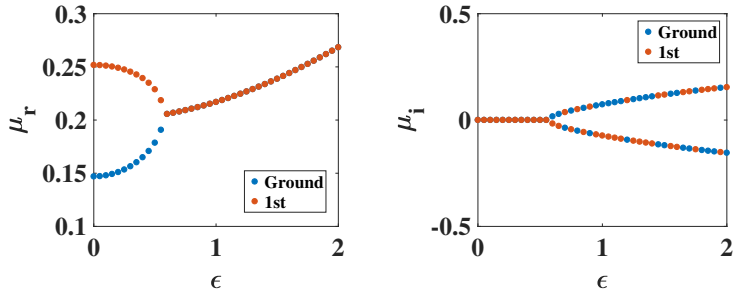

(c) $k = \sqrt{3}$

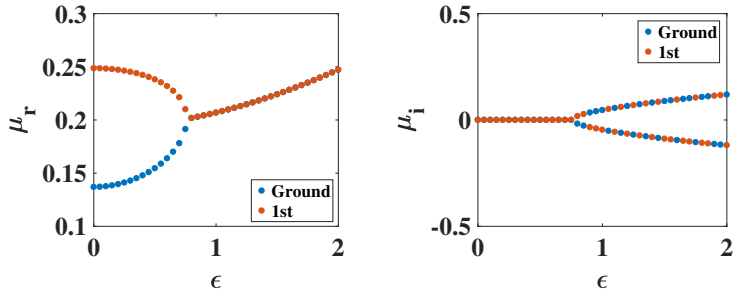

(d) $k = 2$

Figure 3.3: The eigenvalue spectra (μ_r, μ_i) of the ground and first excited states in the linear regime at $d = 0.05$. Real and imaginary eigenvalues with varying ϵ at $v = -0.5$ for (a) $k = 1$ (b) $k = \sqrt{2}$, (c) $k = \sqrt{3}$ and (d) $k = 2$.

by choosing initial profiles such as Gaussian, squared hyperbolic tangent and the exact localised solution of the Wadati model of Scarf II potential for both ground and first excited states.

The solutions are single dip symmetric modes in the unbroken PT regime for some parametric regions of k and v. The solutions have the same form for all the chosen initial Ansatze but with different parametric ranges. The eigenvalues and eigenfunctions with Gaussian profile as the input have been depicted in Figs. 3.4 and 3.5, respectively.

The real and imaginary parts of the eigenvalues of the ground (blue) and 1st excited (red) states have been illustrated in Fig. 3.4. Figs. 3.4(a)-(d) show the real and imaginary parts of the eigenvalues for $k = 1, \sqrt{2}, \sqrt{3}$ and 2. For small values of ϵ, the eigenvalues are real ($\mu_i = 0$) for the fundamental and first excited states. At $\epsilon \geq \epsilon_{th}$, the eigenvalues of ground and 1st excited states become complex conjugate pairs. Above the threshold value, $|\mu_i|$ increases linearly with ϵ.

The intensity profiles of the eigenfunctions by varying the transverse coordinate (x =-5 to 5) have been depicted in Fig. 3.5. The blue plot, having a nonzero intensity dip at $x = 0$, represents the ground state of the system which is grey soliton-like solution. The red plot, with zero intensity dip at $x = 0$, indicates the 1st excited state of the system which is black soliton-like solution. The grey soliton and black soliton are two types of the dark soliton [84, 85]. The intensity dips are confined in the region $[\frac{-x}{2}\ \frac{x}{2}]$. The eigenfunctions are plotted for a small value of ϵ ($\epsilon < \epsilon_{th}$) for $k = 1, \sqrt{2}, \sqrt{3}$ and 2. The fundamental and first excited eigenstates have symmetric eigenfunctions below the threshold values as shown in Figs. 3.5(a)-(d). But a phase transition from PT-symmetry to broken PT-symmetry occurs at $\epsilon = \epsilon_{th}$. The eigenfunctions are asymmetric in the x-axis for $\epsilon \geq \epsilon_{th}$ which is shown in Figs. 3.5(e) and (f). The ground and first excited states have single dip eigenmodes in the unbroken PT regime.

From Fig. 3.4, it is evident that as the parameter k increases the threshold value also increases in the nonlinear regime which means that narrowing the real and imaginary potentials enhances the PT-symmetry in both linear and nonlinear regimes. By comparing Figs. 3.3 and 3.4, it is clear that the threshold value is

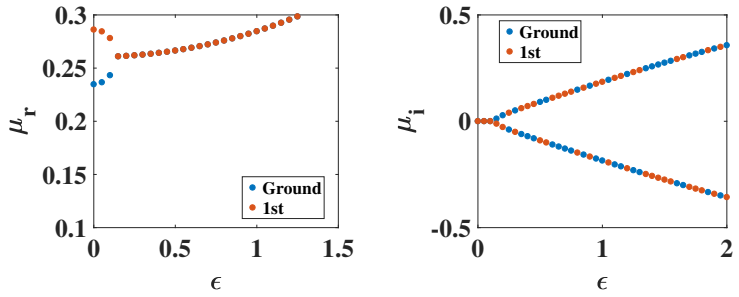

(a) $k = 1$

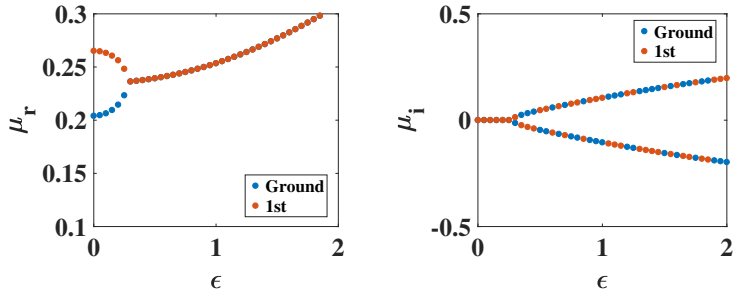

(b) $k = \sqrt{2}$

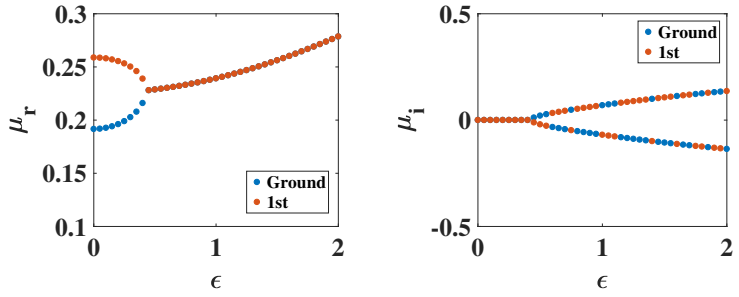

(c) $k = \sqrt{3}$

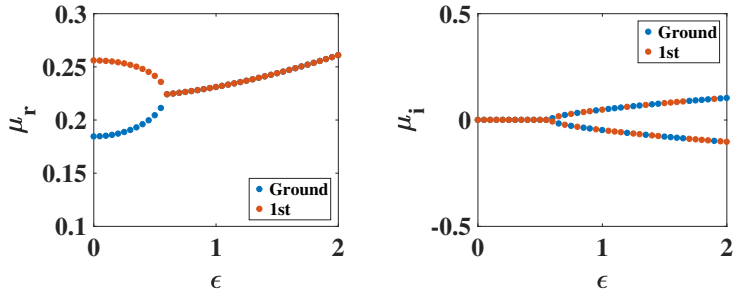

(d) $k = 2$

Figure 3.4: The eigenvalue spectra (μ_r, μ_i) of the ground and first excited states in the nonlinear regime at $\beta = -0.1$ and $d = 0.05$. The real and imaginary eigenvalues with ϵ at $v = -0.5$ for (a) $k = 1$, (b) $k = \sqrt{2}$, (c) $k = \sqrt{3}$ and (d) $k = 2$.

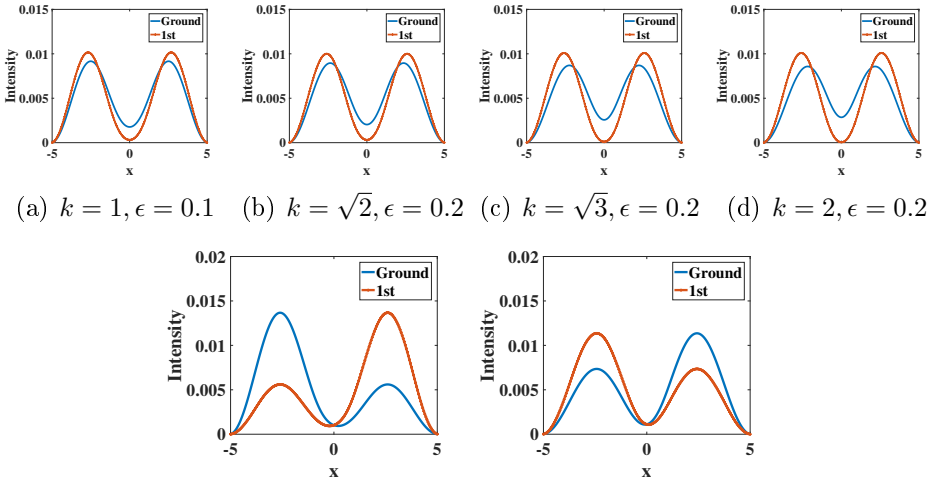

(a) $k = 1, \epsilon = 0.1$ (b) $k = \sqrt{2}, \epsilon = 0.2$ (c) $k = \sqrt{3}, \epsilon = 0.2$ (d) $k = 2, \epsilon = 0.2$

(e) $k = 1, \epsilon = 0.15$ (f) $k = 2, \epsilon = 0.6$

Figure 3.5: The eigenfunctions of ground (blue) and first excited (red) states in the unbroken PT-symmetric (top panel) and broken PT-symmetric (bottom panel) regimes for the nonlinear case ($\beta = -0.1$) at $v = -0.5$ and $d = 0.05$ with Gaussian input.

lower in the nonlinear regime, i.e., the defocusing nonlinearity suppresses the PT-symmetry.

3.3.3 The PT phase transition

We analyse the dependence of the variables k, v and β on the PT phase transition point in the linear and nonlinear regimes. The variation of the threshold values with the width of the potential for these cases is shown in Fig. 3.6(a). The red and black solid lines show that as k increases the threshold value increases in both the regimes, i.e. narrowing the potential profile results in the enhancement of the PT-symmetry. The threshold value versus the coefficient of nonlinearity at $k = 1$ (blue) and $k = 2$ (red) are plotted in Fig. 3.6(b). From the figure, it is clear that the threshold value is highest when $\beta = 0$ (linear). In the nonlinear regime, as the coefficient of self-defocusing nonlinearity increases the threshold value decreases. The interplay between the defocusing nonlinearity and PT-symmetric potential suppresses the PT-symmetry. The effect of the coefficient of the real part of the k-wavenumber Scarf II potential, v, on the threshold values at $k = 1, \sqrt{2}, \sqrt{3}$ and 2 in linear and nonlinear regimes have been plotted in Figs. 3.6(c) and (d). In these figures, the blue dashed line, green solid line, red dotted line and black solid line indicate the threshold values

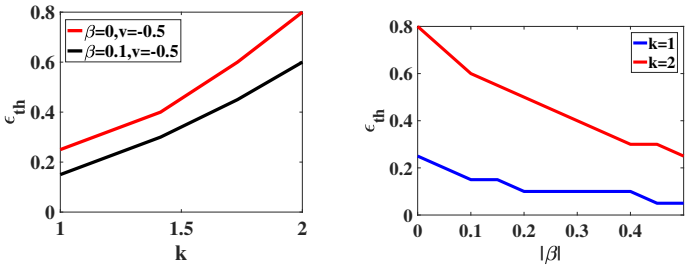

(a) at $v = -0.5$ (b) at $v = -0.5$

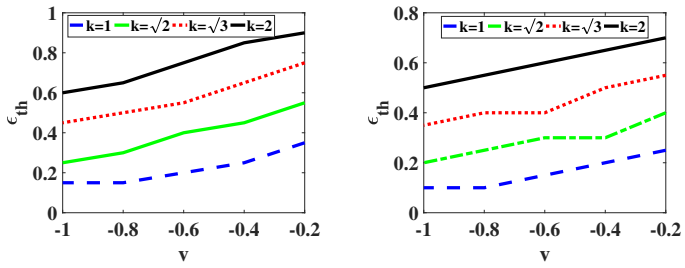

(c) Linear (d) Nonlinear

Figure 3.6: The variation of the threshold values with different parameters of the system k, v and β in the linear and nonlinear systems at $d = 0.05$. (a) ϵ_{th} Vs k at $v = -0.5$ (b) ϵ_{th} vs β at $v = -0.5$ (c) ϵ_{th} vs v for the linear case and (d) ϵ_{th} vs v for the nonlinear case.

for $k = 1$, $k = \sqrt{2}$, $k = \sqrt{3}$ and $k = 2$, respectively. It is clear that both in the linear and nonlinear regimes the threshold values increases with decreasing $|v|$, i.e., the threshold values decrease with increasing the depth of the real potential well.

3.4 Linear stability analysis

The stability properties of the stationary states of fundamental and first excited states of nonlinear eigenmodes in k-wavenumber Scarf II potential have been analysed. The stability has been analysed using linearised BDG equations. Fig. 3.7 shows the perturbation eigenspectra in linear and nonlinear regimes for the fundamental (blue) and first (red) eigenstates. For the linear case, in the PT-symmetric regime ($\epsilon = 0.1$) the perturbation eigenvalues are real and the solutions are stable as shown in Figs. 3.7(a) and (b). When $\epsilon = 1$ (broken PT), the solutions show oscillatory instability due to the presence of the imaginary component and Figs. 3.7(c) and (d) show that the perturbation eigenvalues of the ground and 1st excited states are in quartets of $\lambda, \lambda^*, -\lambda$ and $-\lambda^*$.

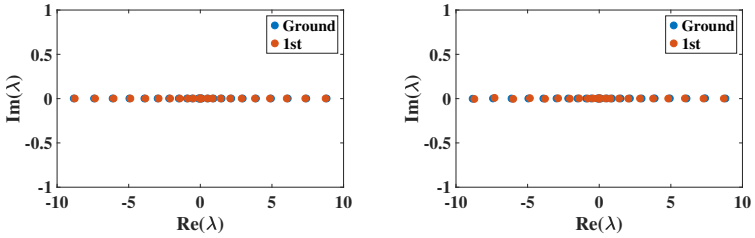

(a) $k = 1, \epsilon = 0.1$ (b) $k = 2, \epsilon = 0.1$

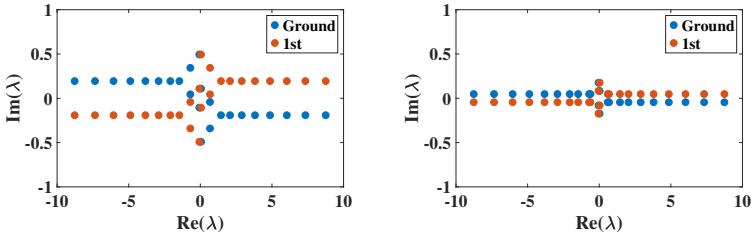

(c) $k = 1, \epsilon = 1$ (d) $k = 2, \epsilon = 1$

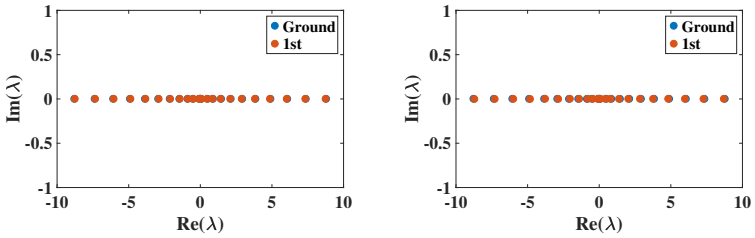

(e) $k = 1, \epsilon = 0.1$ (f) $k = 2, \epsilon = 0.1$

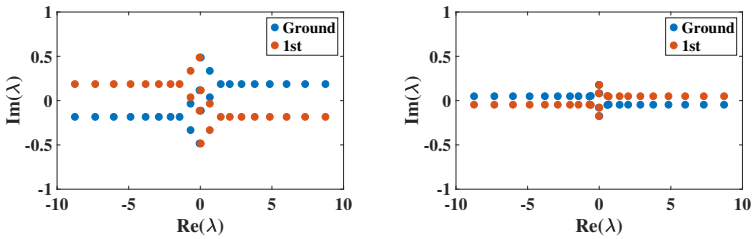

(g) $k = 1, \epsilon = 1$ (h) $k = 2, \epsilon = 1$

Figure 3.7: The perturbation eigenvalues of the stationary states of ground and 1st excited modes in PT-symmetric ($\epsilon = 0.1$) and broken PT ($\epsilon = 1$) regimes for linear and weak nonlinearity ($\beta = -0.1$) at $d = 0.05, v = -0.5$. The first two rows for the linear case and the last two rows for the nonlinear case.

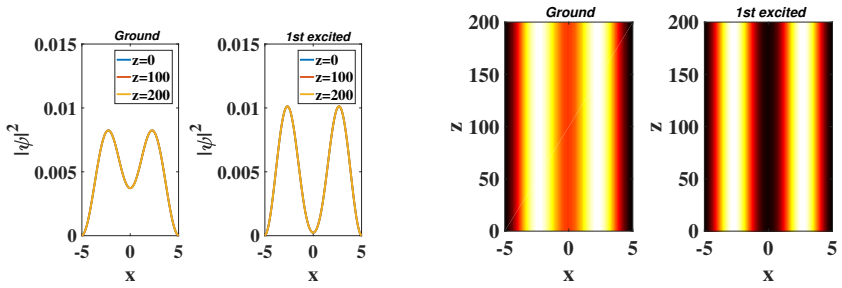

(a) $\epsilon = 0.1, z = 200$

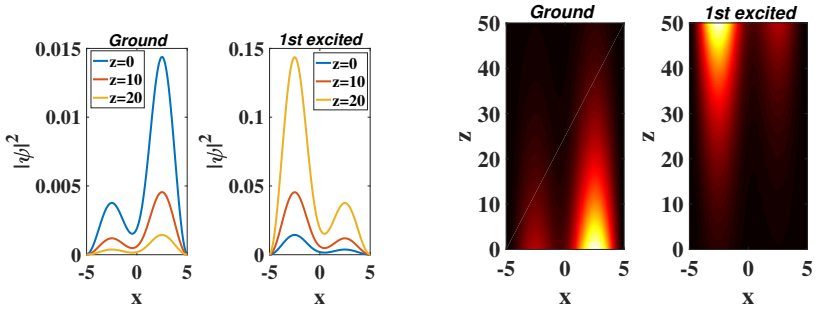

(b) $\epsilon = 0.25, z = 50$

Figure 3.8: Intensity evolution of the linear eigenstates during the propagation in the unbroken and broken PT-symmetric regimes for $k = 1$ at $d = 0.05$ and $v = -0.5$. Upper panel: the ground and 1st excited states in the unbroken regime and lower panel: the ground and 1st excited states in the broken regime.

The bottom panel of Fig. 3.7 gives the perturbation eigenvalues for the nonlinear case. In the unbroken PT system, all the perturbation eigenvalues are purely real and the solutions are linearly stable for both ground and 1st excited states as shown in Figs. 3.7(e) and (f). For $\epsilon = 1$ (broken PT regime), the perturbation eigenvalues of the ground and 1st excited states form quartets of $\lambda, \lambda^*, -\lambda$ and $-\lambda^*$ as illustrated in Figs. 3.7(g) and (h). In this case, the eigenstates show oscillatory instability.

3.5 Propagation of the stationary states

The propagation dynamics of the stationary solution given by Equation (3.5) have been analysed for the ground and first excited states in linear and nonlinear regimes. Dynamical states before and after the PT breaking are analysed.

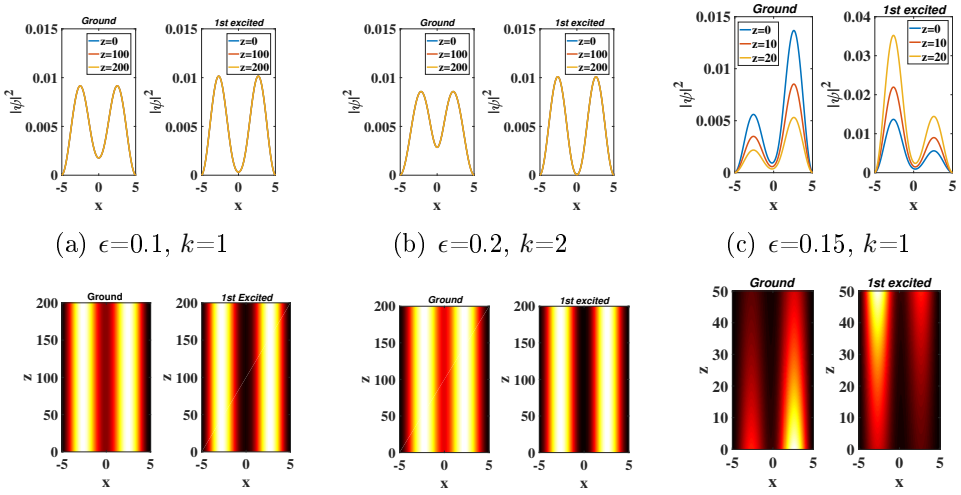

(a) ϵ=0.1, k=1 (b) ϵ=0.2, k=2 (c) ϵ=0.15, k=1

(d) ϵ=0.1, k=1, z=200 (e) ϵ=0.2, k=2, z=200 (f) ϵ=0.15, k=1, z=50

Figure 3.9: Intensity evolution of the nonlinear stationary eigenmodes of ground and first excited states for $k = 1, 2$ with propagation at $d = 0.05, \beta = -0.1$ and $v = -0.5$. (a), (b), (d), (e) in the unbroken PT regime and (c), (f) in the broken PT regime.

3.5.1 Linear regime

The analysis of beam dynamics in the linear regime has been done in the PT and PT broken modes for $k = 1$. It is evident that for small values of the coefficient of the imaginary potential, $\epsilon < \epsilon_{th}$, the propagation of the solution is stable in the z-direction as shown in Fig. 3.8(a). When $\epsilon \geq \epsilon_{th}$, the symmetry of dynamical solutions of the ground and 1st excited states gets broken which is depicted in Fig. 3.8(b). In the PT symmetric regime, the solutions are symmetric in x and z directions. Whereas, in the broken PT regime the solutions are asymmetric in both x and z axes.

3.5.2 Nonlinear regime

The beam evolution of the eigenstates in the nonlinear regime for k-wavenumber Scarf II potential has been illustrated in Fig. 3.9 for $k = 1, 2$. Figs. 3.9(a) and (d) show the dynamical evolution of the eigenstates in the PT regime for $k = 1$. Figs. 3.9(b) and (e) show the evolution of the ground and 1st excited states in the PT-symmetric regime for $k = 2$. The solutions are stable with propagation in the unbroken PT-regime. Above the threshold values of the coefficient of the imaginary

potential, $\epsilon \geq \epsilon_{th}$, the dynamical solutions become unstable in x and z axes as depicted in Figs. 3.9(c) and (f).

3.6 Conclusion

The stationary states of the ground and first excited modes in linear and nonlinear systems with PT-symmetric k-wavenumber Scarf II well potential have been analysed. The linear case admits stable eigenmodes with real eigenspectra in the unbroken PT regime. The nonlinear model with weak defocusing nonlinearity produces stable solutions with real eigenspectra in the PT regime. In the broken PT, the eigenmodes become asymmetric and the eigenvalues of the fundamental and first excited states become complex conjugate pairs in linear and nonlinear cases. The linear stability analysis shows that the solutions are stable in the unbroken PT regime. In k-wavenumber Scarf II potential, the results have shown that, the threshold value of the coefficient of the imaginary part of the PT-symmetric potential, at which the spontaneous breaking of PT-symmetry occurs, depends on the width of the complex potential and the depth of the real potential well. Narrowing the complex potential enhances the PT-symmetry. When the depth of the real potential well decreases the PT-symmetric region increases. The study shows that for self-defocusing nonlinear case, nonlinearity suppresses the PT-symmetry in k-wavenumber Scarf II well potential. In linear and nonlinear models, the evolution of the stationary solutions show a stable propagation in the unbroken PT regime and becomes unstable in the broken PT regime. The existence of nonlinear eigenmodes under PT-symmetric potential find applications in fibre-optic communication processes.

Chapter 4

The eigenstates of the coupled system with equal gain and loss effects

4.1 Introduction

The fundamental and higher eigenmodes of PT-symmetric coupled systems with self-focusing and self-defocusing nonlinearity have significant applications in all-optical switching, non-reciprocal light transmission, active coupling mechanism and unidirectional optical valves [86–88]. In such systems, an efficient compensation of the losses can induce many desirable effects which enhance active light control and the formation of localised modes of signals like bright and dark solitons. Not only the region of PT-symmetry but also the region of broken PT-symmetry is useful [89].

The soliton's steering dynamics in PT-symmetry directional coupler [49] and the dynamics of vector bright and dark solitons using variable coefficient coupled nonlinear Schrodinger equations have been studied widely [90]. The existence of non-local gap solitons with transverse real periodic potential [91, 92] have been studied. Nonlinear modes of PT-symmetric coupler in the presence of saturable nonlinearity and nonlinear gain or loss effects have been proposed [93]. Linear and nonlinear PT-symmetric dimers having the property of unidirectional light transport are

used in on-chip optical diodes. This enhanced relevant studies on nonlinear PT-symmetric trimers and oligomers [94]. The stationary and dynamical states of the PT-symmetric coupler in the presence of transverse periodic and aperiodic potentials have been studied in self-focusing nonlinear systems [95]. In this chapter, fundamental and higher eigenmodes, propagation and power oscillation between channels in PT-symmetric coupled system with self-defocusing nonlinearity are studied using variational analysis and numerical methods.

This chapter is presented as follows: In Section 4.2, the model of the nonlinear PT-symmetric coupled system is described. The eigenvalue equation of the stationary states for high and low-frequency modes are also discussed under this section. The effect of the gain/loss coefficient, self-defocusing nonlinearity and coupling constant on the fundamental and higher eigenstates are discussed in Section 4.3. The propagation dynamics of the eigenstates have been studied in Section 4.4 and Section 4.5 discusses the stability of the nonlinear modes using BDG equations. The two-channel power distribution of the system has been studied using the variational analysis in Section 4.6. Section 4.7 summerises the results and concludes the chapter.

4.2 The stationary solutions

The optical beam propagation of a PT-symmetric coupled system with Kerr nonlinearity is governed by couple of nonlinear Schrodinger equations of the form

$$\begin{aligned} i\psi_z + \tfrac{d}{2}\psi_{xx} + \beta|\psi|^2\psi + iG\psi + C\phi = 0 \\ i\phi_z + \tfrac{d}{2}\phi_{xx} + \beta|\phi|^2\phi - iG\phi + C\psi = 0. \end{aligned} \tag{4.1}$$

Where $\psi(x,z)$ and $\phi(x,z)$ are the mode amplitudes in the medium with gain and loss, respectively. The light beam experiences diffraction in the x-direction and propagates along the z-direction. Subscripts z and xx represent the first derivative in z and second derivative in x, respectively. d, β, G and C are the coefficients of the diffraction, nonlinearity, gain/loss and coupling, respectively.

The eigenvalue equation of the PT-symmetric coupled system with self-

defocusing nonlinearity has been analysed using Ansatze,

$$\psi(x,z) = U(x)\mathrm{e}^{-i(\mu z-\theta_1)} \tag{4.2}$$

and

$$\phi(x,z) = U(x)\mathrm{e}^{-i(\mu z-\theta_2)}, \tag{4.3}$$

which lead to the eigenvalue equation of the form,

$$\mu U = -\frac{d}{2}U_{xx} - \beta|U|^2U - C_{th}U. \tag{4.4}$$

Where $U(x)$ is the steady-state solution and μ implies the propagation constant, $C_{th} = \sqrt{C^2 - G^2} = C\cos\delta$ and $\delta = \theta_1 - \theta_2$. The eigenmodes with $\cos\delta > 0$ refers to high-frequency mode (U_H) and $\cos\delta < 0$ refers to low-frequency mode (U_L).

The eigenvalues and eigenmodes of the ground and excited states in the self-defocusing ($\beta < 0$) nonlinear medium have been studied. Equation (4.4) has been solved using Gaussian input and the influence of the gain/loss coefficient, coupling constant and the coefficient of nonlinearity on the PT-symmetric phase transition are studied.

The real and imaginary eigenvalues of the high and low-frequency modes of the ground, second and fourth excited states by varying the gain/loss coefficient are illustrated in Fig. 4.1. The real eigenvalues, μ_r, for two different values of the coupling constant, C, have been plotted in Figs. 4.1(a) and (b). The green and blue dotted plots in the figures indicate the real eigenvalues of the high and low-frequency modes of the ground state. Both modes have distinct real eigenvalues when $G < C$. At $G = C$, the real eigenvalues of the high and low-frequency modes get merged and become a constant for $G > C$. The imaginary eigenvalues, μ_i, of the ground state are plotted in Figs. 4.1(c) and (d). In the figures, the green and blue dots indicate the high and low-frequency modes, respectively. The imaginary eigenvalues are zero when $G < C$ and $|\mu_i|$ increases with G when $G > C$. It is evident that the eigenvalues are purely real below the threshold value of G (G_{th}), i.e., in the PT phase. Also, the eigenvalues of these modes are complex conjugate

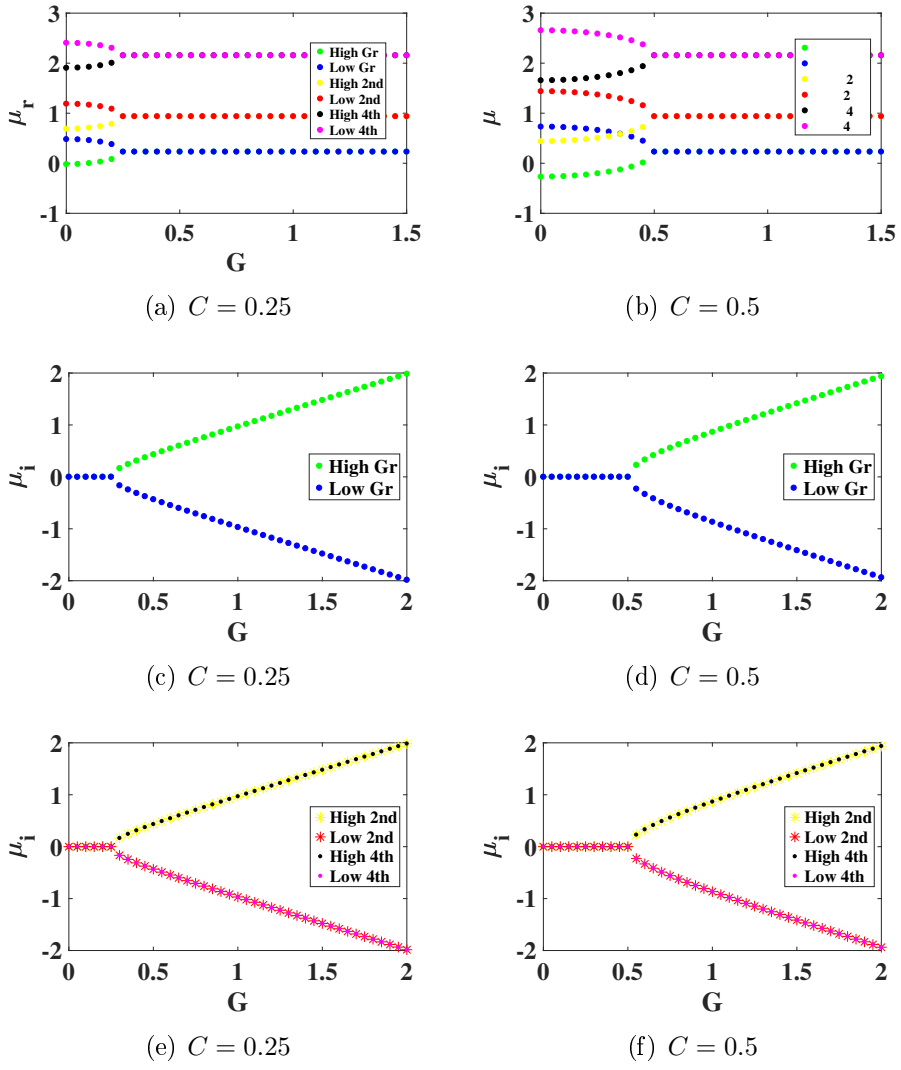

(a) $C = 0.25$ (b) $C = 0.5$

(c) $C = 0.25$ (d) $C = 0.5$

(e) $C = 0.25$ (f) $C = 0.5$

Figure 4.1: The real and imaginary eigenvalues (μ_r and μ_i) of the high and low-frequency modes with gain/loss coefficient for fundamental, 2nd and 4th excited states at $\beta = -4$ and $d = 1$. First column for $C = 0.25$ and second column for $C = 0.5$.

to each other above the threshold value, i.e., in the broken PT-symmetric regime. The real eigenvalue at $G = G_{th}$ is called the threshold real eigenvalue, given as μ_r^{th}.

In Figs. 4.1(a) and (b), the yellow and black dots represent the real eigenvalues of the high-frequency modes of the 2nd and 4th excited states, respectively. Also, the red and magenta dots indicate the real eigenvalues of the low-frequency modes of the 2nd and 4th excited states, respectively. In Figs. 4.1(e) and (f), the yellow and red coloured stars, respectively, represent μ_i values of the high and low-frequency modes of the 2nd excited state. The black and magenta coloured dots of the lower panel of Fig. 4.1 indicate μ_i values of high and low-frequency modes of the 4th excited state. The excited states also show the same behaviour as the ground state. For each eigenstate, the low-frequency mode has a higher eigenvalue than the high-frequency mode in the PT-symmetric regime. In the broken PT regime, for all the eigenstates, the high-frequency modes have positive imaginary eigenvalues and the low-frequency modes have negative imaginary eigenvalues. In the broken PT regime, $|\mu_i|$ values of the all eigenstates are same for a given G.

The intensity profiles of the high and low-frequency eigenmodes of the ground and excited stationary states in the PT-symmetric regime have been shown in Fig. 4.2. The green and blue plots of Figs. 4.2(a)-(c) indicate the high and low-frequency modes of the ground state for different nonlinearity coefficients (β). The figures show that both the high and low-frequency modes have the same eigenfunction. The eigenmodes have a dip at $x = 0$ and the depth of the dip increases as β increases. The high and low-frequency modes of the 2nd excited state are indicated by the yellow and red plots, respectively, in Figs. 4.2(d)-(f), and that of the 4th excited state are indicated by the black and magenta coloured plots, respectively, in Figs. 4.2(g)-(i). Similar to the ground state, the low and high-frequency modes of the states exhibit same eigenfunction. All the nonlinear modes are symmetric in x-direction and for small values of β the eigenmodes of the excited states show a peak at $x = 0$. As the parameter β increases a dip evolves at $x = 0$ and the depth of the dip increases with the nonlinearity coefficient. The analysis has shown that the dips are evolved only for the ground, 2nd and 4th excited states in the self-defocusing nonlinearity.

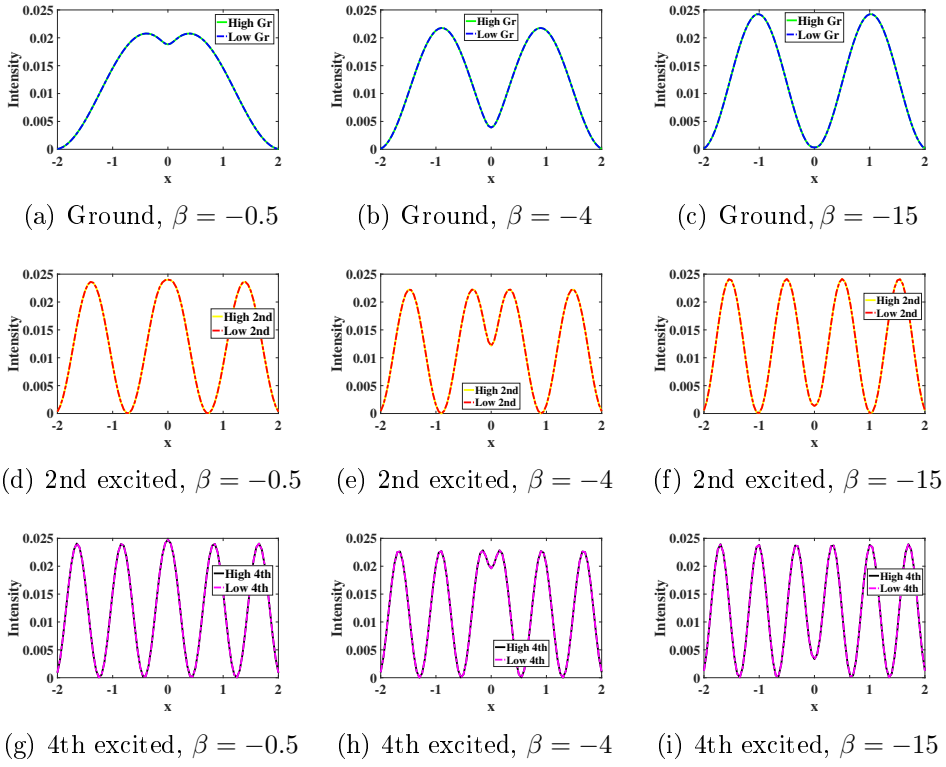

(a) Ground, $\beta = -0.5$ (b) Ground, $\beta = -4$ (c) Ground, $\beta = -15$

(d) 2nd excited, $\beta = -0.5$ (e) 2nd excited, $\beta = -4$ (f) 2nd excited, $\beta = -15$

(g) 4th excited, $\beta = -0.5$ (h) 4th excited, $\beta = -4$ (i) 4th excited, $\beta = -15$

Figure 4.2: The ground and excited eigenstates of the high and low-frequency modes in the PT-symmetric regime for $C = 0.25$, $G = 0.2$ at $d = 1$. First column: for $\beta = -0.5$, second column: for $\beta = -4$ and third column: for $\beta = -15$.

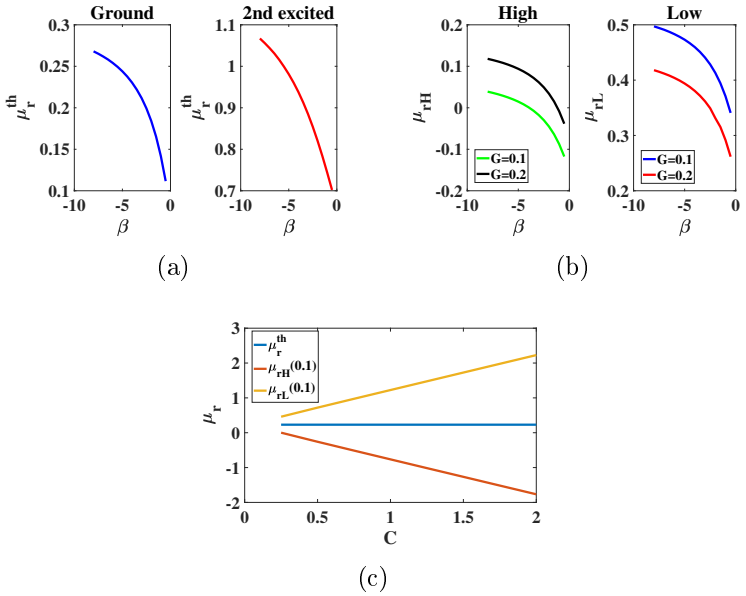

(a) (b)

(c)

Figure 4.3: The variation of the real eigenvalues with the coefficient of nonlinearity and coupling constant. (a) μ_r^{th} vs β at $C = 0.25$, (b) the variation of high and low-frequency real eigenvalues at $C = 0.25$ in PT regime and (c) variation with C at $\beta = -4$.

Fig. 4.3 depicts the effect of the coefficient of nonlinearity and coupling constant on the real eigenvalues. As $|\beta|$ increases μ_r^{th} of the ground and excited states increase which is shown in Fig. 4.3(a). In the PT-symmetric regime, the eigenvalues of the high and low-frequency modes (μ_{rH} and μ_{rL}) are higher for higher values of the parameter β as shown in Fig. 4.3(b). The variation of μ_r with C, illustrated in Fig. 4.3(c), shows that when C increases the threshold real eigenvalue remains constant. In the PT-symmetric regime ($G = 0.1$), the eigenvalue of the high-frequency mode decreases and that of the low-frequency mode increases with C. The excited states also show the same behaviour.

4.3 The propagation of eigenstates

The propagation of the high and low-frequency modes of the ground and excited states in the PT-symmetric and broken PT-symmetric regimes have been studied and are depicted in Fig. 4.4 and Fig. 4.5. The intensity evolution of the high and low-frequency modes of the ground state for $G \leq C$ is as shown in Fig. 4.4(a). The propagation of the high and low modes of the 2nd and 4th states are plotted in Figs. 4.4(b) and (c), respectively. The plots clearly show that low and high-frequency modes of the eigenstates have stable propagation in the PT-symmetric regime.

Fig. 4.5 shows the intensity evolution of the stationary states in the broken PT-symmetric regime ($G > C$). The beam propagation of the high and low-frequency modes of the ground state is shown in Figs. 4.5(a) and (b). The second and third rows of Fig. 4.5 show the propagation dynamics of the excited states. The figures clearly show that the propagation of the eigenmodes becomes unstable with increasing intensity for the high-frequency mode and decreasing intensity for the low-frequency mode in the broken PT-regime.

The variation of the power, P, along the propagation distance, z, before and after the PT-symmetry breaking for the ground state is as shown in Fig. 4.6(a). It is evident that for both high and low-frequency modes, the power is constant in the PT-symmetric regime. Whereas in the broken PT regime, power suddenly

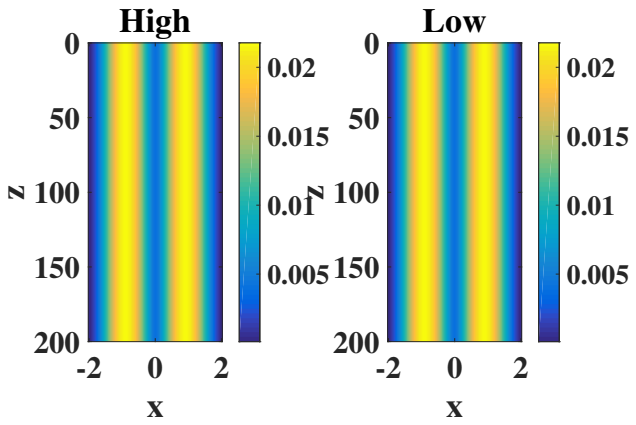

(a) Ground

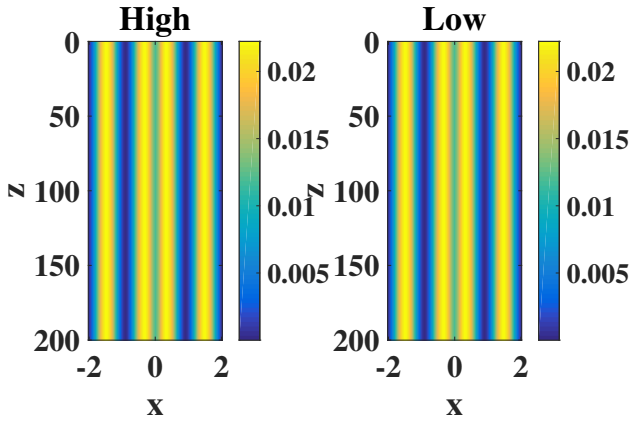

(b) 2nd excited

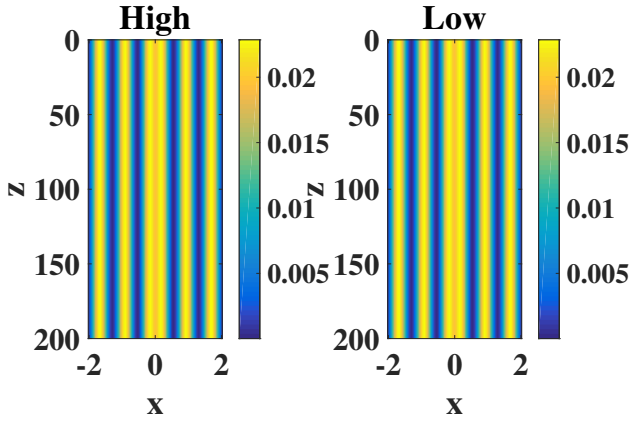

(c) 4th excited

Figure 4.4: The propagation of the high and low-frequency modes of the ground and excited states in the PT-symmetric regime ($G = 0.2$) for $z = 200$ at $C = 0.25$, $\beta = -4$ and $d = 1$.

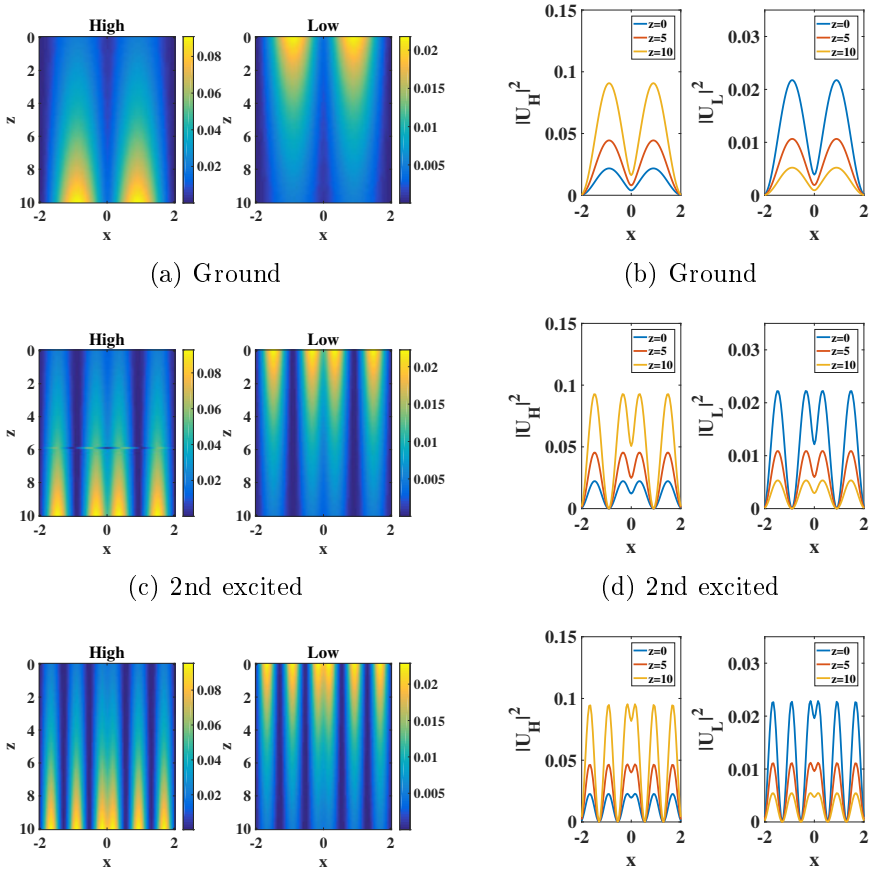

(a) Ground (b) Ground

(c) 2nd excited (d) 2nd excited

(e) 4th excited (f) 4th excited

Figure 4.5: The propagation of the high and low-frequency modes of the ground and excited states in the broken PT-symmetric regime for $C = 0.25, G = 0.26, \beta = -4$ and $d = 1$.

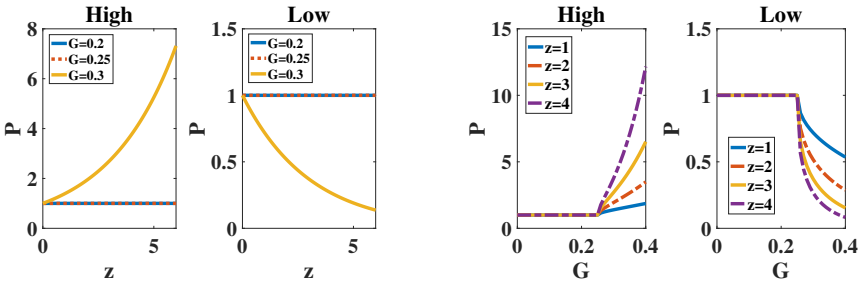

(a) P vs z (b) P vs G

Figure 4.6: The power variation of the high and low-frequency modes of the ground state with the propagation at $C = 0.25$, $\beta = -4$ and $d = 1$. (a) P vs z for different G values and (b) P vs G for different z values.

increases for the high-frequency mode and suddenly decreases for the low-frequency mode. Fig. 4.6(b) shows the power variation with the parameter G at different propagation distances. It verifies that for both the high and low-frequency modes the power is a constant till $G = G_{th}$.

4.4 Linear stability analysis

The stability of the solutions of the ground and excited states of the system has been analysed by considering the effect of small perturbations of the form [96]

$$\begin{aligned}\psi(x,z) &= [U(x) + p_1(x)\exp(i\lambda z) + q_1(x)\exp(-i\lambda^* z)]\mathrm{e}^{-i\mu z} \\ \phi(x,z) &= [U(x) + p_2(x)\exp(i\lambda z) + q_2(x)\exp(-i\lambda^* z)]\mathrm{e}^{-i\mu z},\end{aligned} \tag{4.5}$$

where λ is the growth rate of the perturbation, p_1, q_1 and p_2, q_2 are the perturbation eigenfunctions in the gain and loss media, respectively. The stability has been discussed using linearised BDG equations,

$$\lambda \begin{bmatrix} p_1 \\ q_1^* \\ p_2 \\ q_2^* \end{bmatrix} = \begin{bmatrix} L_1 + iG & \beta U^2 & Ce^{-i\delta} & 0 \\ -\beta U^{*2} & -(L_1 - iG) & 0 & -Ce^{i\delta} \\ Ce^{i\delta} & 0 & (L_1 - iG) & \beta U^2 \\ 0 & -Ce^{-i\delta} & -\beta U^{*2} & -(L_1 + iG) \end{bmatrix} \begin{bmatrix} p_1 \\ q_1^* \\ p_2 \\ q_2^* \end{bmatrix}. \tag{4.6}$$

Where $L_1 = \mu + \frac{d}{2}\frac{d^2}{dx^2} + 2\beta|U|^2$ and $Ce^{i\delta} = \sqrt{C^2 - G^2} + iG$.

The perturbation eigenvalue spectra of the eigenstates are shown in Fig. 4.7. The first row of Fig. 4.7 refers to the perturbation eigenvalue spectrum in the PT-symmetric regime ($G = 0.25$). In this regime, $Im(\lambda) = 0$ and it implies that the solutions are linearly stable. When PT-symmetry gets broken ($G = 0.26$), the eigenstates exhibit oscillatory instability ($Im(\lambda) \neq 0$) as shown in the second row of Fig. 4.7.

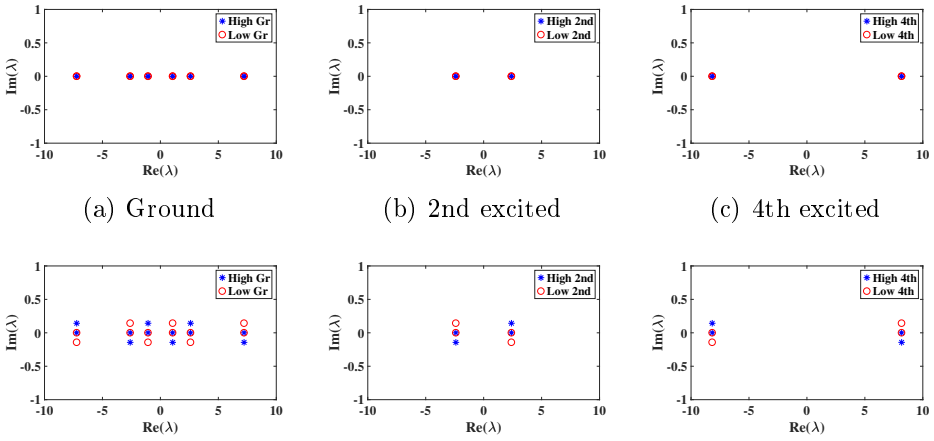

(a) Ground (b) 2nd excited (c) 4th excited

(d) Ground (e) 2nd excited (f) 4th excited

Figure 4.7: Linear stability analysis of the nonlinear modes of the fundamental and higher states at $C = 0.25$, $\beta = -4$ and $d = 1$. Top panel: in the PT-symmetric regime $G = 0.25$ and bottom panel: in the broken PT-regime for $G = 0.26$.

4.5 Variational analysis

Two-channel power distribution is studied using the semi-analytical approach by the variational analysis of Equation (4.1) using the Ansatze,

$$\begin{aligned} \psi(x,z) &= \phi_1(x,z)\mathrm{e}^{-i\mu z}, \\ \phi(x,z) &= \phi_2(x,z)\mathrm{e}^{-i\mu z}. \end{aligned} \tag{4.7}$$

Where ϕ_1 and ϕ_2 are the eigenmodes in the gain and lossy channels. Thus, the eigenvalue equation is given by

$$\begin{aligned} i\phi_{1z} + \frac{d}{2}\phi_{1xx} + \beta|\phi_1|^2\phi_1 + iG\phi_1 + C\phi_2 &= -\mu\phi_1, \\ i\phi_{2z} + \frac{d}{2}\phi_{2xx} + \beta|\phi_2|^2\phi_2 - iG\phi_2 + C\phi_1 &= -\mu\phi_2. \end{aligned} \tag{4.8}$$

Due to the gain/loss terms, total Lagrangian density has a conservative and a non-conservative part. The conservative part is

$$\begin{aligned} L_C = \frac{i}{2}(\phi_{1z}^*\phi_1 - \phi_1^*\phi_{1z}) + \frac{i}{2}(\phi_{2z}^*\phi_2 - \phi_2^*\phi_{2z}) + \frac{d}{2}(|\phi_{1x}|^2 + |\phi_{2x}|^2) \\ -\frac{\beta}{2}(\phi_1^4 + \phi_2^4) - C(\phi_2\phi_1^* + \phi_1\phi_2^*) - \mu(|\phi_1|^2 + |\phi_2|^2)\,. \end{aligned} \tag{4.9}$$

The dynamics of the system is described by Euler-Lagrange equation,

$$\frac{\partial}{\partial z}\frac{\partial L_C}{\partial \phi_{1z}^*} - \frac{\partial L_C}{\partial \phi_1^*} + \frac{\partial}{\partial z}\frac{\partial L_C}{\partial \phi_{2z}^*} - \frac{\partial L_C}{\partial \phi_2^*} = Q_i. \tag{4.10}$$

Where Q_i refers to all dissipative terms in Equation (4.8) and are given by

$$Q_1 = -iG\phi_1, \quad Q_2 = iG\phi_2. \tag{4.11}$$

The reduced Lagrangian is given by

$$< L_c >= \int_{-\infty}^{\infty} L_c dx. \tag{4.12}$$

The form chosen for the variational Ansatz is

$$\phi_j(x,z) = A_j(z)\mathrm{e}^{\frac{-x^2}{2a^2(z)} + i\theta_j(z)}, \tag{4.13}$$

where A_j is the amplitude and θ_j represents the phase which are the variational parameters. $j = 1, 2$ represent Channel 1 and Channel 2, respectively. a is the beam width and is taken as a constant. The power is defined by $p_j = \int_{-\infty}^{\infty} \phi_j \phi_j^* dx$, which is expressed as $p_j = \sqrt{\pi} A_j^2 a$. The ratio of the power in a channel to the total power is defined as its relative power, which is given as $P_j = \frac{p_j^2}{p_1^2 + p_2^2}$. The reduced Lagrangian of Equation (4.9) is

$$\begin{aligned} < L_c >= p_1\theta_{1z} + p_2\theta_{2z} + \frac{d}{4a^2}(p_1 + p_2) - \frac{\beta}{2\sqrt{2\pi}a}(p_1^2 + p_2^2) \\ - \frac{2C\sqrt{p_1 p_2}\ \cos\delta}{a^2} - \mu(p_1 + p_2). \end{aligned} \tag{4.14}$$

For the dissipative system, the variational approach is given by

$$\frac{d}{dz}\frac{\partial < L_c >}{\partial(\eta_{iz})} - \frac{\partial < L_c >}{\partial \eta_i} = 2\ Re \int_{-\infty}^{\infty} \Big(Q_1 \frac{\partial \phi_1^*}{\partial \eta_i} + Q_2 \frac{\partial \phi_2^*}{\partial \eta_i} \Big) dx. \tag{4.15}$$

Where $\eta_i = p_1, p_2, \theta_1$ and θ_2 correspond to parameters that can vary in the variational Ansatz. Using Equations (4.11), (4.14) and (4.15), the variation of the parameters in the two channels are obtained as below:

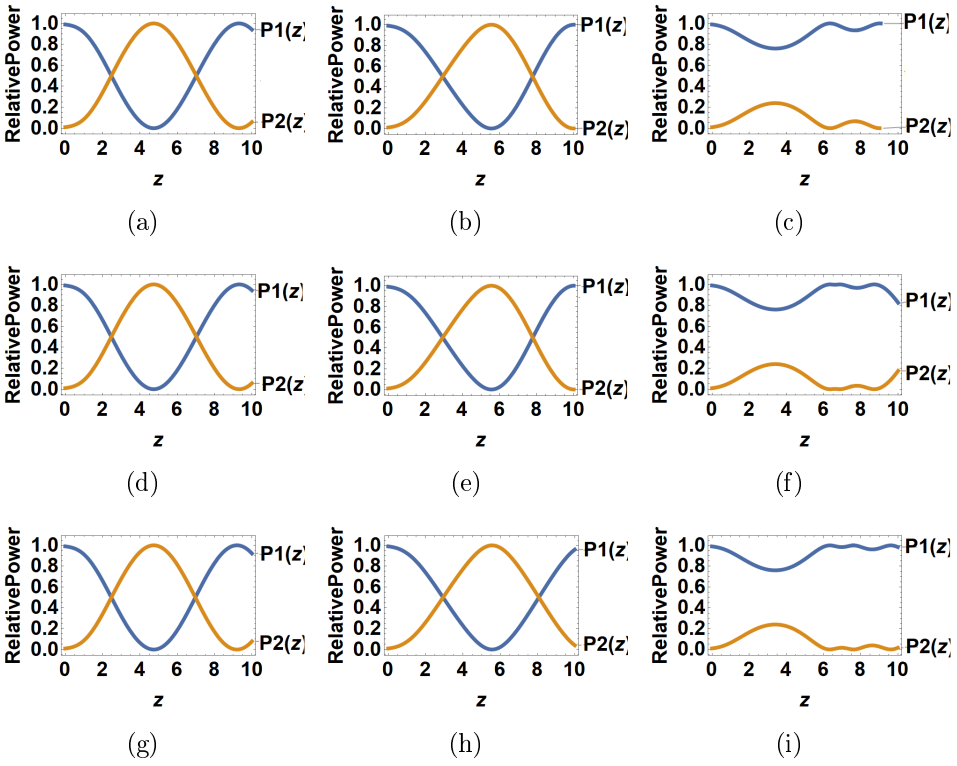

Figure 4.8: Variation of relative power, P_1 and P_2, with z for low-frequency eigenmodes with $P_1(0) = 1$, $P_2(0) = 0.1$ and $\beta = -4$. First column: $C = 0.25$, $G = 0.2$ and second column: $C = 0.25$, $G = 0.25$, represent the eigenmodes below PT-symmetry breaking. Third column: $C = 0.25$, $G = 0.3$, represents the case of eigenmodes in the broken PT-regime. First row: ground state, second row: second excited state and third row: fourth excited state.

$$\frac{dp_1}{dz} = -2C\sqrt{p_1 p_2}\sin\delta + 2Gp_1, \tag{4.16}$$

$$\frac{dp_2}{dz} = 2C\sqrt{p_1 p_2}\sin\delta - 2Gp_2, \tag{4.17}$$

$$\frac{d\theta_1}{dz} = -\frac{d}{4a^2} + \frac{\beta p_1}{\sqrt{2\pi}a} + 2Ca\sqrt{\frac{p_2}{p_1}}\cos\delta + \mu, \tag{4.18}$$

$$\frac{d\theta_2}{dz} = -\frac{d}{4a^2} + \frac{\beta p_2}{\sqrt{2\pi}a} + 2Ca\sqrt{\frac{p_1}{p_2}}\cos\delta + \mu. \tag{4.19}$$

Equations (4.16)-(4.19) have been studied numerically and the relative power of the eigenmodes in both channels are studied for various values of the gain/loss coefficients.

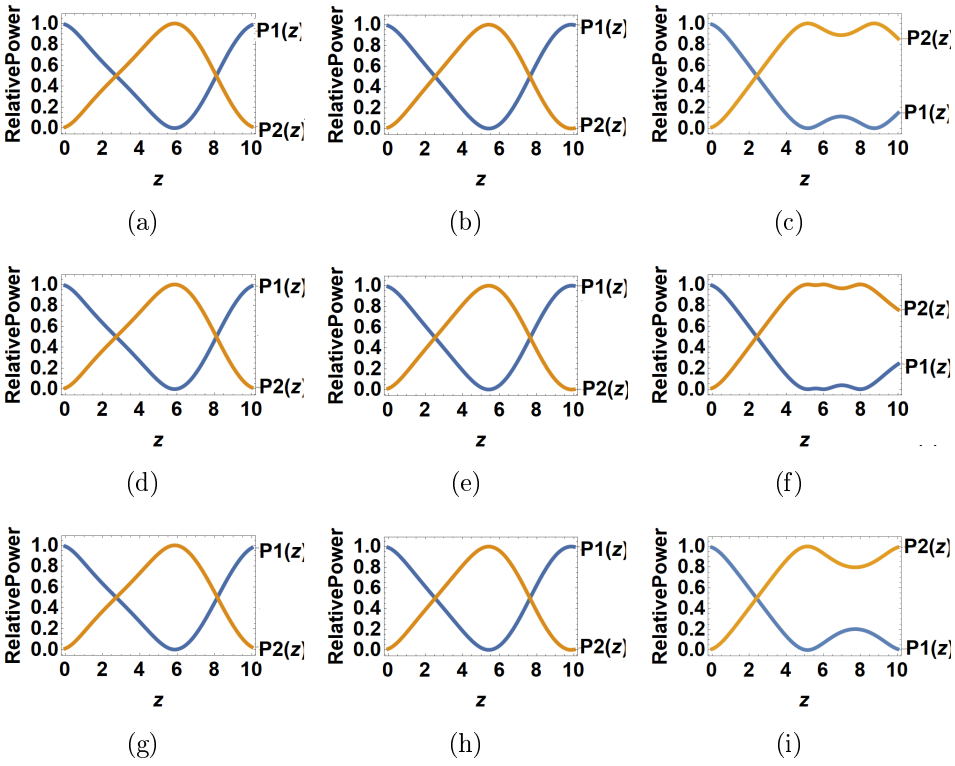

Figure 4.9: Variation of P_1 and P_2 with z for high-frequency eigenmodes with $P_1(0) = 1$, $P_2(0) = 0.1$ at $\beta = -4$. First column: $C = 0.25$, $G = 0.2$ and second column: $C = 0.25$, $G = 0.25$, represent the eigenmodes below the PT-symmetry breaking. Third column: $C = 0.25$, $G = 0.3$, represents the eigenmodes in the broken PT regime. First row: ground state, second row: second excited state and third row: fourth excited state.

4.5.1 Power oscillation

Fig. 4.8 shows the relative power of the low-frequency modes of the eigenstates. The orange and blue plots indicate relative power in Channel 1 and Channel 2, respectively. Column 1 represents the case below the PT breaking and column 2 is the case at the threshold value of PT breaking. In these two cases, the propagation constant is real. Columns 1 and 2 show that the power from Channel 1 transfers to Channel 2 at a coupling length which results in the periodic variation of the power. Column 3 shows the relative power of the eigenmodes after the PT breaking, where the propagation constant is complex. In this case, there is no power transfer between the two channels and the power remains in the excited channel itself as shown in the third column.

The relative power carried by high-frequency modes of the eigenstates in the two

channels is shown in Fig. 4.9. The first and second columns show the variation of the relative power of the eigenmodes below the PT-symmetry breaking. The power in the first channel transfers to the second channel at a coupling length $L_c = \frac{\pi}{2C}$. In the broken PT symmetric regime, power switches between the channels and then confines in a single channel. After the switching, there is a slight oscillation in power in two channels.

4.6 Conclusion

This chapter analyses the stationary eigenmodes of the ground and excited states in PT-symmetric coupled system with self-defocusing nonlinearity. Purely real eigenvalues are obtained if the coupling constant is greater than the gain/loss coefficient, i.e., in the PT phase. In this regime, the low and high-frequency modes have the same eigenfunction. For low values of the defocusing nonlinearity, the fundamental eigenmode shows a central dip whereas excited modes show central peaks. As the nonlinearity strength increases a dip evolves for the higher eigenmodes. Above the threshold value of the gain/loss coefficient, i.e., in the broken PT regime, the eigenvalues of the high and low modes become complex conjugates. As the strength of the defocusing nonlinearity increases the threshold eigenvalue increases while as the coupling constant increases the threshold eigenvalue remains constant. The propagation dynamics shows that beam evolution of the eigenstates are stable and the power remains constant in the PT regime. When PT-symmetry gets broken, propagation becomes unstable and power increases for the high-frequency mode whereas it decreases for the low-frequency mode. The linear stability analysis verified that the stationary eigenmodes are stable in the PT regime. In a two-channel system, the relative power periodically oscillates between the channels in the PT regime. In the broken PT regime, power switches between the channels and then confines in a single channel in the case of high-frequency modes. For the low-frequency modes, there is no power transfer between the channels in the broken PT regime. The PT-symmetric modes in the self-defocusing nonlinear medium find applications in developing optical nanostructures and switching devices.

Chapter 5

The switching dynamics with k-wavenumber Scarf II potential

5.1 Introduction

Nonlinear coupled Schrodinger equation with PT-symmetry supports families of localised waves with real eigenvalue spectra. The realisation of different profiles of complex PT-symmetric potentials such as super-Gaussian, Rosen-Morse, Scarf II, sextic anharmonic double-well [97] etc. are achieved by effectively amalgamating an antisymmetric gain/loss distribution on an even refractive index profile. PT-symmetric nonlinear coupled systems enhance advanced light steering techniques that find applications in directional couplers, all-optical switches, non-reciprocal light transmission, etc. Stable bright soliton formation in the PT-symmetric coupled NLSE with self-focusing nonlinearity are studied, extensively. However, PT coupled systems with self-defocusing nonlinearity are yet to be explored. The self-regulation of the refractive index through defocusing nonlinearity affects the localised nonlinear modes in the PT-symmetric systems. PT-symmetric coupled optical systems in the defocusing nonlinear medium with k-wavenumber Scarf II potential find applications in optical switching devices.

In this chapter, we analyse the linear and nonlinear eigenmodes of the PT-symmetric coupled system and its switching dynamics. Section 5.2 describes the

model of the coupled system and the stationary solutions in the self-defocusing nonlinear medium. The PT phase transition, the effect of nonlinearity and the linear stability analysis are discussed in this section. In Section 5.3, the power switching dynamics of the beam between the gain and lossy channels are analysed. The chapter is concluded in Section 5.4.

5.2 The stationary solution

The optical beam evolution in a nonlinear coupled system with PT-symmetric transverse potential has the form

$$\begin{aligned} i\psi_z + \tfrac{d}{2}\psi_{xx} + \beta|\psi|^2\psi + (V_r + iV_i)\psi + C\phi = 0 \\ i\phi_z + \tfrac{d}{2}\phi_{xx} + \beta|\phi|^2\phi + (V_r - iV_i)\phi + C\psi = 0, \end{aligned} \tag{5.1}$$

where $\psi(x,z)$ and $\phi(x,z)$ are the beam envelopes in gain and lossy channels, respectively. d, β and C represent the coefficients of diffraction, nonlinearity and coupling. $\beta < 0$ implies the self-defocusing nonlinearity. The real and imaginary parts of the PT-symmetric k-wavenumber Scarf II potential has the form

$$V_r = v\ \mathrm{sech}^2(kx) \tag{5.2}$$

and

$$V_i = \epsilon\ \mathrm{sech}(kx)\ \tanh(kx), \tag{5.3}$$

where v and ϵ are the strength of the real and imaginary parts of potential. V_r has potential well form when $v < 0$. The wavenumber, k, tunes the width of the potential. In this work, we study the system with k-wavenumber Scarf II potential having $k = 1, 3, 5$, for $v < 0$. When $k = 1$, the potential has Scarf II form. The potential width is small when k is large. The real potential has symmetric and the imaginary component has antisymmetric profiles.

The eigenvalue equation is obtained from Equation (5.1) taking solutions in the

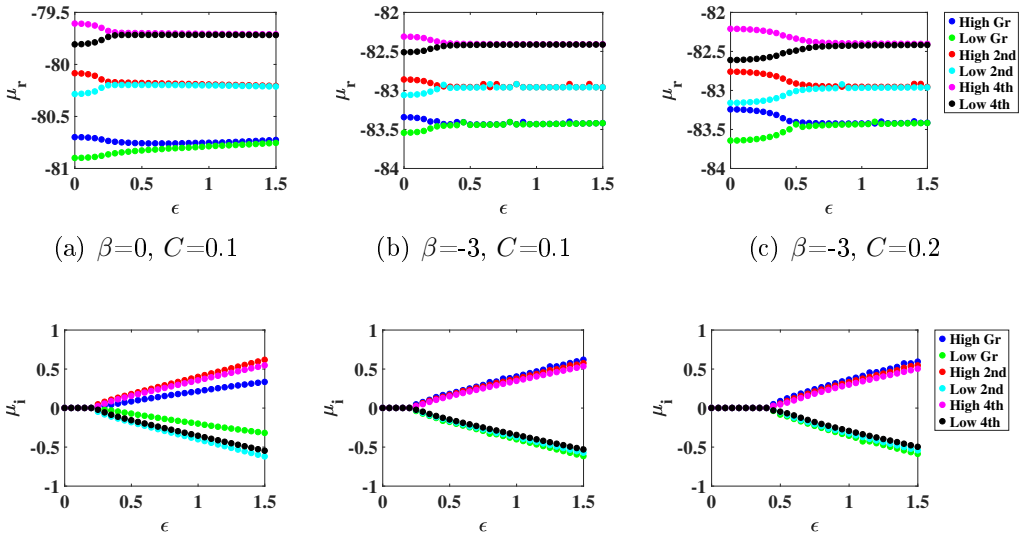

(a) β=0, C=0.1 (b) β=-3, C=0.1 (c) β=-3, C=0.2

(d) β=0, C=0.1 (e) β=-3, C=0.1 (f) β=-3, C=0.2

Figure 5.1: The real and imaginary eigenvalues (μ_r and μ_i) with the coefficient of imaginary potential (ϵ) for the high and low-frequency modes in the linear and nonlinear regimes for Scarf II potential at $v = -1$, $d = 0.1$.

form,

$$\psi(x,z) = U(x)\ \exp\ [i(\mu z + \theta_1)]$$
$$\phi(x,z) = U(x)\ \exp\ [i(\mu z + \theta_2)] \tag{5.4}$$

where $U(x)$ gives the stationary solution and μ is the propagation constant. The eigenvalue equation satisfied by the stationary solution is of the form

$$\mu U = \frac{d}{2}\ U_{xx} + \beta\ |U|^2\ U + V_r\ U + C\ \cos\delta\ U, \tag{5.5}$$

where $\delta = \theta_1 - \theta_2$ and $\cos\delta = \frac{\sqrt{C^2 - V_i^2}}{C}$. High-frequency mode ($U_H$) exists when $\cos\delta > 0$ and $\cos\delta < 0$ refers to the low-frequency mode (U_L). In the linear regime, the eigenvalue equation is given by

$$\mu U = \frac{d}{2}\ U_{xx} + V_r\ U + C\ \cos\delta\ U. \tag{5.6}$$

The eigenvalue equations in the nonlinear and linear regimes are solved using the finite difference method and the eigenvalues and corresponding eigenfunctions are found.

The values of μ_r and μ_i in the linear and nonlinear systems have been studied which are depicted in Fig. 5.1. The top panel of the figure shows μ_r values with gain/loss coefficient, ϵ, for high and low-frequency modes of the eigenstates. The blue and green coloured dots, respectively, indicate the real eigenvalues of the high and low-frequency modes of the ground state. Similarly, the red and cyan coloured dots, respectively, refer to the real eigenvalues of the high and low-frequency modes of the second excited state. And, magenta and black dotted plots show the high and low-frequency modes of the fourth excited state. Fig. 5.1(a) shows the real eigenvalues of the ground and excited states in the linear regime. μ_r values are distinct for small values of ϵ. For large ϵ, μ_r values of the high and low modes of each state will merge. Fig. 5.1(b) and (c) show the real eigenvalues in the nonlinear regime. The results are similar to the linear case. For each mode, μ_r is smaller in the defocusing nonlinear medium when compared to the linear regime.

In the linear and nonlinear cases, the variations in the imaginary eigenvalues with ϵ are as shown in the bottom panel of Fig. 5.1. In the figures, the blue, red and magenta colours indicate the imaginary eigenvalues of the high-frequency modes of the fundamental, 2nd and 4th eigenstates, respectively. Similarly, the green, cyan and black coloured dots refer to the low-frequency modes of the ground, 2nd and 4th excited states, respectively. In both cases, $\mu_i = 0$ until the threshold value for all the eigenstates and this region is known as the PT-symmetric regime. Above the threshold value, the eigenvalues are complex and the region is called as the broken PT regime. The threshold value of the gain/loss coefficient at which this phase transition occurs is called ϵ threshold, ϵ_{th}. Fig. 5.1(d)-(f) show that $\epsilon_{th} = 2C$ for the ground and excited states in the linear and nonlinear regimes. From the figures, it is clear that as the coupling constant (C) increases, ϵ_{th} also increases, i.e. the coupling enhances the PT-symmetry.

5.2.1 Formation of dark soliton-like solutions

The eigenstates in the linear and defocusing nonlinear regimes are plotted in Fig. 5.2 and Fig. 5.3, respectively. In the figures, blue and green plots show the high and low-frequency modes of the ground state. The high and low modes of the second

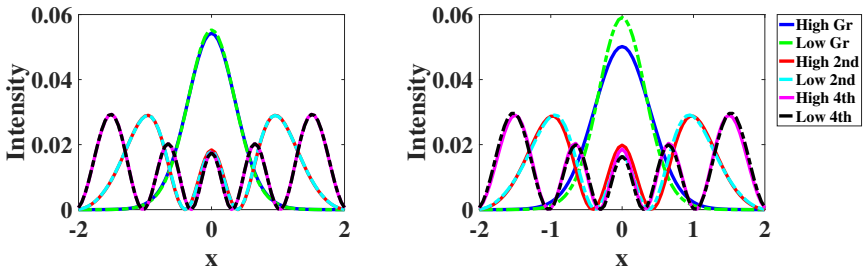

(a) $\epsilon = 0.1$ (b) $\epsilon = 0.25$

Figure 5.2: The eigenfunctions of low and high-frequency modes of the ground state in the PT ($\epsilon = 0.1$) and broken PT ($\epsilon = 0.25$) regimes at $k = 1$, $v = -1$, $C = 0.1$, and $d = 0.1$, for linear case.

excited state are represented by red and cyan coloured plots. Also, the magenta and black plots refer to the high and low modes of the fourth excited state. Fig. 5.2(a) and (b) show the eigenmodes of the ground, 2nd and 4th excited states in the linear regime. The eigenmodes are symmetric with intensity bubbles at the centre of x-coordinate ($x = 0$). The low and high-frequency eigenmodes of each state are the same in the PT regime, as depicted in Fig. 5.2(a). The high and low-frequency modes of each state split apart above the threshold value, ϵ_{th}, which is shown in Fig. 5.2(b). The refractive index profile compensates with the gain/loss distribution which leads to symmetric solutions with bubbles at the centre.

The effect of self-defocusing nonlinearity on the eigenstates are analysed. For the ground and even excited states the eigenfunctions are symmetric, whereas for the odd excited states the eigenfunctions are anti-symmetric. The eigenfunctions of the ground and first excited states in Scarf II potential are as shown in Fig. 5.3(a). For symmetric eigenstates, the self-defocusing nonlinearity admits intensity dips at $x = 0$. For antisymmetric odd eigenstates, the intensity is zero at $x = 0$. The intensity plots of the ground and even excited states in PT system with defocusing nonlinearity are illustrated in Fig. 5.3(b)-(e). The intensity plots show central dips in the presence of self-defocusing nonlinearity, whereas that show central peaks in the linear system. Fig. 5.3(b) shows that when β is small ($\beta = -1$), only the ground state has the central dip, whereas a dip starts to evolve for the 2nd excited state and no dip is formed for the 4th excited state. When β is increased ($\beta = -3$), a central dip is formed for the 4th excited state also, which is shown in Fig. 5.3(d). The

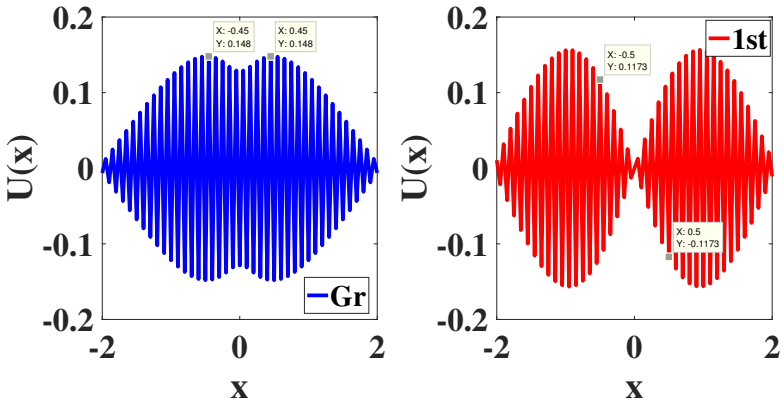

(a) Eigenfunctions of ground and 1st excited state

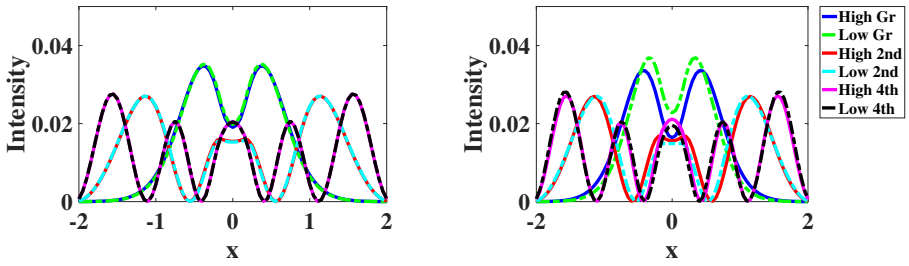

(b) ϵ=0.1,β=-1 (c) $\epsilon = 0.25, \beta = -1$

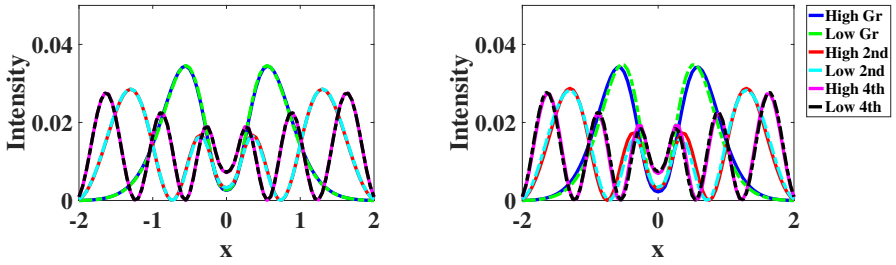

(d) $\epsilon = 0.1, \beta = -3$ (e) $\epsilon = 0.25, \beta = -3$

Figure 5.3: The eigenfunctions of low and high-frequency modes of the ground and excited states in the PT and broken PT-symmetric regimes in the nonlinear system for Scarf II potential at $v = -1$, $C = 0.1$, and $d = 0.1$.

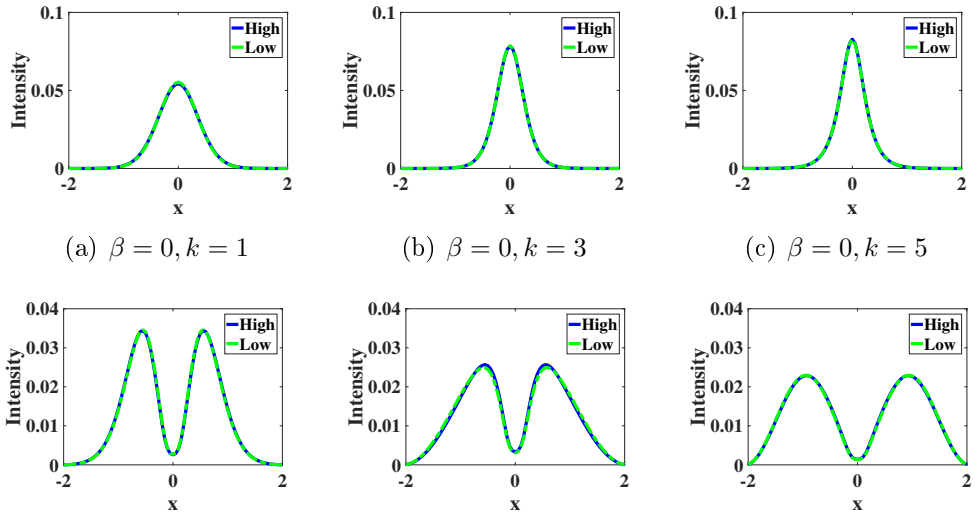

(a) $\beta = 0, k = 1$ (b) $\beta = 0, k = 3$ (c) $\beta = 0, k = 5$

(d) $\beta = -3, k = 1$ (e) $\beta = -3, k = 3$ (f) $\beta = -3, k = 5$

Figure 5.4: The eigenfunctions of low and high-frequency modes of the ground state in the PT-regime ($\epsilon = 0.1$) at $k = 1, 3, 5$, $v = -1$, $C = 0.1$, and $d = 0.1$, for linear and nonlinear cases.

depth of the central dips of the eigenstates is more for higher values of the defocusing nonlinearity. From Fig. 5.3(b) and (d), it is visible that the eigenfunctions of the high and low-frequency modes of each state merge in the PT regime ($\epsilon = 0.1$). Whereas in the broken PT regime ($\epsilon = 0.25$), the high and low-frequency modes of each state split apart as shown in Fig. 5.3(c) and (e). The interaction between the self-defocusing nonlinearity and refractive index distribution with appropriate gain/loss modulation leads to self-trapped dark soliton-like solutions with central dips.

In the linear system, the fundamental modes are studied in the PT-symmetric regime by varying the width (k) of the potential, which are illustrated in Fig. 5.4(a)-(c). The intensity of the central peak of the ground state increases with increasing k. In the nonlinear system, for the central dips of the fundamental and higher eigenmodes, an optimum depth is formed at $\beta = -3$. So the fundamental mode is studied at $\beta = -3$ in the PT-symmetric regime by varying the width (k) of the potential, which is illustrated in Fig. 5.4(d)-(f). From the figures it is clear that as k increases the depth of the dip is reduced.

The ground and excited eigenmodes of linear system have central peak whereas central dip is formed in the self-defocusing nonlinear medium. The nonlinearity co-

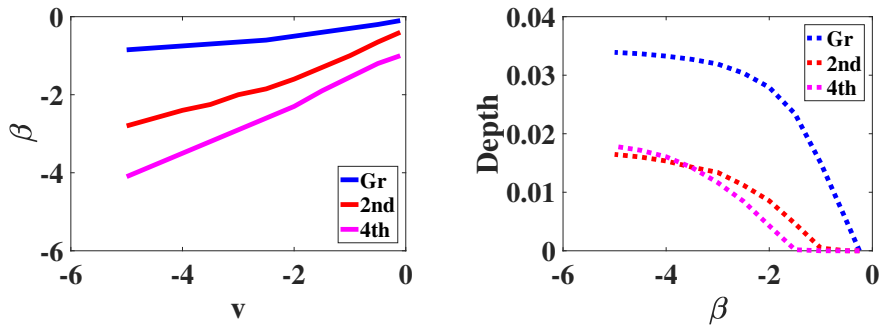

(a) β Vs v (b) Maximum depth Vs β at $v = -1$

Figure 5.5: The dip formation in the nonlinear regime for ground and excited states at $\epsilon = 0.1$, $C = 0.1$, and $k = 1$. (a) β values at which the dip evolves for different v values and (b) the depth of the central dip with defocusing nonlinearity.

efficient at which the central dip evolves depends on the coefficient of real potential, v. This variation for ground, 2nd and 4th excited states in the PT-symmetric regime for $k = 1$ (Scarf II) are plotted in Fig. 5.5(a). As $|v|$ increases, the value of $|\beta|$ at which the central dip evolves also increases. Also, the maximum depth of the central dip is plotted with the nonlinearity coefficient in Fig. 5.5(b). From the figure, it is evident that as $|\beta|$ increases the depth of the central dips of the ground and excited states also increase and become almost steady at a higher value of $|\beta|$. The interplay of the defocusing nonlinearity and real potential well generate eigenmodes with localised dips.

5.2.2 The stability of the eigenstates

The stability of the stationary states of the coupled system with k-wavenumber Scarf II potential and self-defocusing nonlinearity has been studied using linear stability analysis. The perturbation eigenvalue spectra of the ground and excited states are studied in the linear and nonlinear regimes with Scarf II potential, which are as shown in Fig. 5.6. Fig. 5.6(a) and (b) show the perturbation eigenvalues in the linear regime. Fig. 5.6(a) depicts that the λ values of the high (blue) and low (green) frequency modes of the ground state have no imaginary component in the PT-symmetric phase ($\epsilon = 0.1$), which indicates the solutions are stable in this phase. Similarly, high and low-frequency modes (red and cyan) of the 2nd

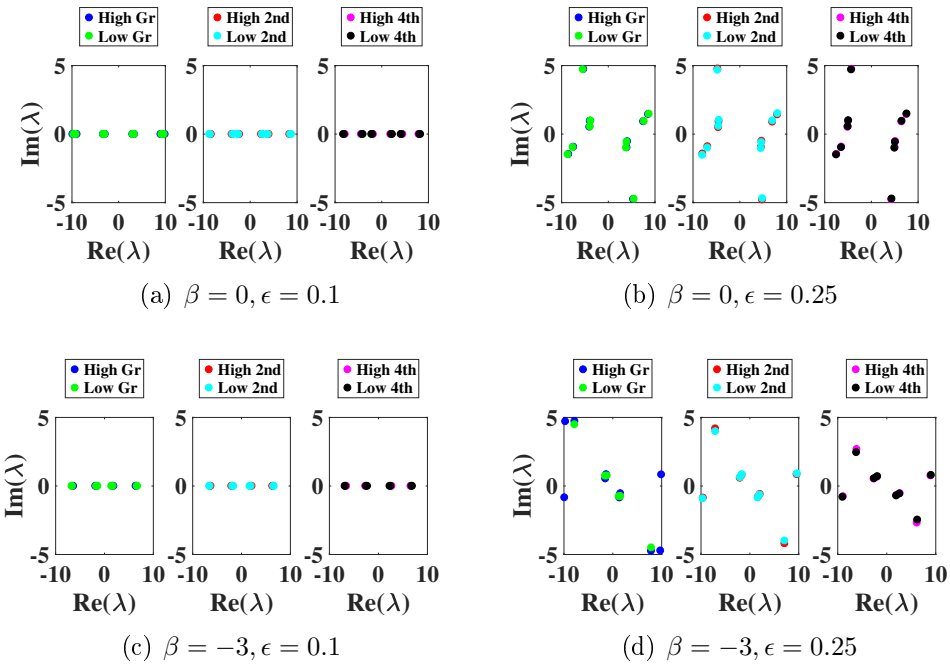

Figure 5.6: The linear stability analysis of the ground and excited states in the linear and nonlinear regimes for Scarf II potential at $v = -1$ and $C = 0.1$.

excited state have only real λ values in the PT regime. Also, high (magenta) and low (black) frequency eigenmodes of the fourth excited state have real λ values at $\epsilon = 0.1$. It means that the solutions of the excited states are also linearly stable in the PT-symmetric regime. The perturbation eigenspectra of the ground, 2nd and 4th excited states in the broken PT regime ($\epsilon = 0.25$) have been shown in Fig. 5.6(b). The imaginary component of the λ value denotes that the solutions are unstable in the broken PT-symmetric regime in the linear system. The nature of the stability in the self-defocusing nonlinearity resembles the linear system and is shown in Fig. 5.6(c) and (d). i.e., for nonlinear case, the ground and excited modes are stable in the PT phase and are unstable in the broken PT phase.

The propagation of the stationary eigenstates of the ground state in the linear and nonlinear regimes are studied using Equation (5.4). Fig. 5.7 shows the nature of the low and high-frequency modes of the ground state with Scarf II potential in the PT and broken PT phases. Linear system shows stable beam propagation in the PT phase ($\epsilon = 0.1$), which is shown in Fig. 5.7(a) and (b). Whereas in the broken PT phase ($\epsilon = 0.25$), the intensity of the central peak of the high-frequency mode

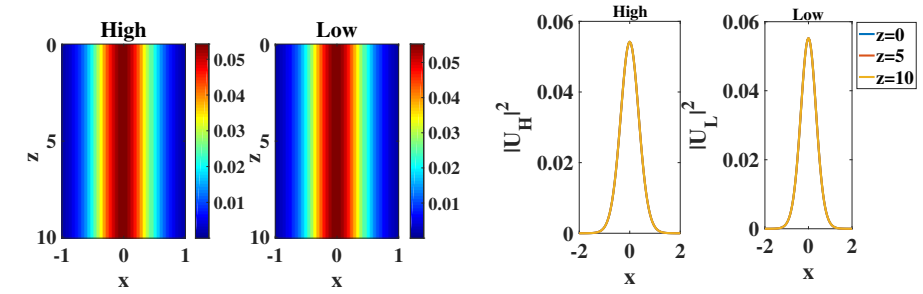

(a) $\epsilon = 0.1$ (b) $\epsilon = 0.1$

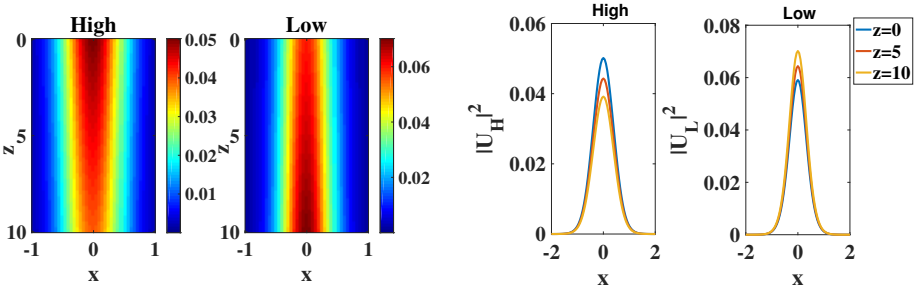

(c) $\epsilon = 0.25$ (d) $\epsilon = 0.25$

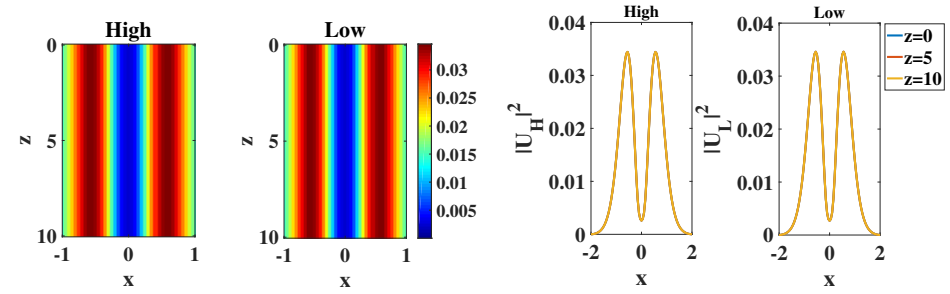

(e) $\epsilon = 0.1$ (f) $\epsilon = 0.1$

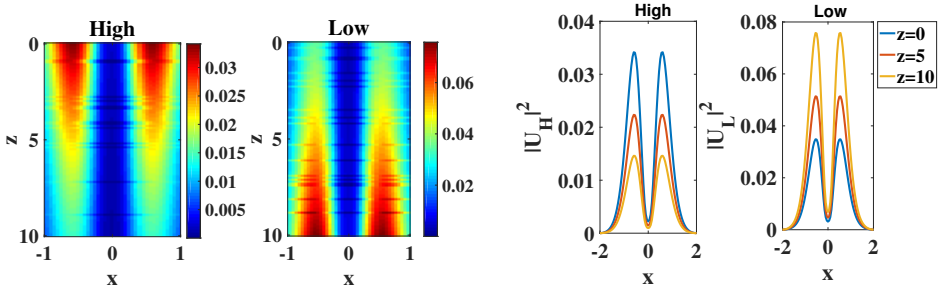

(g) $\epsilon = 0.25$ (h) $\epsilon = 0.25$

Figure 5.7: The propagation of the high and low-frequency modes of the ground state before and after the PT phase transition at $k = 1$, $C = 0.1$, and $v = -1$. Row 1 and Row 2: in the linear regime. Row 3 and Row 4: in the nonlinear regime ($\beta = -3$).

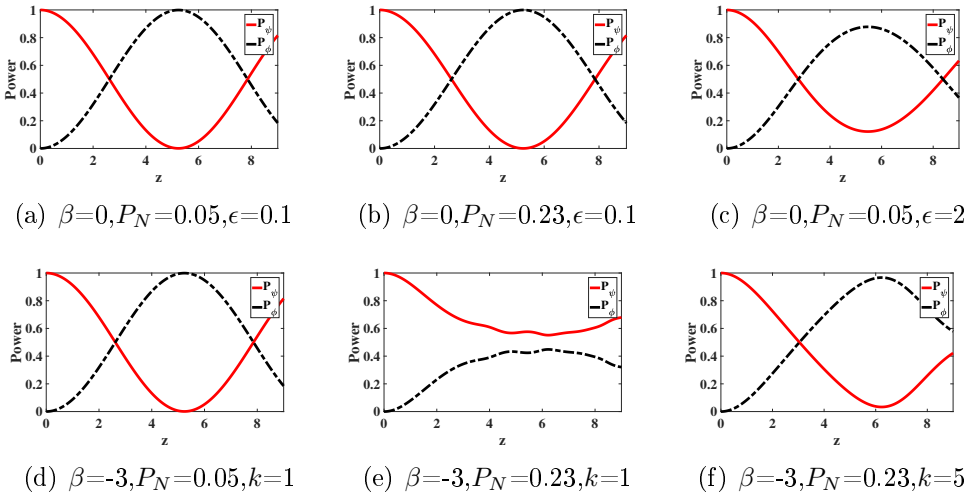

(a) β=0,P_N=0.05,ϵ=0.1 (b) β=0,P_N=0.23,ϵ=0.1 (c) β=0,P_N=0.05,ϵ=2

(d) β=-3,P_N=0.05,k=1 (e) β=-3,P_N=0.23,k=1 (f) β=-3,P_N=0.23,k=5

Figure 5.8: The relative power distribution in gain (P_ψ) and lossy (P_ϕ) channels in the PT-symmetric potential for $v = -1$ and $C = 1$ for linear and nonlinear cases. Top panel: linear case at $k = 1$ and bottom panel: nonlinear case at $\beta = -3$ and $\epsilon = 0.1$.

decreases and that of the low-frequency mode increases as shown in Fig. 5.7(c) and (d). It implies the instability of the eigenmode in the broken PT regime. In the defocusing nonlinear medium, the solution shows stable propagation in z in the PT regime which is clearly depicted in Fig. 5.7(e) and (f). But, once the PT symmetry gets broken, the depth of the central dip of the high-frequency mode decreases and that of the low-frequency mode increases as depicted in Fig. 5.7(g) and (h). It verifies that in the nonlinear regime, the ground state solutions are unstable in the broken PT phase.

5.3 The switching dynamics

The switching dynamics of the fundamental state in two channels of the self-defocusing nonlinear coupled system with PT-symmetric k-wavenumber Scarf II potential have been analysed by solving the model given in Equation (5.1), using FDBPM. The power transfer between the gain and lossy channels is analysed for different parametric values in the linear and nonlinear cases.

The power variation in the two channels during the propagation is as shown in Fig. 5.8, for linear and nonlinear systems. In the figure, the relative power in the

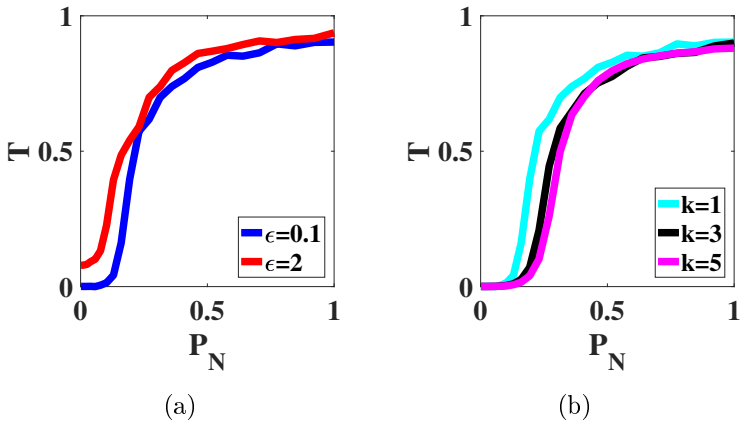

Figure 5.9: The switching curve of the ground state in the nonlinear system ($\beta = -3$) at $v = -1$ and $C = 1$. (a) T vs P_N, for $\epsilon = 0.1, 2$ and (b) T vs P_N for $k = 1, 3, 5$.

gain and lossy channels are represented by red and black plots, respectively. The shortest distance at which maximum power in the gain channel is transferred to the lossy channel for the first time is called the first coupling length, ζ. Its value depends on the strength of the coupling.

The power distribution and effect of the gain/loss coefficient on the power transfer are studied in the linear system and are illustrated in Fig. 5.8(a)-(c). Fig. 5.8(a) shows that, at a low input, the power in the gain channel completely switches to the lossy channel when ϵ is small. In the linear medium, the power transfer is independent of the input power which is shown in Fig. 5.8(b). However, a high value of ϵ hinders the switching to the lossy channel as shown in Fig. 5.8(c).

Fig. 5.8(d)-(f) show the power transfer between the channels in the nonlinear regime. From Fig. 5.8(d) it is evident that at low input power, the system resembles the linear system. The defocusing nonlinearity takes the role at a high input power as shown in Fig. 5.8(e). The power is not completely transferred to the loss channel in this case even for small ϵ. However, the power transfer occurs between the gain and lossy channels due to the interplay between k-wavenumber Scarf II potential and the defocusing nonlinearity at $k = 5$ as depicted in Fig. 5.8(f).

The power remaining in the gain channel at ζ w.r.t the input power launched in the same channel is defined as the transmission coefficient, i.e., $T = \frac{P(z=\zeta)}{P(z=0)}$. The power switching curve is plotted by taking the normalized input power (P_N) along

the x axis and the transmission coefficient along the y axis. The normalized input power, P_N, is defined as the ratio of the input power to the maximum input power and $P_N \leq 1$. The critical switching power, P_r, is input power corresponding to $T = 0.5$. The power transmission of the defocusing nonlinear system has been analyzed at $\beta = -3$ by varying the input power and is illustrated in Fig. 5.9. In Fig. 5.9(a) the effect of the gain/loss coefficient on the power transmission has been depicted. The critical switching power is lower when ϵ is high. The variation in the power-dependent transmission with the width of the potential is analysed, which is plotted in Fig. 5.9(b). For $k = 1$ (cyan), $k = 3$ (black), and $k = 5$ (magenta) the critical switching powers are studied. As the width of the potential increases, the critical switching power decreases.

5.4 Conclusion

The stationary solutions and switching dynamics of the PT-symmetric coupled systems with k-wavenumber Scarf II potential in linear and self-defocusing nonlinear media have been analysed. The eigenvalues are real in the PT-symmetric phase and are complex in the broken PT phase. The phase transition from the PT-symmetry to the broken PT-symmetry occurs at a threshold value of the gain/loss coefficient, for linear and nonlinear cases. The coupling enhances the PT-symmetry. In linear system, the ground and excited modes show intensity bubbles at the centre of the transverse coordinate. In contrast, the eigenmodes of the ground and excited states show central intensity dips in the defocusing nonlinear medium. In the PT regime, the high and low-frequency modes of each state are the same for linear and nonlinear cases. For nonlinear modes, the central dip evolution and its depth depend on the strength of the defocusing nonlinearity, the depth of the real potential well, and the width of the real and imaginary potentials. The high and low-frequency modes, of the ground and excited states, are linearly stable in the PT-symmetric regime and show instability in the broken PT regime, for both linear and nonlinear systems. The PT-symmetric systems with self-defocusing nonlinearity generate stable localised solutions of the dark soliton form. In the linear system, the power

transfer occurs between the channels and is independent of the input power, whereas the system with high gain/loss effects inhibits the power transfer. In the nonlinear system, for PT-symmetric Scarf II potential, the power transfer occurs at a small input, whereas the power is trapped in the gain channel at a high input power. In the high input, the power transfer between the channels takes place when the width of the k-wavenumber Scarf II potential is small. The input power-dependent beam propagation has been studied by varying the gain/loss coefficient and the width of the potential. The critical input power is decreased by increasing the gain/loss effects and the width of the k-wavenumber Scarf II potentials. In self-defocusing nonlinear regime, the teamplay between the nonlinear effects and the real and imaginary potentials influence the power transmission, which find applications in optical switching devices.

Chapter 6

Nonlinear modes in a system with k-wavenumber Scarf II barrier potential

6.1 Introduction

The real component of the PT-symmetric potential can be either well or barrier distributions depending on the sign of the coefficient of real potential. In optical system, the real part of the k-wavenumber Scarf II barrier potential refers to the inhomogeneous refractive index profile for which maximum value is at the center and it taper off symmetrically towards either extreme. Light controlled by light is the most fundamental concept of all-optical communication and all-optical switches. Recent developments in photonics changed electronically controlled optical switches to light-controlled optical switches. The joint action of Kerr nonlinearities, beam diffraction and k-wavenumber Scarf II barrier potential in the symmetry-preserving phase and symmetry broken phase showcase rich physics and phenomena such as all-optical switching and unidirectional light transport etc. In this chapter, we analyse the fundamental and higher eigenmodes of PT-symmetric single and coupled systems with k-wavenumber Scarf II barrier potential, for weak and strong self-defocusing nonlinearities. The effect of barrier potential in the formation of eigenmodes with

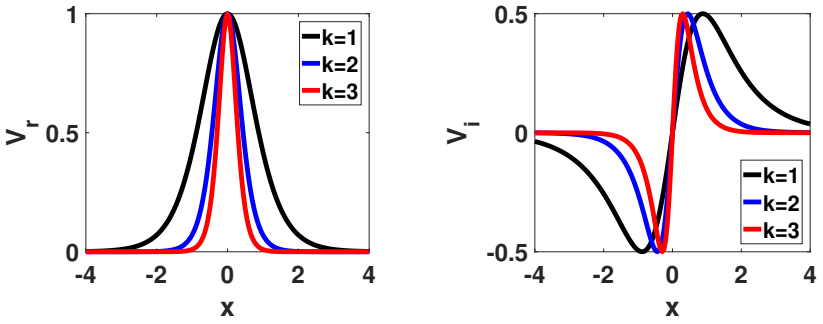

(a) Real part (b) Imaginary part

Figure 6.1: The real and imaginary components of the k-wavenumber Scarf II barrier potential at $v = 1$ and $\epsilon = 1$ for $k = 1, 2$ and 3

central dips in the self-defocusing nonlinear medium is analysed. The switching dynamics of the coupled system also studied in the PT and broken PT phases. The real and imaginary components of the potential take the form,

$$V_r(x) = v \text{ sech}^2(kx)$$

and

$$V_i(x) = \epsilon \text{ sech}(kx) \tanh(kx),$$

where $v > 0$ for barrier potential and k modulates the width of the potential. Figs. 6.1(a) and (b) show the profiles of V_r and V_i.

The model of the single system is introduced in Section 6.2. The stationary states and propagation for weak and strong nonlinearities are discussed under this section. The coupled model, stationary states and switching dynamics are studied under Section 6.3. Section 6.4 concludes the chapter.

6.2 Single system

The evolution of an optical beam in a nonlinear single system with k-wavenumber Scarf II barrier potential is given by

$$i\psi_z + \frac{d}{2}\psi_{xx} + \beta|\psi|^2\psi + [V_r(x) + iV_i(x)]\psi = 0 \tag{6.1}$$

v	$\epsilon_{th}(k=1)$	$\epsilon_{th}(k=\sqrt{2})$
0.5	0.75	0.95
1	1.2	1.4
1.5	1.7	1.85
2	2.2	2.35
2.5	2.7	2.85
3	3.2	3.35

Table 6.1: The threshold values of the coefficient of the imaginary part of the PT-symmetric k-wavenumber Scarf II potential for $k = 1, \sqrt{2}$ in linear regime in single system.

where $\psi(x, z)$ is the beam amplitude and $\beta < 0$ refers to the self-defocusing nonlinearity.

The propagation-invariant solution of Equation (6.1) satisfies the eigenvalue equation of the form

$$\mu U = -\frac{d}{2}\frac{d^2U}{dx^2} - \beta|U|^2U - [V_r(x) + i\ V_i(x)]U. \tag{6.2}$$

The linear and nonlinear eigenvalue equations are solved numerically using the finite difference method and the eigenvalues and eigenmodes are analysed.

6.2.1 Linear system

The eigenvalue spectra and the eigenmodes of ground and excited states are studied in the linear regime for k-wavenumber Scarf II barrier potential and are as shown in Fig. 6.2. The eigenvalues of the ground (blue), 2nd (red) and 4th (black) excited states by varying the coefficient of imaginary potential, ϵ, are plotted in Fig. 6.2(a). The region with $\mu_i = 0$ is the PT-symmetric regime and the region with $\mu_i \neq 0$ is the broken PT regime. For the ground state, the threshold values, ϵ_{th}, at which the PT-symmetry breaking occurs for different v values are tabulated in Table 6.1 for $k = 1, \sqrt{2}$. For nonlinear case, the eigenvalues are real for $|\epsilon| \leq v + k^2/4$ when $v > 0$.

The eigenmodes of the ground state for Scarf II barrier potentials are plotted for $v = 1, 2, 3$ in Fig. 6.2(b)-(d). Eigenmodes with intensity peaks at the centre are formed. The intensity of the solution is increased with the coefficient of real potential. The 2nd (red) and 4th (black) excited states in the linear regime with

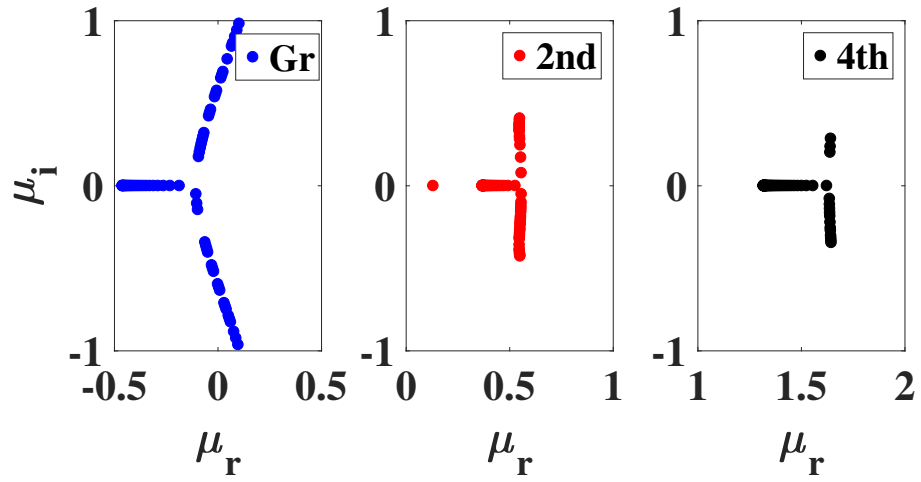

(a) $v = 1$

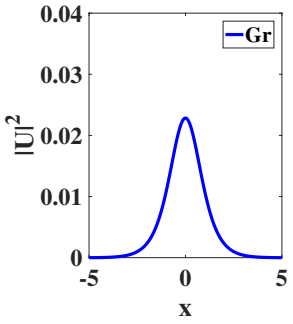

(b) Gr, $v = 1$

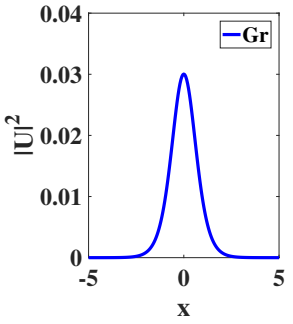

(c) Gr, $v = 2$

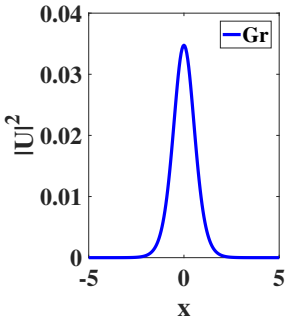

(d) Gr, $v = 3$

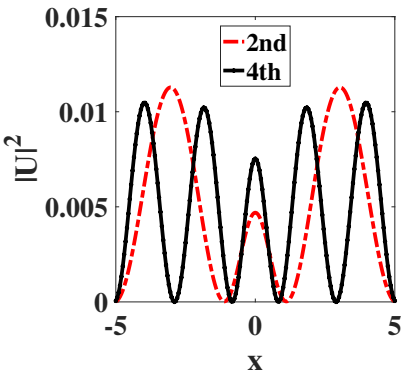

(e) Excited, $v = 1$

Figure 6.2: The eigenvalue spectra and the stationary states for barrier Scarf II potential in the linear regime for $d = 0.05$ in single system. Top panel: Eigenvalues in complex plane for ground, 2nd and 4th excited states by varying ϵ in the range [0 4]. Middle panel: ground state eigenmode at $\epsilon = 0.1$. Bottom panel: 2nd and 4th excited states in barrier potential.

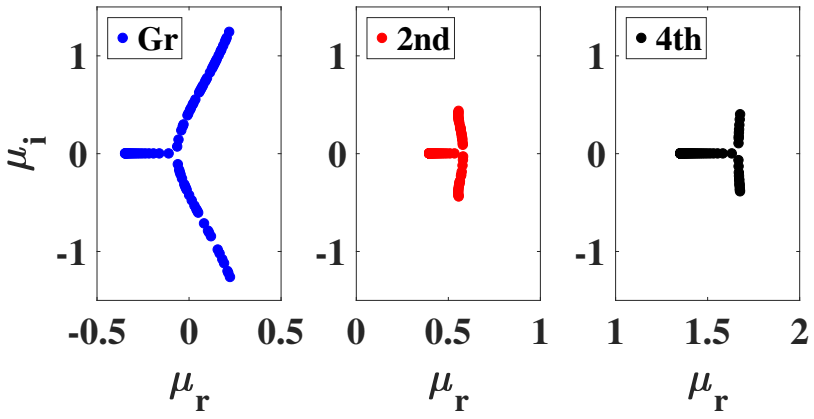

(a) $\beta = -1$

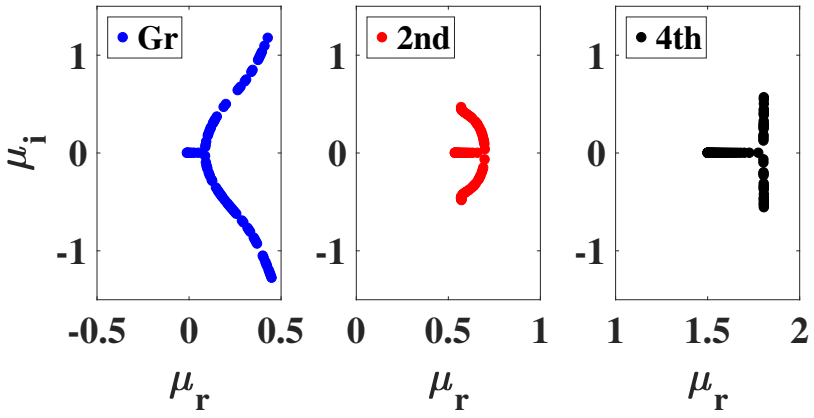

(b) $\beta = -5$

Figure 6.3: The eigenvalue spectra in the self-defocusing nonlinear regime for barrier Scarf II potential at $d = 0.05$, $v = 1$ and $\beta = -1, -5$ for single system.

Scarf II barrier potential are plotted in Fig. 6.2(e). It shows that the solutions have central intensity peaks. For linear systems, intensity peaks are formed in the Scarf II barrier potential due to the interplay between diffraction and PT-symmetry. Whereas intensity dips are formed in the Scarf II well potential [98].

6.2.2 Nonlinear system

The nonlinear eigenvalue equation, given in Equation (6.2), has been solved for the self-defocusing nonlinearity and the eigenmodes of the ground and even excited states are analysed. The eigenvalues and eigenfunctions with Scarf II barrier potential for different β values are illustrated in Fig. 6.3. In Figs. 6.3(a) and (b), the

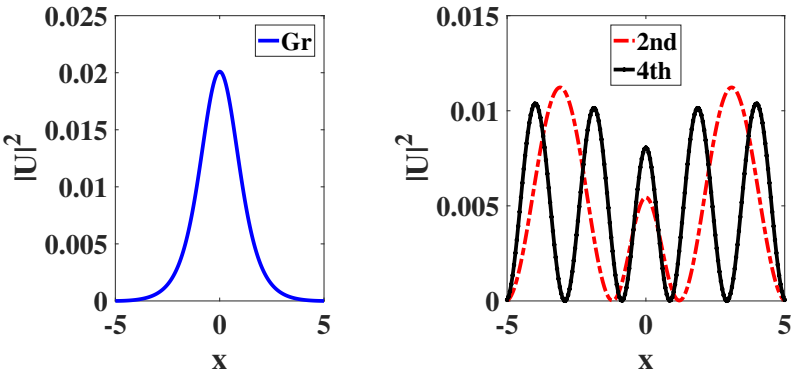

(a) Gr, $\beta = -1$

(b) Excited, $\beta = -1$

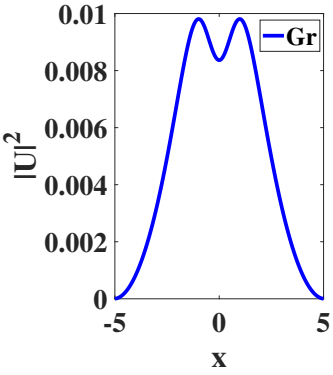

(c) Gr, $\beta = -5$

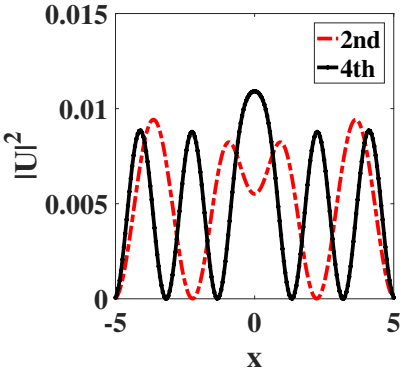

(d) Excited, $\beta = -10$

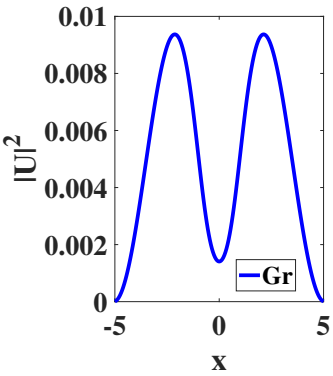

(e) Gr, $\beta = -10$

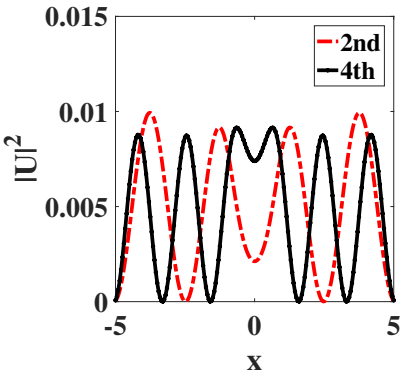

(f) $\beta = -15$

Figure 6.4: The ground and excited stationary states in the self-defocusing nonlinear regime for barrier Scarf II potential in PT regime ($\epsilon = 0.1$) at $d = 0.05$ and $v = 1$.

eigenvalues for the range of gain/loss coefficient, $\epsilon = [0\ 4]$, are plotted at $\beta = -1, -5$. The real spectra for low ϵ imply the unbroken PT regime and the region of complex eigenvalues with higher values of ϵ refers to the broken PT regime. This phase transition occurs at ϵ_{th}.

The fundamental eigenmodes for different β values are shown in Figs. 6.4(a),(c) and (e) in the PT regime at $v = 1$. If the coefficient of nonlinearity is small, the eigenmode has an intensity peak at the centre. Intensity dips are formed at the centre for higher values of the nonlinearity. The depth of the dip increases with an increase in the coefficient defocusing nonlinearity. For weak nonlinearity, the eigenmodes with central peaks exist for excited states also, which is shown in Fig. 6.3(b). From Figs. 6.3(d) and (f), it is clear that a further increase of β forms excited eigenmodes with central dips. In the case of the excited modes, higher nonlinearity strength is needed for the dip formation. The delicate balancing between diffraction, defocusing nonlinearity and Scarf II barrier potential leads to the formation of the eigenmodes with central intensity dips in the PT-symmetric regime.

The effect of the width of the potential, k, on the stationary ground state has been studied for high and low values of the nonlinearity coefficient. For small β, the width of the solution is slightly reduced with k which is depicted in the top panel of Fig. 6.5. From the bottom panel of Fig. 6.5, it is evident that for high β, the depth of the dip is greater when k is large.

The stability of the fundamental state with Scarf II potential has been analyzed using linear stability analysis, in linear and defocusing nonlinear systems. In Fig. 6.6 green and brown dots represent the perturbation eigenvalues in the PT and broken PT regimes, respectively. Figs. 6.6(a) and (b) clearly show that, in the linear regime, the solutions are linearly stable in the PT regime and are unstable in the broken PT regime. Similar results have been found in the defocusing nonlinear regime and are depicted in Figs. 6.6(c) and (d).

6.2.3 Propagation dynamics

The propagation of the eigenmodes of the ground state in the self-defocusing nonlinear system with Scarf II barrier potential is studied in the PT and PT broken

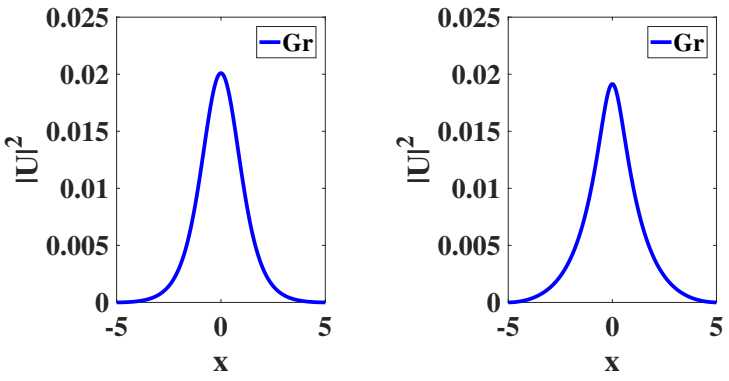

(a) $k = 1, \beta = -1$ (b) $k = 2, \beta = -1$

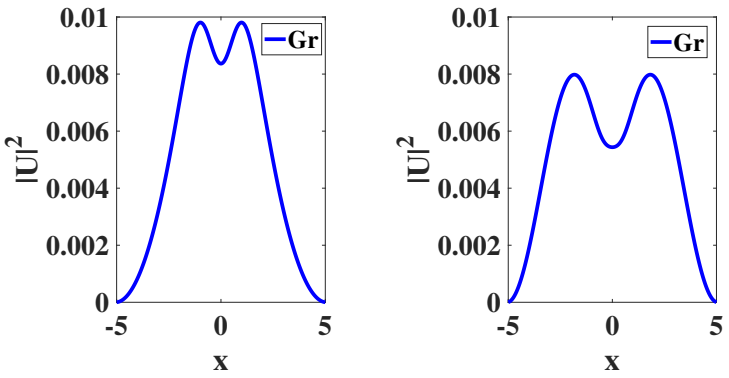

(c) $k = 1, \beta = -5$ (d) $k = 2, \beta = -5$

Figure 6.5: The effect of k on the amplitude of the central peaks and dips of fundamental state in the nonlinear regime at $\epsilon = 0.1$

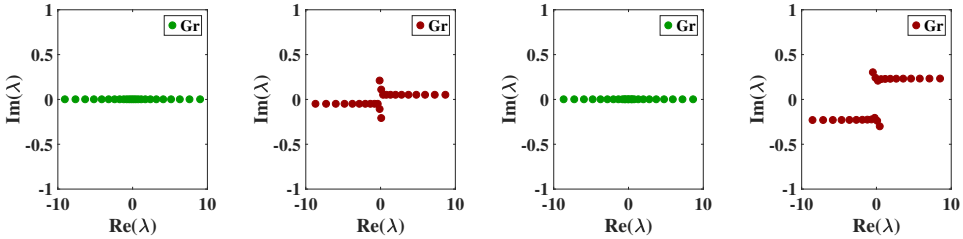

(a) $\beta = 0, \epsilon = 0.1$ (b) $\beta = 0, \epsilon = 1.2$ (c) β=-5,ϵ=0.1 (d) β=-5,ϵ=1.2

Figure 6.6: The perturbation eigenvalues of the stationary states of the ground state in PT-symmetric ($\epsilon = 0.1$) and broken PT ($\epsilon = 1.2$) regimes for linear ($\beta = 0$) and nonlinear ($\beta = -5$) cases at $d = 0.05, v = 1$.

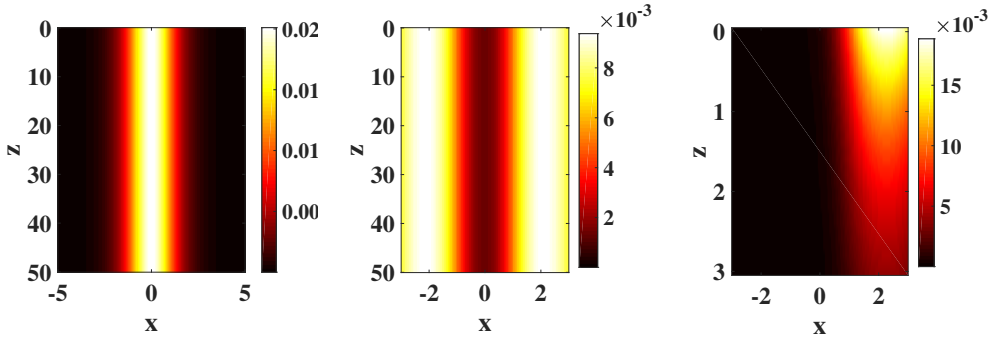

(a) $\beta = -1, \epsilon = 0.1$ (b) $\beta = -10, \epsilon = 0.1$ (c) $\beta = -10, \epsilon = 1.2$

Figure 6.7: The beam propagation at $\beta = -1, -10$ for Scarf II barrier potential at $v = 1$. (a) and (b) in the PT regime ($\epsilon = 0.1$) and (c) in the broken PT regime ($\epsilon = 1.2$)

regimes. Fig. 6.7(a) and (b) verify the stable beam propagation in the PT regime. Whereas it is clear from Fig. 6.7(c) that the fundamental mode is unstable in the broken PT phase ($\epsilon = 1.2$).

6.3 Coupled system

The beam evolution in a nonlinear coupled system with PT-symmetric transverse potential is given as

$$\begin{aligned} i\psi_z + \tfrac{d}{2}\psi_{xx} + \beta|\psi|^2\psi + [V_r(x) + iV_i(x)]\psi + C\phi = 0 \\ i\phi_z + \tfrac{d}{2}\phi_{xx} + \beta|\phi|^2\phi + [V_r(x) - iV_i(x)]\phi + C\psi = 0, \end{aligned} \tag{6.3}$$

where ψ and ϕ are the beam amplitudes in the gain and lossy channels propagating along z direction.

6.3.1 The stationary states

The nonlinear eigenvalue equation,

$$\mu U = -\frac{d}{2}\, U_{xx} - \beta\, |U|^2\, U - V_r\, U - C\, cos\delta\, U, \tag{6.4}$$

with $cos\delta > 0$ has been solved and the stationary states are studied by taking Gaussian form of input in the boundary values $x = -2$ to $x = 2$.

The stationary solutions of the ground and excited states in the self-defocusing nonlinear regime with k-wavenumber Scarf II barrier potential are studied which are as shown in Fig. 6.8. The variation of the imaginary eigenvalues (μ_i) with the gain/loss coefficient (ϵ) for the ground state, at $\beta = -5$ is plotted in Fig. 6.8(a). It is obvious that $\mu_i = 0$ for small ϵ whereas it becomes nonzero above a threshold value of ϵ and $\epsilon_{th} = 1.1$ for the given parameters. The complex eigenvalues of the ground (blue), 2nd (red) and 4th (black) excited states for a range of gain/loss coefficient are plotted (μ_i vs μ_r) in Fig. 6.8(b). The region with purely real eigenvalues is called as the PT-symmetric regime and the region with $\mu_i \neq 0$ is termed as the broken PT-symmetric regime.

The eigenmodes of the ground, 2nd and 4th excited states are plotted in the PT regime, for low and high values of the defocusing nonlinearity. When β is small, the ground state solution has an intensity peak at $x = 0$ which is depicted in Fig. 6.8(c). But, eigenmodes with central dips are formed when β is high which is clearly shown in Figs. 6.8(d) and (e). The figures show that as β increases, the depth of the dip increases. When β is small the effect of the barrier potential dominates and it leads to the bright soliton form of solution. Whereas for strong nonlinearity, the defocusing effect dominates and dark soliton-like solutions are formed. Because of the reason that the stationary solution with a sharp dip is formed around $x = 0$ for $\beta = -5$, this parameter range of the defocusing nonlinearity is used for further analysis. The eigenmodes of the excited states are illustrated in Figs. 6.8(f) and (g). The red coloured plots indicate the 2nd excited state and black refers to the 4th excited state. It has been shown that the eigenmodes with central peaks are formed for weak nonlinearity and that with central dips are formed when β is increased.

Linear stability analysis is used to study the stability of the solutions and the perturbation eigenvalue spectra are analysed for the ground state in Scarf II potential which is shown in Fig. 6.9. The nature of the perturbation eigenvalues in the unbroken and broken PT phases, respectively, are illustrated in Figs. 6.9(a) and (b). From Fig. 6.9(a) it is clear that λ is real in the PT-symmetric regime ($\epsilon = 0.1$).

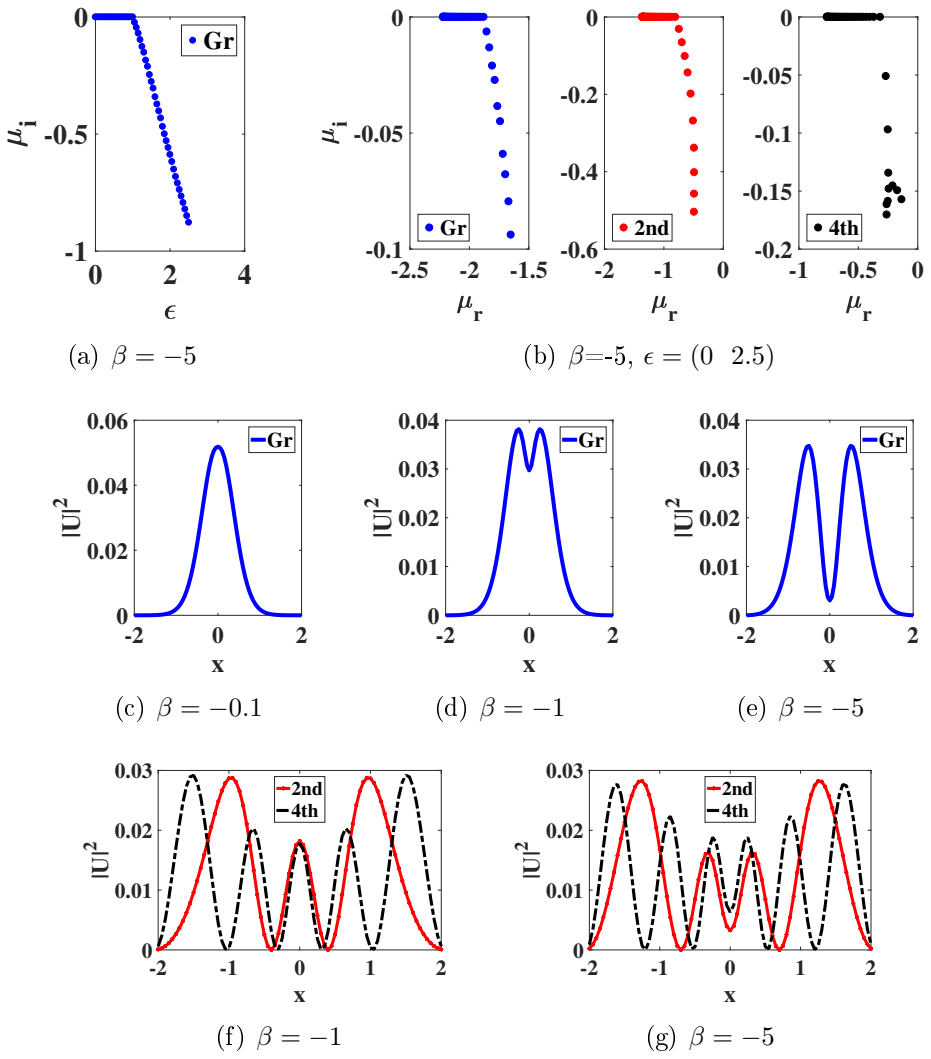

(a) $\beta = -5$ (b) β=-5, $\epsilon = (0 \;\; 2.5)$

(c) $\beta = -0.1$ (d) $\beta = -1$ (e) $\beta = -5$

(f) $\beta = -1$ (g) $\beta = -5$

Figure 6.8: The eigenvalues and eigenfunctions of the ground and excited states in coupled system at $v = 1$, $k = 1$, $C = 0.5$ and $d = 0.1$. Top panel: (a) μ_i vs ϵ for ground state, (b) μ_i vs μ_r for ground, 2nd and 4th excited states by varying ϵ in the range $(0 \;\; 2.5)$. Middle panel: eigenmodes of the ground state for $\epsilon = 0.1$ at (c) $\beta = -0.1$ (d) $\beta = -1$ and (e) $\beta = -5$. Bottom panel: eigenmodes of the 2nd and 4th excited states at $\epsilon = 0.1$ for (f) $\beta = -1$ and (g) $\beta = -5$.

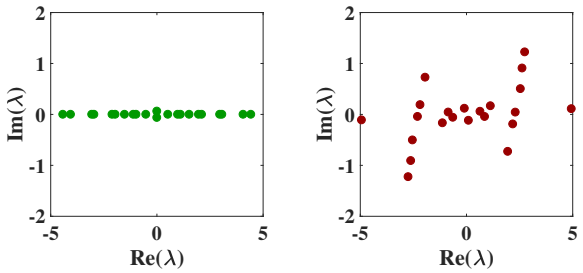

(a) $\epsilon = 0.1$ (b) $\epsilon = 1.2$

Figure 6.9: The perturbation eigenvalues of the ground state coupled system in the PT ($\epsilon = 0.1$) and broken PT ($\epsilon = 1.2$) regimes for defocusing nonlinearity ($\beta = -5$) in Scarf II potential at $v = 1$ and $C = 0.5$.

Purely real λ values show that the solution is linearly stable in this regime. But, the presence of λ_i indicates the instability of the solution. It is verified that the solution is unstable in the broken PT-regime ($\epsilon = 1.2$) which is shown in Fig. 6.9(b).

6.3.2 The switching dynamics

The switching dynamics of the optical beam in a self-defocusing nonlinear coupled system with k-wavenumber Scarf II barrier potential is studied by numerically solving the coupled NLSE in Equation (6.3), using finite difference beam propagation method. The dynamics of the system has been studied by exciting one of the channels with the stationary solution of the ground state at $\beta = -5$. The switching dynamics is analysed by varying the input power in the PT and broken PT regimes.

Generally, in the absence of PT-symmetric potential, the power oscillates between the channels if the input is low and it gets trapped in the excited channel for high input [89]. The power distribution in the channels are analysed by exciting the gain (lossy) channel with a very low input and is plotted in Fig. 6.10. The red and black coloured plots of Figs. 6.10(a)-(e) indicate the power distribution in the gain and lossy channels, respectively, at $P_N = 0.01$, where P_N is the ratio between the input power to the maximum input at which the power is completely trapped in the same channel [92]. In a coupled system with no PT-symmetric potential, when the input is launched in the gain channel, the power injected is completely transferred to the lossy channel at a coupling length $z = \zeta$ as shown in Fig. 6.10(a).

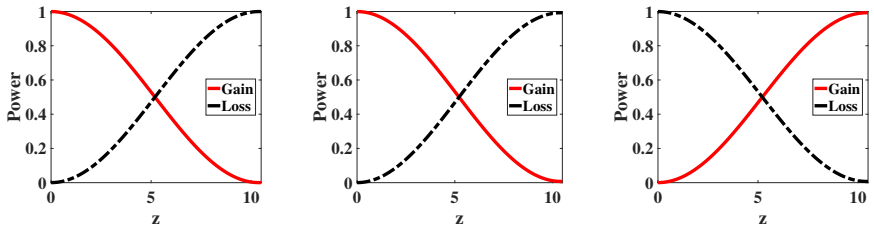

(a) v=0, ϵ=0 (b) v=1, ϵ=0.1 (c) v=1, ϵ=0.1

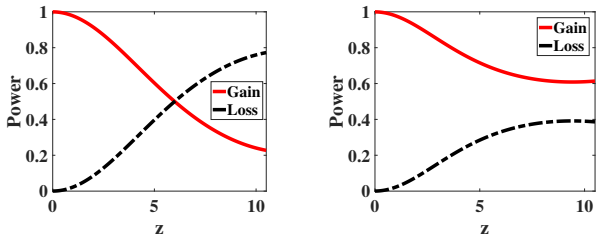

(d) v=1, ϵ=0.5 (e) v=1, ϵ=1.2

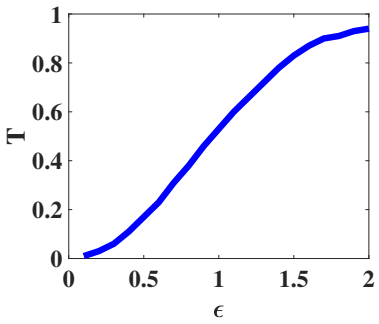

(f) T vs ϵ

Figure 6.10: The power transfer between the gain and lossy channels in the nonlinear regime ($\beta = -5$) for very low input power, $P_N = 0.01$ at $C = 0.5$ and $k = 1$. First row: (a) for $v = 0$ and $\epsilon = 0$, (b) for $v = 1$ and $\epsilon = 0.1$ with gain channel excited and (c) for $v = 1$ and $\epsilon = 0.1$ with loss channel excited. Second row: for (d) $\epsilon = 0.5$ and (e) $\epsilon = 1.2$. Third row: (f) the effect of ϵ on the transmission coefficient (T).

Where, ζ is the shortest distance at which the complete transfer of maximum power occurs from the excited channel to the other for the first time and is called as the first coupling length. Fig. 6.10(b) shows that complete power transfer occurs at ζ from gain to lossy channel when the gain channel is excited with a very low input, in Scarf II potential with small ϵ. Whereas when we excite the lossy channel, the power trasfers to the gain channel in the PT phase ($\epsilon = 0.1$) and is shown in Fig. 6.10(c). The effect of the gain/loss coefficient on the power switching by exciting the gain channel is also analysed. As ϵ is increased, no complete power transfer is observed but more than 50% of the power is transferred in the PT phase which is evident from Fig. 6.10(d). From Fig. 6.10(e), it is obvious that when $\epsilon \geq \epsilon_{th}$, power transferred is negligible and the input power is confined in the excited channel. Fig. 6.10(f) presents the variation of the transmission coefficient (T) with the gain/loss coefficient. T is the fraction of power remaining in the excited channel at the first coupling length w.r.t the input power. This shows that power remained in the excited channel is less than 50% in the PT regime. In contrast, more than 50% of the injected power is confined in the same channel in the broken PT regime. Thus, by varying the gain/loss coefficient, one can achieve the power confinement even at a low input.

The field dynamics through the channels, from $z = 0$ to $z = \zeta$, are analysed in the PT and broken PT phases when the initial input power is very low and are depicted in Fig. 6.11. The blue and red curves of Figs. 6.11(a), (c) and (e) indicate the solutions in the gain channel and lossy channel, respectively. Figs. 6.11(b), (d) and (f) show the intensity plots in the PT and broken PT regimes. Figs. 6.11(a) and (b) show that when the gain channel is excited with the stationary solution, the intensity in the same channel becomes zero at $z = \zeta$. Initially, there was no power in the lossy channel, whereas the power launched in the gain channel switches to the lossy channel at $z = \zeta$ which are clear from the given plots. The beam dynamics in the broken PT regime has been illustrated in Figs. 6.11(c)-(f). When the gain (lossy) channel is excited, the power in the gain (lossy) channel grows up and that in the lossy (gain) channel is almost zero. i.e., gain/loss effects hinder power oscillation in the broken PT phase at a very low input, which have applications in non-reciprocal

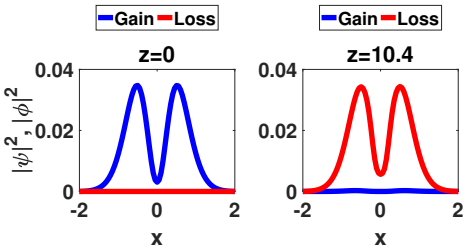

(a) P_N=0.01,ϵ=0.1

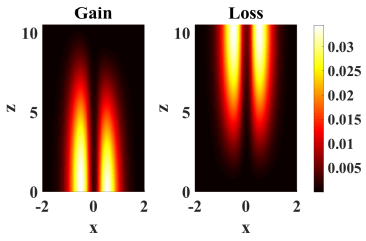

(b) P_N=0.01,ϵ=0.1

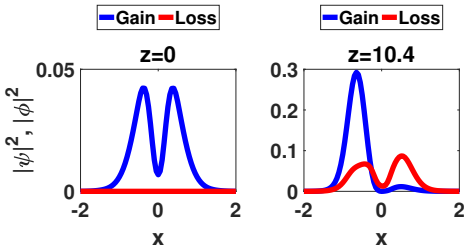

(c) P_N=0.01,ϵ=1.2

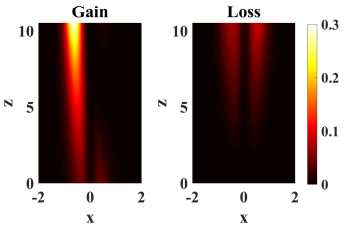

(d) P_N=0.01,v=1,ϵ=1.2

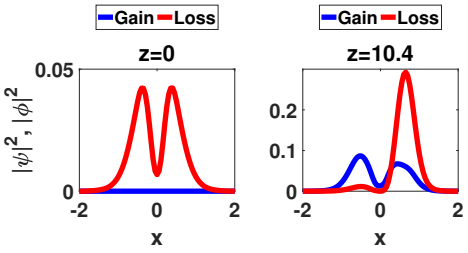

(e) P_N=0.01,ϵ=1.2

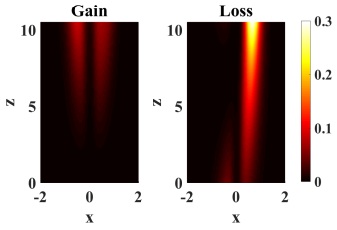

(f) P_N=0.01,ϵ=1.2

Figure 6.11: The switching dynamics of the coupled system in the defocusing nonlinearity ($\beta = -5$) in the PT and broken PT regimes at $v = 1, k = 1$ and $P_N = 0.01$. Top panel: in the PT-symmetric regime, middle panel: in the broken PT regime by exciting the gain channel and bottom panel: in the broken PT regime by exciting the lossy channel.

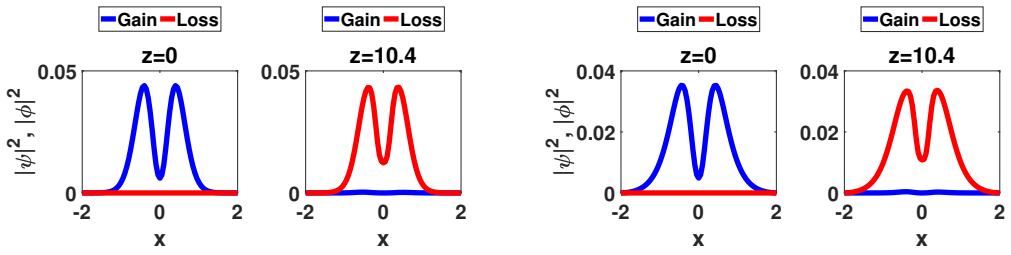

(a) v=2,k=1 (b) v=1,k=2

Figure 6.12: The effect of real potential and width of the potential on switching dynamics in the defocusing nonlinearity ($\beta = -5$) in the PT-regime ($\epsilon = 0.1$) for very low input at (a) $v = 2$ and (b) $k = 2$.

light transport. When the gain (lossy) channel is excited, the power is confined in the negative x (positive x) region of the same channel, i.e., power is trapped in the well region of the antisymmetric imaginary potential.

The nature of the field switched from the gain to the lossy channel by increasing the coefficient of real potential and width of the potential are studied. From Fig. 6.12(a) it is evident that as v increases the depth of the central dip of the oscillating field is reduced in the PT regime. Also, the depth of the dip is decreased at the coupling length by decreasing the width of the potential in the PT phase as shown in Fig. 6.12(b).

Fig. 6.13 illustrates the switching dynamics when a high input is given in the gain channel. When $P_N = 0.25$, more than 50% of the power is trapped in the gain channel in the PT region as shown in Figs. 6.13(a) and (e). Almost entire power injected is confined in the gain channel in the broken PT region which are shown in Figs. 6.13(b) and (f). In the PT regime, the trapped beam power is almost constant during propagation, whereas the power drastically grows up in the well region of the imaginary potential in the broken PT phase due to the effect of ϵ which are evident from Figs. 6.13(e) and (f), respectively. The system is also studied when the input is very high ($P_N = 0.64$). Figs. 6.13(c) and (d) show that the complete power confinement occurs at a lower value of ϵ in this case.

The switching curve has been plotted between normalized input power (P_N) and transmission coefficient (T) to study the effect of ϵ and k in the input power dependent switching. At $P_N > P_r$, more than 50% of the input power is trapped in

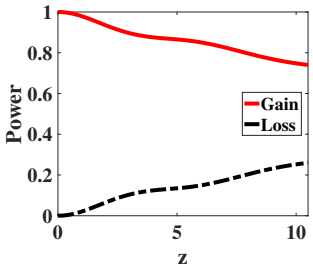

(a) P_N=0.25,ϵ=0.1

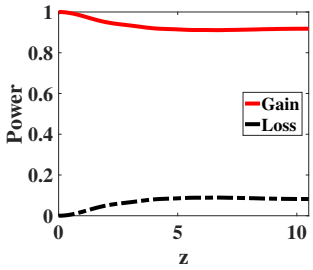

(b) P_N=0.25,ϵ=1.2

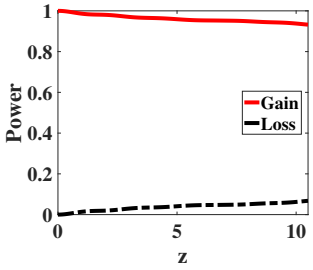

(c) P_N=0.64,ϵ=0.1

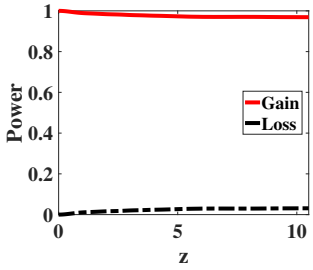

(d) P_N=0.64,ϵ=1.2

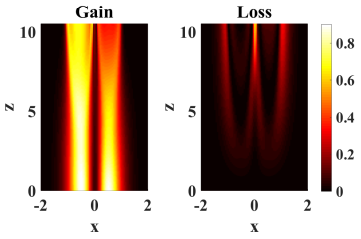

(e) P_N=0.25,ϵ=0.1

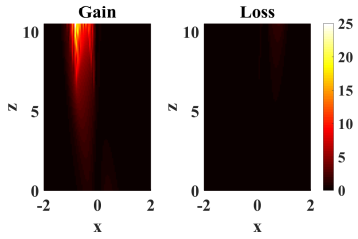

(f) P_N=0.25,ϵ=1.2

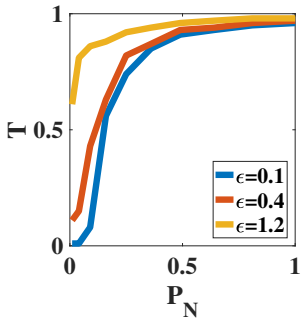

(g) $k = 1$

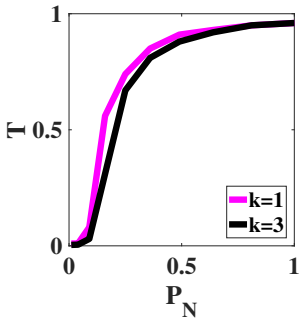

(h) ϵ=0.1,$v = 1$

Figure 6.13: The switching dynamics of the system in the defocusing nonlinearity ($\beta = -5$) for high input $P_N = 0.25, 0.64$. First and second row: power vs z in the PT ($\epsilon = 0.1$) and broken PT regimes ($\epsilon = 1.2$). Third row: field dynamics at $P_N = 0.25$ and $\epsilon = 0.1, 1.2$. Fourth row: switching curves (g) T vs P_N by varying ϵ and (h) T vs P_N by varying k.

the excited channel. The switching curve for different gain/loss coefficients are as plotted in Fig. 6.13(g). The blue and red plots depict that P_r is low for high values of ϵ in the PT phase, whereas the yellow plot indicates that power gets trapped at a very low input in the broken PT phase. The gain/loss effects hinder power oscillation in the PT regime, which find applications in directed energy transport. Also, Fig. 6.13(h) shows the influence of the width of the potential on P_r at $\epsilon = 0.1$. P_r is low for low k (high width) values.

6.4 Conclusion

The single and coupled systems with k-wavenumber Scarf II barrier potential have been studied. The single system gives rise to eigenmodes with central peaks in the linear case. A weak defocusing nonlinearity admits bright soliton form of solution and strong nonlinearity leads to dark-soliton-like solutions in the PT regime, in single and coupled systems. For coupled system, in the PT regime, the power oscillation occurs between the channels for very low input, whereas power in the excited channel gets trapped keeping constant power during propagation for high input. On the other hand, in the broken PT regime, the power is trapped in the well region of the antisymmetric imaginary potential and it grows up during propagation for low and high input power. The effective balancing between the diffraction, self-defocusing nonlinearity and PT-symmetric barrier potential in single and coupled systems lead to localised stable solutions with central dips in the PT regime which find applications in controlled optical signal transmission and switching circuits. Also, by increasing the gain/loss coefficient and the width of the potential, the power confinement in the excited channel can be enhanced in the broken PT regime that has relevance in non-reciprocal and unidirectional signal transport.

Chapter 7

Beam dynamics in coupled NLSE with super-Gaussian barrier potential

7.1 Introduction

In nonlinear optics, the realisation of PT-symmetric systems with refractive index barrier distributions of Gaussian and super-Gaussian form has great importance due to applications like localisation of light signals, all-optical switching and unidirectional optical valves. The nonlinear non-Hermitian PT-symmetric coupled system has opened many ways for the developments in the engineering of advanced functional components and materials in photonics. The researchers have investigated the existence of solitons in nonlinear fractional Schrodinger equation supported with PT-symmetric periodic [99], Gaussian [100] and Scarf II potentials [101]. Recently, stable solitons of the logarithmic NLSE in PT system with non-periodic potentials [102] are studied. Nonlinear PT-symmetric coupled systems with varying gain/loss coefficients, nonlinear gain/loss effect and competing cubic-quintic nonlinearities [103] have been discussed. The switching dynamics of the nonlocal nonlinear coupler with PT- symmetric transverse potential and soliton steering dynamics in a PT-symmetric directional coupler having higher-order perturbative effects have been

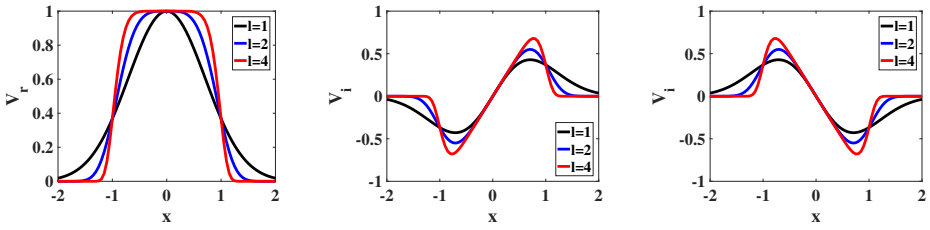

(a) V_r (b) V_i, Gain channel (c) V_i, Lossy channel

Figure 7.1: The real and imaginary components of super-Gaussian barrier potential in the gain and lossy channels with k=1 and ϵ=1 for $l = 1, 2, 4$

investigated. The existence and dynamics of dark soliton-like solutions in single and coupled systems of defocusing Kerr nonlinearity with PT-symmetric super-Gaussian and k-wavenumber Scarf II well potentials [104] have been studied recently. The studies on the eigenmodes of the coupled system with super-Gaussian barrier potential in a medium encompassing defocusing Kerr nonlinearity in PT and broken PT regimes have relevance in nonlinear optical switching and non-reciprocal light transmission processes.

In this chapter, the stationary and dynamical solutions of the ground and excited states in self-defocusing nonlinear coupled systems with PT-symmetric super-Gaussian barrier potential have been analyzed. The study addresses how the imaginary part of the potential influences the PT-symmetry breaking at a critical threshold. The theoretical model of the system has been introduced in Section 7.2. The stationary eigenmodes of ground and excited states and the effect of the nonlinearity, coupling and PT-symmetric potential on the eigenvalue spectra are discussed under this section. The stability of the solution using linear stability analysis has been studied in Section 7.3. In Section 7.4, the beam dynamics of the low and high-frequancy modes and the power oscillation between the gain and lossy channels have been analyzed. Section 7.5 concludes the chapter.

7.2 The model

The beam evolution in a nonlinear PT-symmetric coupled system with transverse potential has the form:

$$
\begin{aligned}
i\psi_z + \tfrac{d}{2}\psi_{xx} + \beta|\psi|^2\psi + (V_r + iV_i)\psi + C\phi = 0 \\
i\phi_z + \tfrac{d}{2}\phi_{xx} + \beta|\phi|^2\phi + (V_r - iV_i)\phi + C\psi = 0,
\end{aligned}
\tag{7.1}
$$

where $\psi(x,z)$ and $\phi(x,z)$ are the beam amplitudes in the two channels. ψ_z is the first derivative in z and ψ_{xx} is the second derivative in x. The real constants d, β and C represent the coefficients of diffraction, nonlinearity and coupling. $\beta < 0$ represents the self-defocusing nonlinearity. V_r and V_i are the real and imaginary components of the PT-symmetric potential. PT-symmetric super-Gaussian potential can be achieved by suitably tuning the parameters of even and odd transverse profiles of the form,

$$
\begin{aligned}
V_r &= k\ \exp(-x^{2l}) \\
V_i &= \epsilon\ x\ \exp(-x^{2l}),
\end{aligned}
\tag{7.2}
$$

where k refers to the amplitude of the real potential and $k > 0$ gives the super-Gaussian barrier form. ϵ is the strength of the imaginary potential (gain/loss coefficient). $l = 1$ represents the Gaussian potential and $l > 1$ gives the super-Gaussian form. V_r and V_i profiles for $k > 0$ are shown in Fig. 7.1. As l increases, the shape of the central peak of V_r becomes wider and flattens with the same amplitude k . However, only small changes occur for V_i with l [105, 106].

Equation (7.1) leads to eigenvalue equation by considering the solutions in the form,

$$
\begin{aligned}
\psi(x,z) &= U(x)\ \mathrm{e}^{-i(\mu z - \theta_1)} \\
\phi(x,z) &= U(x)\ \mathrm{e}^{-i(\mu z - \theta_2)},
\end{aligned}
\tag{7.3}
$$

where $U(x)$ gives the stationary solution and μ is the propagation constant. The eigenvalue equation satisfied by the stationary solution is of the form

$$
\mu U = -\frac{d}{2}\, U_{xx} - \beta\ |U|^2\ U - V_r\ U - C\ \cos\delta\ U, \tag{7.4}
$$

where $C\cos\delta = \sqrt{C^2 - V_i^2}$ and $\delta = \theta_1 - \theta_2$. When $\cos\delta > 0$, it implies the high-frequency mode (U_H) while $\cos\delta < 0$ refers to the low-frequency mode (U_L). The

system has been studied in the nonlinear regime using the Gaussian form of input with boundary values of the transverse coordinate ranging from $x = -2$ to $x = 2$ and constant diffraction coefficient ($d = 1$).

7.2.1 The eigenspectra

Equation (7.4) has been solved numerically and the stationary eigenmodes of the ground and excited states have been analyzed. The effect of the coefficients of the imaginary potential, coupling constant, nonlinearity and l values on the eigenspectra of the low and high-frequency modes are studied.

The variation of the real and imaginary eigenvalues (μ_r and μ_i) with the gain/loss coefficient (ϵ) at $l = 1, 2, 4$ are illustrated in Fig. 7.2. The top panel of Fig. 7.2 refers to the real eigenvalues of the ground, 2nd and 4th excited states. The blue and red dotted plots of the figure indicate real eigenvalues of the high and low-frequency modes, respectively, of the ground state. For these modes, the real eigenvalues are distinct for small values of ϵ. As ϵ increases, the difference between real eigenvalues of the eigenmodes decreases. The orange and purple colored dots shown in Figs. 7.2(a)-(c) are the real eigenvalues of the high and low-frequency modes of the 2nd excited state. And, the green and sky-blue colored dots refer to that of the 4th excited state. For the excited states, the results are similar to that of the ground state in the PT-symmetric regime.

The blue and red dotted plots of the middle panels of Fig. 7.2 show the imaginary eigenvalues of the high and low-frequency modes of the ground state. Figs. 7.2(d)-(f) represent the imaginary eigenvalues of the ground and excited states for $l = 1, 2, 4$, respectively. The imaginary eigenvalues of the ground state are zero up to the threshold value, ϵ_{th}. For $\epsilon > \epsilon_{th}$, the imaginary eigenvalues grow with ϵ. The region with zero imaginary eigenvalues, even with an imaginary potential, is called PT-symmetric regime. The region with imaginary eigenvalues is called the broken PT-symmetric regime.

Upon increasing l values, only slight increases are observed in the extremum value of the imaginary potential and corresponding x values. For $l = 1, 2$ the extremum value of the imaginary potential occurs at $x = \pm 0.7$, irrespective of

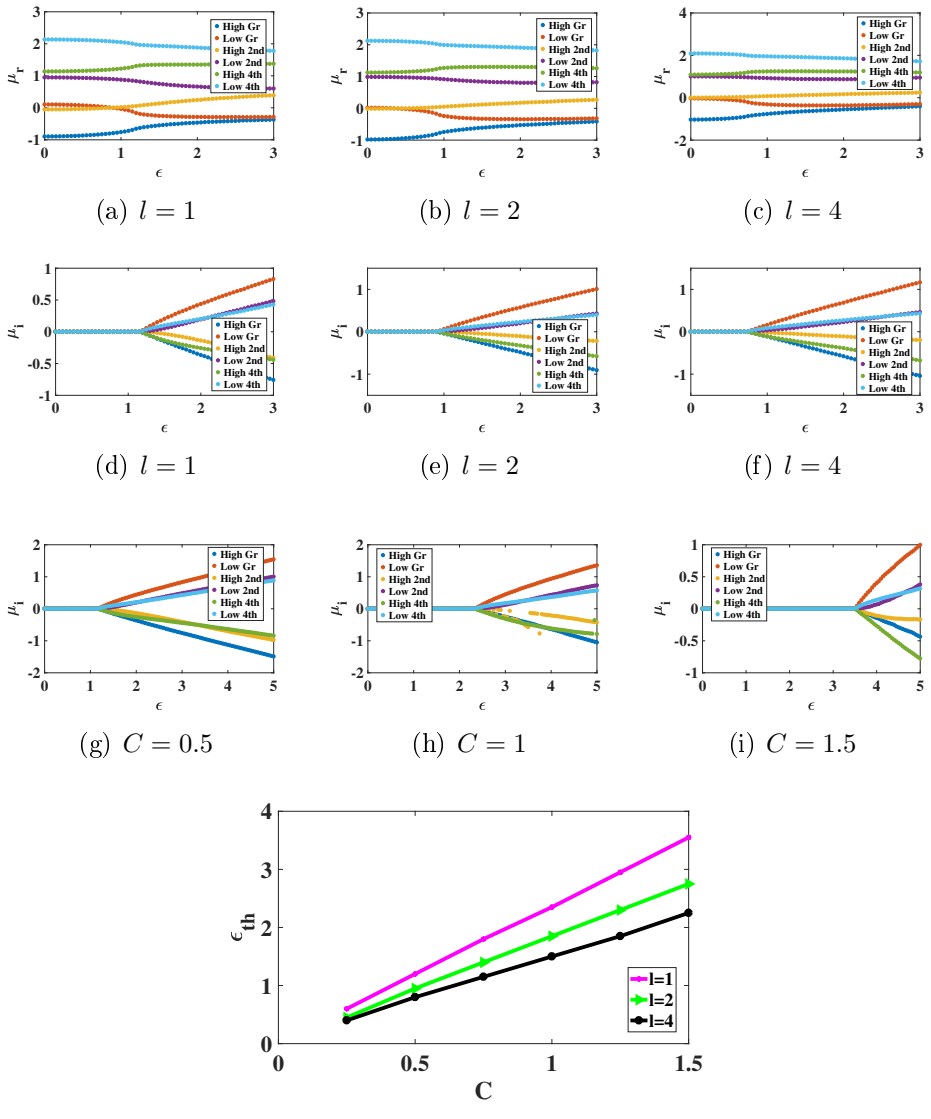

(a) $l = 1$ (b) $l = 2$ (c) $l = 4$

(d) $l = 1$ (e) $l = 2$ (f) $l = 4$

(g) $C = 0.5$ (h) $C = 1$ (i) $C = 1.5$

(j) ϵ_{th} vs C

Figure 7.2: The real and imaginary eigenvalues with ϵ for $l = 1, 2, 4$ and $C = 0.5, 1, 1.5$ at $\beta = -3$ and $k = 1$. Top panel: μ_r vs ϵ, middle panels: μ_i vs ϵ and bottom panel: ϵ_{th} vs C.

	C	0.1	0.5	1	1.5
$l = 1$		0.234	1.17	2.34	3.5
$l = 2$	ϵ_{th}	0.182	0.91	1.82	2.73
$l = 4$		0.148	0.74	1.48	2.22

Table 7.1: The threshold values of the gain/loss coefficient for different values of coupling constants at $l = 1, 2, 4$ for $\beta = -3$ and $k = 1$.

the parameter ϵ. The threshold value of the gain/loss coefficient, ϵ_{th}, is higher for Gaussian potential ($l = 1$) than that of the super-Gaussian potentials ($l = 2, 4$). By tailoring the transverse distribution of the complex refractive index profile, the threshold conditions of the PT-phase transition can be achieved.

The orange and purple coloured plots of the middle panels of Fig. 7.2 refer to the imaginary eigenvalues of the high and low-frequency modes of the 2nd excited state, whereas the green and sky-blue coloured plots refer to that of the 4th excited state. In the PT-symmetric regime, the variation of the imaginary eigenvalues of the excited states with ϵ is similar to the ground state and all the states have the same threshold values when other parameters are fixed.

The imaginary eigenvalues of the high and low-frequency modes of the ground and excited states for different coupling constants are depicted in Figs. 7.2(g)-(i). The eigenvalues are real when $C \geq V_i$(extremum), i.e., when the system is in the PT regime. The transition from the PT phase, with real eigenvalues, to the broken PT phase, with complex eigenvalues, occurs at $C = V_i$(extremum). This abrupt phase transition triggers different optical properties like unidirectional light propagation. The change in the threshold values with the coupling constant is as shown in Fig. 7.2(j). The magenta, green and black colored plots indicate the variations at $l = 1, 2$ and 4, respectively. The numerical values of ϵ_{th} for small coupling constants are given in Table 7.1. It is evident that the coupling enhances the PT-symmetry. Also, the table verifies that the super-Gaussian potentials take a lower threshold value of the PT-phase transition, in comparison with Gaussian potential for a constant C.

The eigenfunctions of the ground and excited states in PT-symmetric and broken PT-symmetric regimes are as shown in Fig. 7.3. The high and low-frequency eigenmodes of the ground state are represented as blue and red plots in Figs. 7.3(a)-(f).

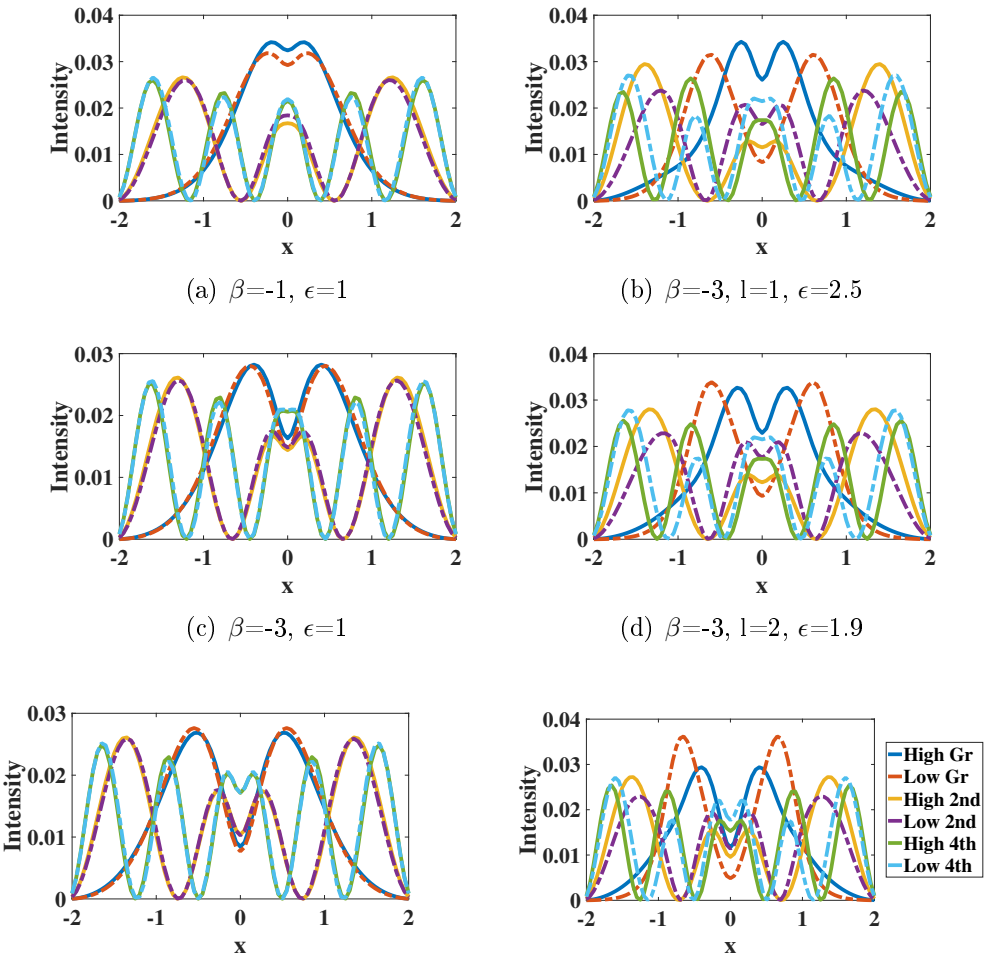

(a) β=-1, ϵ=1 (b) β=-3, l=1, ϵ=2.5

(c) β=-3, ϵ=1 (d) β=-3, l=2, ϵ=1.9

(e) β=-5, ϵ=1 (f) β=-3, l=4, ϵ=1.6

Figure 7.3: The high and low-frequency eigenmodes in the nonlinear regime in PT-symmetric (ϵ=1) and broken PT-symmetric regimes (ϵ=2.5, 1.9, 1.6) at $C = 1$ and $k = 1$. First column: in the PT regime for $l = 1$ at (a) $\beta = -1$, (c) $\beta = -3$ and (e) $\beta = -5$. Second column: in the broken PT regime for $\beta = -3$ at (b) $l = 1$, (d) $l = 2$ and (f) $l = 4$.

And, the orange and purple colored plots indicate the high and low-frequency modes of the 2nd excited state. Also, the green and sky-blue colored plots refer to that of the 4th excited state. For the ground and excited states, the high and low-frequency modes of each state merge in the nonlinear PT-symmetric regime ($\epsilon = 1$), which is shown in the first column of Fig. 7.3. But in the broken PT regime, the high and low-frequency eigenmodes of each state split each other as shown in the second column of Fig. 7.3.

Fig. 7.3(a) show that for small values of the defocusing nonlinearity ($\beta = -1$), only the ground state has a dip and excited states have bubbles at the center of the transverse coordinate ($x = 0$). But for high values of the nonlinearity ($\beta = -3, -5$), the dips are evolved at $x = 0$ for the excited states also, which is depicted in Figs. 7.3(c) and (e). The depth of the dip increases with the strength of the nonlinearity coefficient.

7.3 The stability of stationary states

The linear stability analysis of the stationary solutions of the ground and excited states in the PT-symmetric Gaussian potential has been analysed using the linearised BDG equations,

$$\lambda \begin{bmatrix} p_1 \\ q_1^* \\ p_2 \\ q_2^* \end{bmatrix} = \begin{bmatrix} L_1 + iV_i & \beta U^2 & Ce^{-i\delta} & 0 \\ -\beta U^{*2} & -L_1 + iV_i & 0 & -Ce^{i\delta} \\ Ce^{i\delta} & 0 & L_1 - iV_i & \beta U^2 \\ 0 & -Ce^{-i\delta} & -\beta U^{*2} & -L_1 - iV_i) \end{bmatrix} \begin{bmatrix} p_1 \\ q_1^* \\ p_2 \\ q_2^* \end{bmatrix}. \tag{7.5}$$

Where $L_1 = \mu + \frac{d}{2}\frac{d^2}{dx^2} + 2\beta|U|^2 + V_r$ and $Ce^{i\delta} = \sqrt{C^2 - V_i^2} + iV_i$.

The perturbation eigenvalue spectra of the low and high-frequency modes are studied for the ground and excited states which is shown in Fig. 7.4. The magenta and black coloured dots shown in Fig. 7.4(a) indicate λ values of the high and low-frequency modes, respectively, of the ground state in the PT regime ($\epsilon = 1$). It is evident that the perturbation eigenvalues are real in this regime. So, the eigenmodes

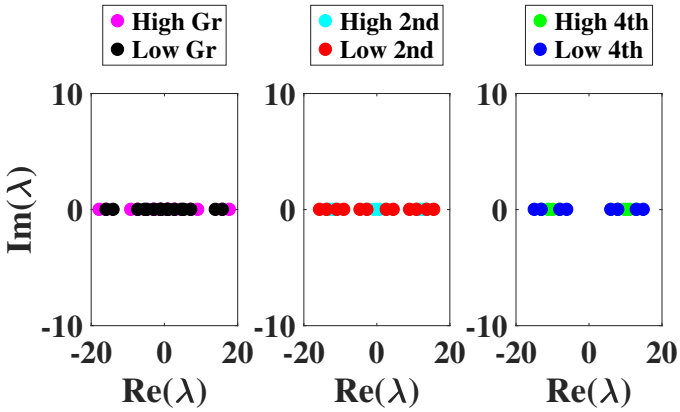

(a) $\epsilon = 1, C = 1, \beta = -3$

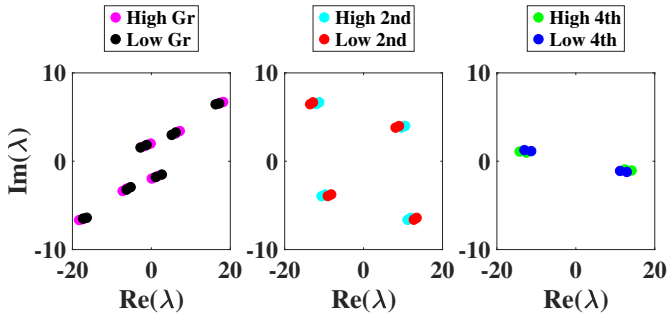

(b) $\epsilon = 2.5, C = 1, \beta = -3$

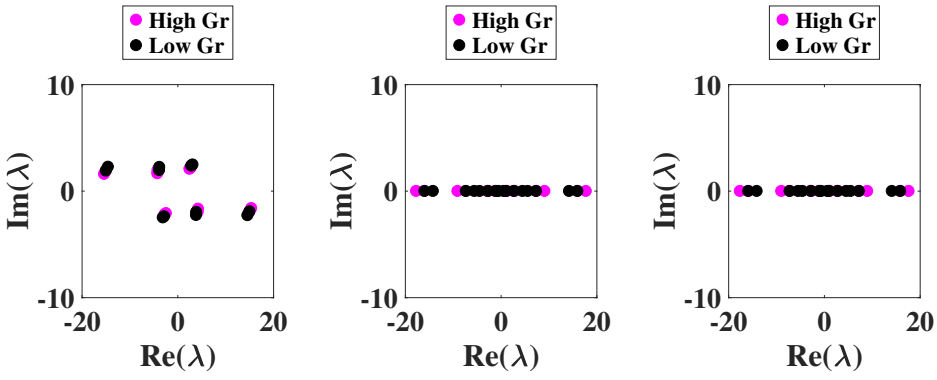

(c) ϵ=1.5,C=0.5,β=-3 (d) ϵ=1.5,C=1,β=-3 (e) ϵ=1.5,C=1,β=-5

Figure 7.4: Linear-stability spectra for the stable and unstable eigenmodes of the ground and excited states with Gaussian potential at $d = 1$ and $k = 1$.

of the ground state are linearly stable. Fig. 7.4(b) shows that the values of λ of the ground state high and low-frequency modes are complex and show oscillatory instability in the broken PT-symmetric regime ($\epsilon = 2.5$). The cyan and red colored dots, respectively, of Figs. 7.4(a) and (b) refer to the perturbation eigenvalues of the high and low-frequency modes of the 2nd excited state. Also, λ values of the high and low-frequency modes, respectively, of the 4th excited state are indicated by the green and blue dots in Figs. 7.4(a) and (b). In the PT regime ($\epsilon = 1$), it has been shown that the excited states are also linearly stable and exhibit oscillatory instability in the broken PT regime ($\epsilon = 2.5$).

Figs. 7.4(c) and (d) illustrate the stability spectrum by varying the coupling constants. For the ground state, λ is complex at $C = 0.5$ when $\epsilon = 1.5$, which is depicted in Fig. 7.4(c). That is, the solution is linearly unstable in this parametric region. Whereas, Fig. 7.4(d) shows that the eigenmodes are linearly stable at $C = 1$ when all other parameters are the same. It verifies the observation that as the coupling constant increases, the threshold value of the PT breaking also increases. And no change in the stability of the solution is visible with β variation, which is evident from Figs. 7.4(d) and (e). Similar behaviors are shown by the excited states also. The coefficient of transverse gain/loss distribution and the coupling constant affect the evolution of stable eigenmodes of the ground and excited states.

7.4 Beam dynamics

The propagation of the stationary states of high and low-frequency modes of the ground state has been studied using Equation (7.3) and the beam evolution is as shown in Fig. 7.5. Both the nonlinear modes give rise to a stable localised beam propagation in the PT-symmetric regime ($\epsilon = 1$) which is clearly illustrated in Fig. 7.5(a). Whereas in the broken PT-regime ($\epsilon = 2.5$), the high and low-frequency modes show opposing behavior and the beam evolution is unstable in the z-direction, which is evident in Fig. 7.5(b). The spatial overlap between the nonlinear modes and the super-Gaussian gain/loss distribution induces stable beam propagation in the PT-symmetric regime for some parametric regions. The boosting of the PT-

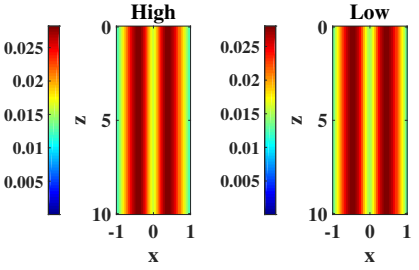

(a) $\epsilon = 1, C = 1, \beta = -3$

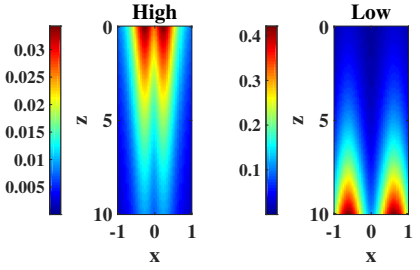

(b) $\epsilon = 2.5, C = 1, \beta = -3$

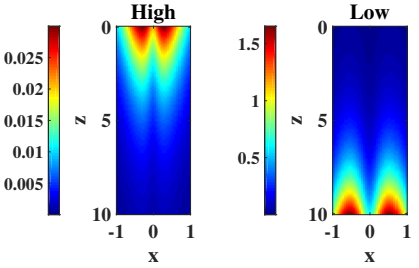

(c) $\epsilon = 1.5, C = 0.5, \beta = -3$

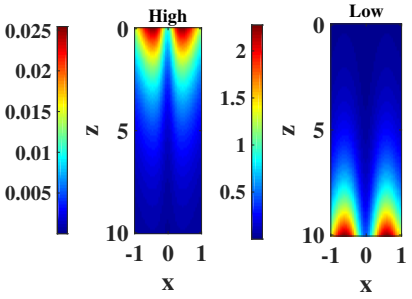

(d) $\epsilon = 1.5, C = 0.5, \beta = -5$

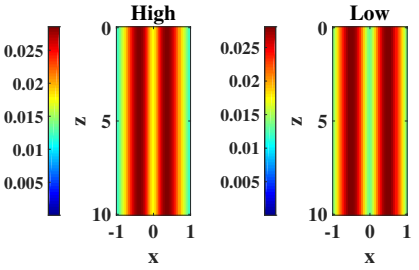

(e) $\epsilon = 1.5, C = 1, \beta = -3$

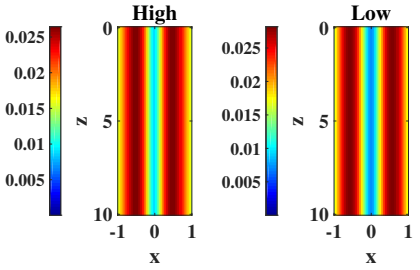

(f) $\epsilon = 1.5, C = 1, \beta = -5$

Figure 7.5: The beam dynamics of the ground state in the PT and broken PT phases at $l = 1$, $k = 1$ and $d = 1$.

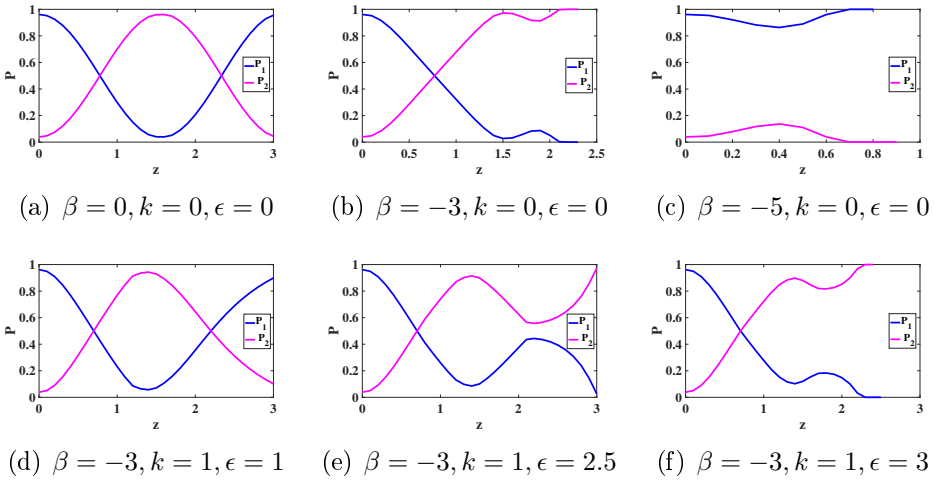

(a) $\beta = 0, k = 0, \epsilon = 0$ (b) $\beta = -3, k = 0, \epsilon = 0$ (c) $\beta = -5, k = 0, \epsilon = 0$

(d) $\beta = -3, k = 1, \epsilon = 1$ (e) $\beta = -3, k = 1, \epsilon = 2.5$ (f) $\beta = -3, k = 1, \epsilon = 3$

Figure 7.6: The relative power distribution of the solutions in the two channels in the PT and broken PT regimes with $l = 1$. Top panel: (a) for $\beta = 0$, (b) $\beta = -3$ and (c) $\beta = -5$. Bottom panel: at $\beta = -3$ for (d) in the PT regime and (e),(f) in the broken PT regime.

symmetry with the coupling has been confirmed in Figs. 7.5(c)-(f). In the PT regime, the stable beam propagates with a dip at the center ($x = 0$) as shown in Fig. 7.5(e). From Fig. 7.5(f), it is obvious that when β is increased, the depth of the central intensity dips of both the high and low-frequency modes are increased.

7.4.1 Power oscillation

The power distribution of the fundamental state in the two channels has been analyzed by solving nonlinear coupled Equation (7.1). The power distribution of the gain channel is given by $p_1 = \int_{-\infty}^{\infty} |\psi|^2 \, dx$ and the lossy channel by $p_2 = \int_{-\infty}^{\infty} |\phi|^2 \, dx$. The relative power of the gain channel, P_1, is the ratio between p_1 and the total power $P_T = p_1 + p_2$. Similarly, the relative power of the lossy channel, P_2, is the ratio between p_2 and P_T.

When only the gain channel is excited initially with $P_1(0) = 1$ at $\beta = 0$ and in the absence of PT-symmetric potential, the power is transferred from the first to the second channel. The plots are as shown in Fig. 7.6(a), where the blue and magenta colors, respectively, represent the relative powers in the gain and lossy channels. The minimum value of z at which the input power is completely transferred from one channel to the other is called the first coupling length, ζ. The blue and

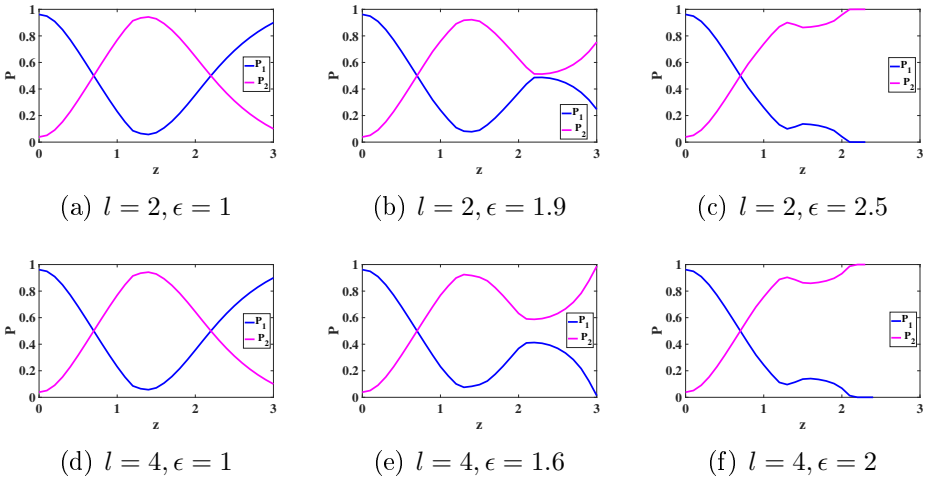

(a) $l = 2, \epsilon = 1$ (b) $l = 2, \epsilon = 1.9$ (c) $l = 2, \epsilon = 2.5$

(d) $l = 4, \epsilon = 1$ (e) $l = 4, \epsilon = 1.6$ (f) $l = 4, \epsilon = 2$

Figure 7.7: The relative power distribution of the solutions in the two channels for super-Gaussian potentials ($l = 2, 4$) at $d = 0.001, C = 1, \beta = -3, k = 1$.

magenta plots of Figs. 7.6(b) and (c) refer to the relative power in gain and lossy channels, respectively, in the defocusing nonlinear system without PT symmetry. It is shown that for $\beta = -3$, the power switches between the channels, initially, and is then trapped in a single channel during the propagation. When the coefficient of nonlinearity is increased ($\beta = -5$), the power switching is stopped and the power is confined in a single channel. The Gaussian PT symmetry is introduced in the nonlinear system and the relative powers in the gain and lossy channels are plotted as blue and magenta curves in Figs. 7.6(d)-(f). The system retrieves the power switching behavior in the PT-symmetric regime, which is evident in Fig. 7.6(d). Above the threshold value of the *PT*-symmetry breaking, the switching behavior again stopped after the first coupling length which is shown in Figs. 7.6(e) and (f).

The power distribution in the gain (blue) and lossy (magenta) channels in the nonlinear regime ($\beta = -3$) with PT-symmetric super-Gaussian potentials are illustrated in Fig. 7.7. The top panel of the figure is for $l = 2$ and the bottom panel is for $l = 4$. In the PT-symmetric regime, the power switches between the gain and lossy channels with propagation as shown in Figs. 7.7(a) and (d). Whereas, Figs. 7.7(b),(c),(e) and (f) depict that the solutions are trapped in a single channel after crossing the first coupling length in the broken PT regime. As l increases the threshold value of the gain/loss coefficient, at which the power trapped in a single

channel, is decreased. The threshold values of the PT-symmetry breaking have been studied for the stationary states and switching dynamics at $l = 1, 2, 4$. Both the results are in good agreement.

7.5 Conclusion

We have analyzed the stationary states and switching dynamics of coupled systems with self-defocusing nonlinearity, and PT-symmetric super-Gaussian barrier potential. The stationary solutions are studied for low and high-frequency eigenmodes of the fundamental and higher states. The influence of the imaginary potential on the threshold value of the PT phase transition and the effect of the nonlinearity on the eigenmodes have been analyzed. In Gaussian and super-Gaussian potentials, the phase transition from the PT to the broken PT-symmetry occurs at a threshold value of the gain/loss coefficient. The eigenvalues of the high and low-frequency modes are real in the PT regime and are complex in the broken PT regime for the ground and excited states. The study shows that as the power of the exponential term of the super-Gaussian potential increases, the threshold value decreases. But, the coupling enhances the PT-symmetry. The fundamental eigenmodes have a small dip at the center of the transverse coordinate for small values of the defocusing nonlinearity. As the nonlinearity increases the dips are evolved at the center for the higher eigenstates also. The depth of the dip increases with the coefficient of nonlinearity. The high and low-frequency modes of each of the eigenstates merge in the PT regime, whereas it split each other with different complex eigenvalues in the broken PT regime. The linear stability analysis shows that both the high and low modes of the eigenstates are stable in the region of PT-symmetry. The eigenmodes show oscillatory instability in the broken PT regime. The existence of stable eigenmodes with central dip has been realized by the effective steering of the PT-symmetric super-Gaussian complex distribution of the refractive index in a self-defocusing nonlinear medium. The power distribution, with the propagation, of the fundamental solutions in the gain and lossy channels is discussed by exciting one of the channels. Without PT-symmetry, the power switching between the two

channels is observed in the linear regime, whereas this behavior is lost in the nonlinear regime. When the PT-symmetric Gaussian and super-Gaussian potentials are introduced the property of power switching is recovered until the threshold value of the gain/loss coefficient. In the broken PT regime, the dynamical solutions are trapped in a single channel.

Chapter 8

Results and Recommendations

The major findings in the thesis are summarised and the recommendations for future studies based on our results are proposed in this chapter. In the thesis, we studied the eigenmodes, propagation and switching dynamics of the PT-symmetric optical systems with self-defocusing nonlinearity. Single and coupled systems with PT-symmetric super-Gaussian and k-wavenumber Scarf II potentials with well and barrier distributions are analysed in this study. In optical systems, the real and imaginary components of the PT-symmetric potential take the role of the transverse refractive index distribution and gain or loss effects in the system, respectively. The real part of k-wavenumber Scarf II and super-Gaussian potentials comprise different profiles of refractive index from smooth to step-index distributions. The major results are given in Section 8.1 and the future prospects are given in Section 8.2.

8.1 Results

- The stationary solutions of the ground and excited states with PT-symmetric super-Gaussian and k-wavenumber Scarf II well potentials, in linear and defocusing nonlinear single systems are studied in Chapter 2 and Chapter 3.

    * Phase transition from PT-symmetry to broken PT-symmetry occurs at a threshold value of the coefficient of imaginary potential, in both linear and nonlinear regimes. For super-Gaussian, the threshold value ei-

ther increases or remains constant when the shape of the real potential changes from smooth Gaussian well to step-index profile, depending on the distribution of the imaginary potential. For k-wavenumber Scarf II, by narrowing the real potential the threshold value is increased. When the depth of the real potential increases, the threshold value decreases for both potentials.

  * The eigenvalues are real below the threshold value, i.e., in the unbroken PT regime. Whereas the eigenvalues are complex above the threshold value, i.e., in the broken PT regime. The threshold values are equal for the pair of ground and first excited states. For super-Gaussian potential, 2nd and 3rd excited states are also studied. For this pair, the threshold values are equal but higher than the first pair.

  * For both the potentials, the eigenmodes are symmetric in the PT phase and are asymmetric in the broken PT phase. The ground state shows single dip dark soliton-like solution, whereas second excited state shows multi-dip solution.

  * The self-defocusing nonlinearity enhances the PT-symmetry for super-Gaussian potential, whereas it suppresses the PT-symmetry for k-wavenumber Scarf II potential.

  * The stability of the solutions are studied using linearised BDG equations. It has been found that the stationary states are stable in the PT regime and are unstable in the broken PT regime. Stable propagation without any loss are also observed in the PT regime.

- The study has been extended to coupled system with equal gain and loss effects in Chapter 4. The low and high-frequency modes of the ground, 2nd and 4th eigenstates are studied, numerically. The power oscillation between the channels is analysed by reducing two-coupled PDEs into four-coupled ODEs using variational analysis.

  * In the PT regime, the high and low-frequency modes have distinct real

eigenvalues and same eigenfunctions. For low values of defocusing nonlinearity, the solutions show central intensity peak but when the strength of the nonlinearity increases solutions with central dip is formed. In the broken PT-regime, the eigenvalues of the high and low-frequency modes become complex conjugates.

  * The propagation dynamics show that beam evolution is stable and the power remains constant in the PT-symmetric regime. When PT-symmetry gets broken, the propagation becomes unstable and the power increases for the high-frequency mode, whereas it decreases for the low-frequency eigenmode.

  * The power variation of high and low-frequency modes in the gain and lossy channels are studied using variational analysis, by exciting one of the channels, for different gain/loss coefficients. The power oscillation occurs between the channels in the PT-symmetric regime, whereas in the broken PT regime, power confines in a single channel for these two modes.

- The switching dynamics of the PT-symmetric coupled system with k-wavenumber Scarf II well potential in linear and self-defocusing nonlinear media have been analysed in Chapter 5. The eigenmodes of ground and even excited states are analysed because the eigenfunctions are symmetric for these states. Whereas for odd excited states antisymmetric eigenfunctions are formed which lead to zero intensity dip at the centre.

  * In linear system, the ground and even excited modes have central intensity bubbles, whereas the ground and even excited states show central intensity dips in the defocusing nonlinear regime. In the PT phase, the high and low-frequency modes are the same and the coupling enhances the PT-symmetry, for both cases. For nonlinear mode, the depth of the dip depends on the strength of the nonlinearity, the depth of the real potential well and the width of the potential. PT-symmetric systems with self-defocusing nonlinearity generate linearly stable localised solutions of dark soliton form.

* The power oscillation has been studied using finite difference beam propagation method. In the linear system, the power oscillates between the channels and it is independent of the input power, whereas the system with high gain/loss inhibits the power transfer. In the nonlinear system, the power transfer occurs at a small input power, whereas the power is trapped in the excited channel for high input. The input-dependent switching dynamics shows that the critical input power, at which 50% of the input trapped in the gain channel, is decreased by increasing the gain/loss effects and the width of the potential.

- In Chapter 6 and Chapter 7, the eigenmodes and intensity-dependent switching dynamics of single and coupled systems with k-wavenumber Scarf II and super-Gaussian barrier potentials have been studied.

  * As the coupling increases the threshold value of the gain/loss coefficient increases.

  * The eigenmodes with central peak is formed for weak nonlinearity because of the effect of the barrier potential. The stationary solution with central dip is formed for strong nonlinearity and its depth increases with the coefficient of nonlinearity.

  * In k-wavenumber Scarf II barrier, single system which admits dark soliton-like solutions and the power oscillation in two-channel coupled system are analysed for low and high inputs. In the PT regime, power transfer occurs between the channels for very low input but it confines in the excited channel with constant power for high input. Power gets trapped in the well region of the antisymmetric imaginary potential and power grows for low and high inputs, in the broken PT phase. The gain/loss coefficient enhances power confinement in the broken PT regime. Also, the switching curve between the input intensity and transmission coefficient reveals that the critical input power is low for high gain/loss and high width of k-wavenumber Scarf II potential.

* For supar-Gaussian coupled system, the high and low modes are studied. The eigenstates of both the modes merge in the PT regime, whereas that split each other with different complex eigenvalues in the broken PT regime.

* For coupled system, the power distribution during propagation in the gain and lossy channels is discussed by exciting one of the channels with the stationary solution. For low input, the power oscillation is found until a threshold value of the gain/loss coefficient. In the broken PT regime, the dynamical solutions are trapped in a single channel.

In single system, the existence of dark soliton-like solution with depression at the center has importance due to its unique properties for a plethora of applications. As the dark soliton exhibits more stability against losses than bright soliton, the experimental realisation of these models may have widespread applications in long-distance energy-efficient communication technology. The interplay between the effects of nonlinearity and the coefficients of real and imaginary components of the PT-symmetric potential influence the switching dynamics in a coupled system, that can contribute in the construction of switching devices. The gain/loss coefficient enhances power confinement in the broken PT regime that has relevance in non-reciprocal and unidirectional signal transmission.

8.2 Recommendations

- The study can be extended to PT-symmetric single and coupled systems with different types of self-defocusing nonlinearity such as nonlocal, cubic-quartic, quintic-septimal, cubic-quintic-septimal etc., can have applications in lossless signal transmission for long distances and all-optical switching.

- The localised solutions and dynamics of optical systems with refractive index modulation and gain/loss variation via PT-symmetric potentials like Rosen-Morse, multi-well Scarf II, sextic anharmonic double-well, Dirac-δ-Scarf II in the defocusing nonlinear regimes can serve as building blocks for designing

innovatory photonic devices of active control over many undesirable effects.

- The solutions in the symmetry broken phase are also fruitful because of the applications in unidirectional invisibility, one way light transport and so on.
- The work in 1-D system can be extended to 2-D and 3-D systems which may bring out families of nonlinear modes with fascinating and more realistic features like light bullets.
- Researches in nonlinear PT-symmetric optical systems are expanding rapidly because of the easiness of physical realisation and the findings may penetrate into fields like Bose-Einstein condensates, plasmonics, acoustics and electronics.

Appendix

To study the propagation dynamics, the coupled nonlinear partial differential equations

$$i\psi_z + \tfrac{d}{2}\psi_{xx} + \beta|\psi|^2\psi + (V_r + iV_i)\psi + C\phi = 0$$

$$i\phi_z + \tfrac{d}{2}\phi_{xx} + \beta|\phi|^2\phi + (V_r - iV_i)\phi + C\psi = 0,$$

are solved by finite difference beam propagation method using Crank-Nicolson scheme. The first and second derivatives in z and x are replaced by

$$\frac{\partial\psi}{\partial z} = \frac{\psi_i^{s+1} - \psi_i^s}{\Delta z}$$

$$\frac{\partial^2\psi}{\partial x^2} = \frac{\psi_{i-1}^s - 2\psi_i^s + \psi_{i+1}^s}{(\Delta x)^2}.$$

The matlab code used to study the propagation dynamics is given below.

```
clear all; close all; clf; clc;
    A1i_1=(d/(delx).^2)*ONES; C1=diag(C);
N=10;
for z=0:0.1:N;
si_n1=si; AB_si=abs(si);
phi_n1=phi; AB_phi=abs(phi);
Si_z=[Si_z,si]; Phi_z=[Phi_z,phi]; Pow_T=si'*si+phi'*phi;
Pow_si_2=[Pow_si_2,(si'*si)/Pow_T];
Pow_phi_2=[Pow_phi_2,(phi'*phi)/Pow_T];
Ai_s2=(1i./delz)*ONES1-(d./(delx).^2)*ONES1+0.5*beta*AB_si.^2+0.5*(V_r'+1i*V_i');
Bi_s1=(1i./delz)*ONES1+(d./(delx).^2)*ONES1-0.5*beta*AB_si.^2-0.5*(V_r'+1i*V_i');
```

```
A1=diag(Ai_s2)+diag(A1i_1,-1)+diag(A1i_1,1);
B1=diag(Bi_s1)+diag(-A1i_1,-1)+diag(-A1i_1,1);
B_si_n1=B1*si_n1-C1*phi_n1;
si_n2=(inv(A1))*B_si_n1;
Ei_s2=(1i./delz)*ONES1-(d./(delx).^2)*ONES1+0.5*beta*AB_phi.^2+0.5*(V_r'-1i*V_i');
Fi_s1=(1i./delz)*ONES1+(d./(delx).^2)*ONES1-0.5*beta*AB_phi.^2-0.5*(V_r'-1i*V_i');
E1=diag(Ei_s2)+diag(A1i_1,-1)+diag(A1i_1,1);
F1=diag(Fi_s1)+diag(-A1i_1,-1)+diag(-A1i_1,1);
F_phi_n1=F1*phi_n1-C1*si_n1;
phi_n2=(inv(E1))*F_phi_n1;
si=si_n2; phi=phi_n2;
end
figure(1)
z=0:0.1:N;
plot(z,Pow_si_2,z,Pow_phi_2,'linewidth',3);
xlabel('z'); ylabel('Power')
```

Bibliography

[1] L. F. Mollenauer and J. P. Gordon, *The Nonlinear Schrödinger Equation and Ordinary Solitons*, in *Solitons in Optical Fibers*, (Elsevier, 2006), pp. 1–22.

[2] R. W. Boyd, The nonlinear optical susceptibility, in *Nonlinear Optics*, (Elsevier, 2003), pp. 1–65.

[3] A. Hasegawa, *Optical Soliton Theory and Its Applications in Communication*, in *Lecture Notes in Physics*, (Springer Berlin Heidelberg, 2002), pp. 9–31.

[4] A. Hasegawa and F. Tappert, *Applied Physics Letters* **23**, 142 (aug 1973).

[5] A. Hasegawa and F. Tappert, *Applied Physics Letters* **23**, 171 (aug 1973).

[6] G. P. Agrawal, *Nonlinear fiber optics Nonlinear Science at the Dawn of the 21st Century* (Springer, 2000).

[7] C. M. Bender and S. Boettcher, *Physical Review Letters* **80**, 5243 (jun 1998).

[8] N. Moiseyev, *Non-Hermitian quantum mechanics* (Cambridge University Press, 2011).

[9] V. Perinova, A. Luks and J. Krepelka, *J Opt Soc Am B* **36**, p. 855 (2019).

[10] Z. H. Musslimani, K. G. Makris, R. El-Ganainy and D. N. Christodoulides, *Phys. Rev. Lett.* **100**, p. 030402 (2008).

[11] V. V. Konotop, J. Yang and D. A. Zezyulin, *Reviews of Modern Physics* **88**, p. 035002 (2016).

[12] A. Lupu, H. Benisty and A. Degiron, *Opt. Express* **21**, p. 21651 (2013).

[13] R. El-Ganainy, K. G. Makris, M. Khajavikhan, Z. H. Musslimani, S. Rotter and D. N. Christodoulides, *Nat. Phys.* **14**, 11 (2018).

[14] S. K. Gupta, Y. Zou, X.-Y. Zhu, M.-H. Lu, L.-J. Zhang, X.-P. Liu and Y.-F. Chen, *Adv. Mater.* , p. 1903639 (2019).

[15] S. Nixon, L. Ge and J. Yang, *Physical Review A* **85**, p. 023822 (feb 2012).

[16] D. A. Zezyulin and V. V. Konotop, *Physical Review A* **85**, p. 043840 (apr 2012).

[17] K. G. Makris, R. El-Ganainy, D. N. Christodoulides and Z. H. Musslimani, *Physical Review Letters* **100**, p. 103904 (mar 2008).

[18] K. A. Muhsina and P. A. Subha, *Optik* **127**, 7550 (2016).

[19] C. P. Jisha, L. Devassy, A. Alberucci and V. C. Kuriakose, *Physical Review A* **90**, p. 043855 (oct 2014).

[20] T. P. Suneera and P. A. Subha, *Waves Random Complex Media* **27**, 241 (2016).

[21] T. P. Suneera and P. A. Subha, *Chaos Solit. Fractals* **98**, 183 (2017).

[22] R. El-Ganainy, K. G. Makris, D. N. Christodoulides and Z. H. Musslimani, *Optics Letters* **32**, p. 2632 (aug 2007).

[23] K. A. Muhsina and P. A. Subha, *J. Mod. Opt.* **63**, 1584 (2016).

[24] K. A. Muhsina and P. A. Subha, *Eur. Phys. J. D* **69** (2015).

[25] Y. Chen and Z. Yan, *Scientific Reports* **6** (mar 2016).

[26] Y. Chen and Z. Yan, *Physical Review E* **95**, p. 012205 (jan 2017).

[27] Y. Kivshar, *Physics Reports* **298**, 81 (may 1998).

[28] V. Achilleos, P. G. Kevrekidis, D. J. Frantzeskakis and R. Carretero-González, *Physical Review A* **86**, p. 013808 (jul 2012).

[29] Y. V. Bludov, V. V. Konotop and B. A. Malomed, *Physical Review A* **87**, p. 013816 (jan 2013).

[30] N. M. Musammil, P. A. Subha and K. Nithyanandan, *Optik* **159**, 176 (2018).

[31] N. M. Musammil, K. Porsezian, P. A. Subha and K. Nithyanandan, *Chaos* **27**, p. 023113 (2017).

[32] N. M. Musammil, P. A. Subha and K. Nithyanandan, *Phys. Rev. E* **100**, p. 012213 (2019).

[33] W. Yu, M. Ekici, M. Mirzazadeh, Q. Zhou and W. Liu, *Optik* **165**, 341 (jul 2018).

[34] A.-M. Wazwaz, *Optik* **192**, p. 162948 (sep 2019).

[35] N. P. Proukakis, N. G. Parker, D. J. Frantzeskakis and C. S. Adams, *Journal of Optics B: Quantum and Semiclassical Optics* **6**, S380 (may 2004).

[36] V. Serkin, *Optik* **173**, 1 (nov 2018).

[37] Z. Ahmed, *Physics Letters A* **282**, 343 (apr 2001).

[38] Z. Ahmed, S. Kumar and D. Ghosh, *Physical Review A* **98**, p. 042101 (oct 2018).

[39] J. Sudharsan, V. Chandrasekar, K. Manikandan, D. Aravinthan and G. Saadhana, *Optik* **268**, p. 169796 (oct 2022).

[40] K. Manikandan and J. B. Sudharsan, *Optik* **256**, p. 168703 (2022).

[41] K. Hari, K. Manikandan and R. Sankaranarayanan, *Physics Letters A* **384**, p. 126104 (feb 2020).

[42] J. Meiyazhagan, K. Manikandan, J. B. Sudharsan and M. Senthilvelan, *Chaos: An Interdisciplinary Journal of Nonlinear Science* **32** (may 2022).

[43] I. V. Barashenkov, D. A. Zezyulin and V. V. Konotop, *New Journal of Physics* **18**, p. 075015 (jul 2016).

[44] D. A. Zezyulin, I. V. Barashenkov and V. V. Konotop, *Physical Review A* **94**, p. 063649 (dec 2016).

[45] C.-Q. Dai, Y. Fan and Y.-Y. Wang, *Nonlinear Dynamics* **98**, 489 (aug 2019).

[46] G. Yao, Y. Li and R.-P. Chen, *Photonics* **9**, p. 249 (April 2022).

[47] J. Li, Y. Zhang and J. Zeng, *iScience* **25**, p. 104026 (apr 2022).

[48] C.-Q. Dai and Y.-Y. Wang, *Nonlinear Dyn.* **80**, 715 (2015).

[49] A. Sahoo, D. K. Mahato, A. Govindarajan and A. K. Sarma, *Phys. Rev. A* **106**, p. 043502 (2022).

[50] C. P. Jisha, A. Alberucci, V. A. Brazhnyi and G. Assanto, *Phys. Rev. A* **89**, p. 013812 (2014).

[51] J.-G. Liu, M. Osman and A.-M. Wazwaz, *Optik* **180**, 917 (feb 2019).

[52] L. Akinyemi, H. Rezazadeh, S.-W. Yao, M. A. Akbar, M. M. Khater, A. Jhangeer, M. Inc and H. Ahmad, *Results in Physics* **26**, p. 104411 (jul 2021).

[53] S. Das, K. K. Dey and G. A. Sekh, *Optik* **247**, p. 167865 (dec 2021).

[54] O. González-Gaxiola, A. Biswas, F. Mallawi and M. R. Belic, *Journal of Advanced Research* **21**, 161 (jan 2020).

[55] C. Q. Dai, Y. Y. Wang, Y. Fan and D. G. Yu, *Nonlinear Dyn.* **92**, 1351 (2018).

[56] Y.-X. Chen, X. Xiao and F.-Q. Xu, *Physica Scripta* **94**, p. 095201 (jun 2019).

[57] H.-P. Zhu and Z.-H. Pan, *Nonlinear Dynamics* **89**, 1745 (may 2017).

[58] R.-R. Wang, Y.-Y. Wang and C.-Q. Dai, *Optik* **254**, p. 168639 (mar 2022).

[59] K. Manikandan, D. Aravinthan, J. Sudharsan and S. Reddy, *Optik* **266**, p. 169594 (sep 2022).

[60] W.-B. Bo, W. Liu and Y.-Y. Wang, *Optik* **255**, p. 168697 (apr 2022).

[61] X. Zhu, W. Che, Z. Wu, J. Xie and Y. He, *Journal of Optics* **22**, p. 035503 (feb 2020).

[62] X. Zhu, F. Yang, S. Cao, J. Xie and Y. He, *Optics Express* **28**, p. 1631 (jan 2020).

[63] W. Che, F. Yang, S. Cao, Z. Wu, X. Zhu and Y. He, *Physics Letters A* **413**, p. 127606 (oct 2021).

[64] G. Lévai, F. Cannata and A. Ventura, *Physics Letters A* **300**, 271 (jul 2002).

[65] M. Nazari, F. Nazari and M. K. Moravvej-Farshi, *Journal of the Optical Society of America B* **29**, p. 3057 (oct 2012).

[66] Z. Yan, Z. Wen and C. Hang, *Phys. Rev. E* **92**, p. 022913 (2015).

[67] Y. Chen, Z. Yan and D. Mihalache, *Physical Review E* **102**, p. 012216 (jul 2020).

[68] Y. Chen, Z. Yan and B. A. Malomed, *Phys. D: Nonlinear Phenom.* **430**, p. 133099 (2022).

[69] X. Zhu, X. Peng, Y. Qiu, H. Wang and Y. He, *New Journal of Physics* **22**, p. 033035 (mar 2020).

[70] X. Zhu, Z. Cai, J. Liu, S. Liao and Y. He, *Nonlinear Dynamics* **108**, 2563 (mar 2022).

[71] S. Yang, Q.-Y. Zhang, Z.-W. Zhu, Y.-Y. Qi, P. Yin, Y.-Q. Ge, L. Li, L. Jin, L. Zhang and H. Zhang, *Optics & Laser Technology* **152**, p. 108116 (aug 2022).

[72] Y. Zhang, C. Yang, W. Yu, M. Liu, G. Ma and W. Liu, *Optical and Quantum Electronics* **50** (jul 2018).

[73] A. R. Seadawy and N. Cheemaa, *Physica Scripta* **95**, p. 065209 (apr 2020).

[74] Z. Yang, W.-P. Zhong, M. Belić and W. Zhong, *Optik* **222**, p. 165417 (nov 2020).

[75] L. Zeng, V. V. Konotop, X. Lu, Y. Cai, Q. Zhu and J. Li, *Optics Letters* **46**, p. 2216 (apr 2021).

[76] X. Hu, J. Guo, G. D. Shao, Y. F. Song, L. M. Zhao, L. Li and D. Y. Tang, *Physical Review A* **101**, p. 063807 (jun 2020).

[77] B. Ren, H. Wang, V. O. Kompanets, Y. V. Kartashov, Y. Li and Y. Zhang, *Nanophotonics* **10**, 3559 (aug 2021).

[78] L. Zeng, J. Shi, J. Li, J. Li and Q. Wang, *Optics Express* **30**, p. 42504 (nov 2022).

[79] J. Li, Y. Zhang and J. Zeng, *Chaos, Solitons & Fractals* **157**, p. 111950 (apr 2022).

[80] L. Zeng and J. Zeng, *Advanced Photonics* **1**, p. 1 (aug 2019).

[81] J. Li and J. Zeng, *Physical Review A* **103**, p. 013320 (jan 2021).

[82] L. Zeng, B. A. Malomed, D. Mihalache, Y. Cai, X. Lu, Q. Zhu and J. Li (may 2021).

[83] A. R. Thasneem, P. A. Subha and K. A. Muhsina, *Optik* **265**, p. 169518 (2022).

[84] B. A. Kalinikos and A. B. Ustinov, *Nonlinear Spin Waves in Magnetic Films and Structures*, in *Solid State Physics*, (Elsevier, 2013), pp. 193–235.

[85] Y. S. Kivshar and S. K. Turitsyn, *Optics Letters* **18**, p. 337 (March 1993).

[86] S. V. Suchkov, A. A. Sukhorukov, J. Huang, S. V. Dmitriev, C. Lee and Y. S. Kivshar, *Laser Photonics Rev.* **10**, 177 (2016).

[87] A. A. Sukhorukov, Z. Xu and Y. S. Kivshar, *Phys. Rev. A* **82**, p. 043818 (2010).

[88] S. Karthiga, V. K. Chandrasekar, M. Senthilvelan and M. Lakshmanan, PT-symmetric nonlinear systems and their implication in optics, in *Indian Academy of Sciences Conference Series (2019) 2:1 Indian Academy of Sciences DOI: 10.29195/iascs.02.01.0011*, 2019.

[89] H. Ramezani, T. Kottos, R. El-Ganainy and D. N. Christodoulides, *Physical Review A* **82**, p. 043803 (October 2010).

[90] N. M. Musammil, K. Porsezian, K. Nithyanandan, P. A. Subha and P. T. Dinda, *Opt. Fiber Technol.* **37**, 11 (2017).

[91] T. P. Suneera and P. A. Subha, *J. Opt.* **20**, p. 095504 (2018).

[92] T. P. Suneera and P. A. Subha, *J. Mod. Opt.* **66**, 1528 (2019).

[93] F. K. Abdullaev and A. A. Abdumalikov, *Optik* **219**, p. 165158 (2020).

[94] O. B. Kirikchi and N. Karjanto, *Nonlinear Dyn.* **103**, 2769 (2021).

[95] T. P. Suneera and P. A. Subha, *Eur. Phys. J. Plus* **133**, 1 (2018).

[96] G. Burlak, Z. Chen and B. A. Malomed, *Communications in Nonlinear Science and Numerical Simulation* **109**, p. 106282 (jun 2022).

[97] Z. C. Wen and Z. Yan, *Physics Letters A* **379**, 2025 (sep 2015).

[98] A. R. Thasneem and P. A. Subha, *Physica Scripta* **98**, p. 035208 (2023).

[99] Z. Wu, S. Cao, W. Che, F. Yang, X. Zhu and Y. He, *Results in Physics* **19**, p. 103381 (dec 2020).

[100] C. Huang, H. Deng, W. Zhang, F. Ye and L. Dong, *EPL (Europhysics Letters)* **122**, p. 24002 (jun 2018).

[101] K. Manikandan, D. Aravinthan, J. Sudharsan and R. Vadivel, *Optik* **271**, p. 170105 (2022).

[102] Z. Zhou, J. Song, W. Weng and Z. Yan, *Applied Mathematics Letters* **132**, p. 108131 (oct 2022).

[103] G. Burlak, S. Garcia-Paredes and B. A. Malomed, *Chaos: An Interdisciplinary Journal of Nonlinear Science* **26** (nov 2016).

[104] A. R. Thasneem and P. A. Subha, *Chaos, Solitons & Fractals* **177**, p. 114245 (December 2023).

[105] L. Devassy, C. P. Jisha, A. Alberucci and V. C. Kuriakose, *Phys. Rev. E* **92**, p. 022914 (2015).

[106] K. Gillen-Christandl, G. D. Gillen, M. J. Piotrowicz and M. Saffman, *Applied Physics B* **122** (apr 2016).